Studies of the Outer Solar System Using the Dark Energy Survey

by

Stephanie J. Hamilton

A dissertation submitted in partial fulfillment
of the requirements for the degree of
Doctor of Philosophy
(Physics)
in The University of Michigan
2019

Doctoral Committee:

Professor David Gerdes, Chair
Professor Fred Adams
Assistant Professor Emily Rauscher
Professor Keith Riles

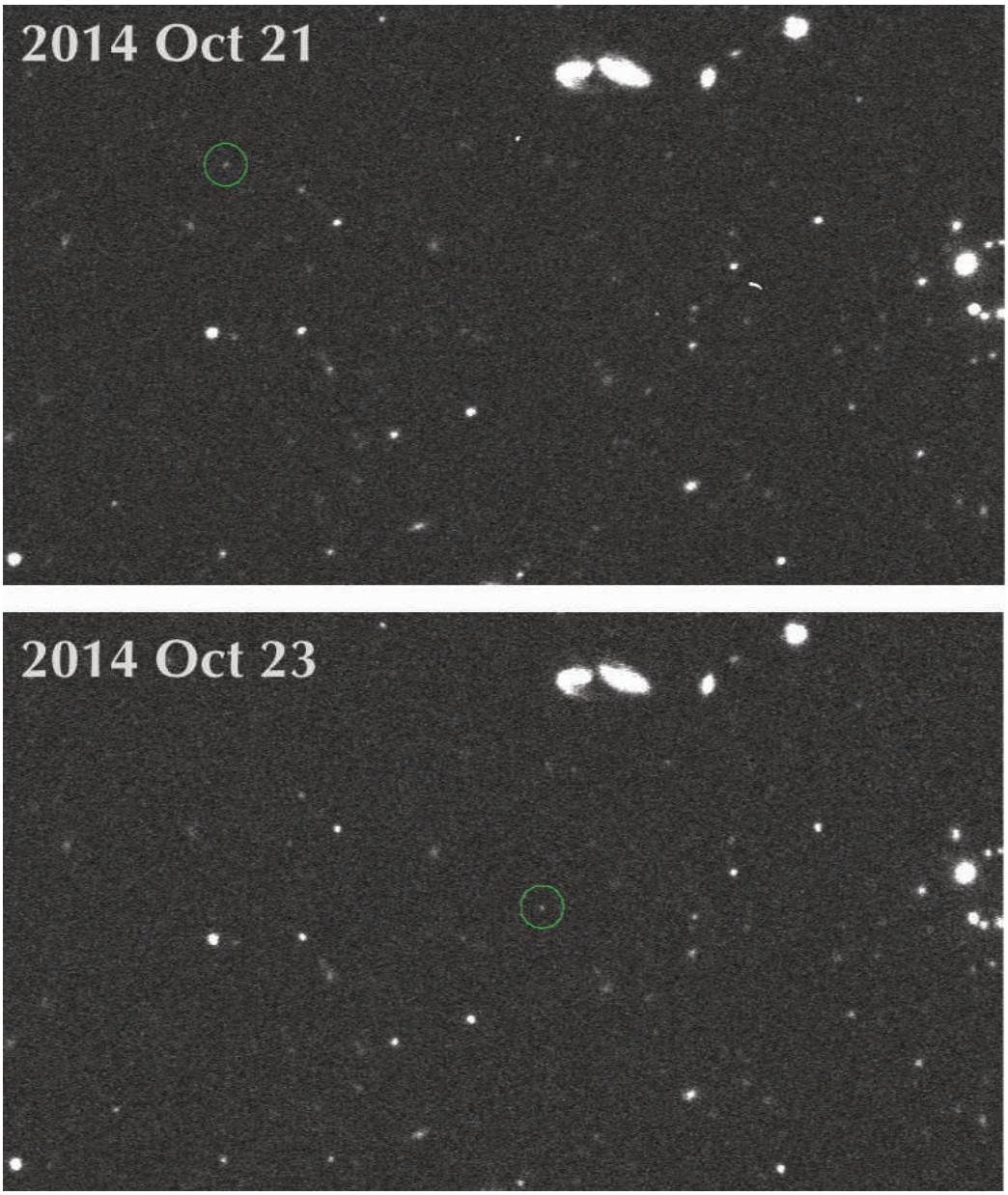

Discovery of a new trans-Neptunian object in the wild – "DeeDee," our beloved distant dwarf planet.

Stephanie J. Hamilton
sjhamil@umich.edu
ORCID iD: 0000-0002-6126-8487

For my parents,

who have always encouraged me to reach for the stars.

☆ ☆ ☆

ACKNOWLEDGEMENTS

I cannot possibly thank all of the people who have gotten me to this point and enabled this thesis in just a few short pages. What follows is an incomplete attempt to do so anyway.

First and foremost, thank you to David Gerdes, my thesis advisor and committee chair, who provided guidance on everything from project direction to code bugs to the finer aspects of craft beer. Your advice and encouragement has been invaluable throughout this graduate school journey. A further thank you to Fred Adams for enlightening and nuanced discussions and for your wisdom on things both physics and not. And thank you to the rest of my committee for your time and expertise. You all have made me a better scientist.

Many thanks to the rest of the Michigan TNO group (Ed, Juliette, Larissa, Tali, Kevin, Kyle, and Lynus) and to the incredible REU students who have come through our group in the past few years (Colin and Kyle) for enlightening discussions, and for reminding me why I chose this research on the days my code wouldn't work. A further thank you to our colleagues at the University of Pennsylvania and Fermilab for joining this effort and expanding it beyond what Dave or I, or the entire Michigan group, could have done on our own.

Thank you to the Dark Energy Survey Collaboration for being my scientific family and for allowing me to study the tiny moving points of reflected light from Solar System objects in this unique dataset. Many thanks especially to Tom Diehl, the DES Operations team, and all the staff at CTIO for providing (three) experiences of a

lifetime to stare at the beautiful Chilean Southern hemisphere sky — I mean, operate the telescope to take data for DES. It was an honor to work with the Education and Public Outreach team and to serve as the chair of the Early Career Scientists Committee. Many of my most memorable experiences have been a result of my involvement with this wonderful group of people. Additional thanks to the NSF, NASA, and the AAS for funding my research and travels over the past five years.

I would not have found myself on this career track if it were not for my high school physics teacher, Mr. Burdick. Thank you for inspiring me, encouraging me, and making physics oh, so much fun. I truly would not be where I am without you. I also thank my undergraduate mentors, Joey Huston and Wade Fisher, for showing me the ropes of research and setting me up for success in whatever form that took. I've had some incredible experiences as a result of your guidance and mentorship, from witnessing the Higgs boson announcement at CERN to everything I've gotten to do in graduate school.

I would like to thank the RELATE science communication organization at Michigan (Deanna, Joe, Nick, Patsy, Alison, Isabel, Fatima, and especially Elyse and Brandon) for providing me with my first formal scicomm training and with great friends with whom I can geek out about the best ways to tell a research story. My passion for scicomm has only grown exponentially, and so much of my success has been a direct result of RELATE. Thank you also to Nathan, Susanna, and the entire ComSciCon team for providing me with some of the most rewarding experiences I've had, including helping organize a scicomm conference. And thanks to the Society for Women in Physics not only for providing opportunities to teach aspiring young scientists about cool physics demonstrations but also for creating a strong sense of community and fighting for an ever-more inclusive department climate.

Thank you to all the friends and officemates I've had the pleasure of interacting with over these past few years: Chelsea, Morgan, Rutu, Anthony, Jessie, Noah, Mid-

hat, Natasha, and so many others. Thank you to Katie for reminding me that there is still a world outside of physics and graduate school, because it is so easy to get lost in the stress and the details. Thank you to the rest of my Spartan Marching Band family (Sarah K, Sarah C, KC, Tyler D, Tyler V, Nick, and many, many others) for continuing to be my home-away-from-home and for reminding me of the healing power of good friends and good music.

Thank you to my parents, my brothers, and the rest of my family for supporting me through this hectic and stressful time of my life. To my dad, who is sometimes more enthusiastic about my interests than I am. Thank you for that pair of binoculars, for fixing Uncle Bobby's old telescope so I could use it, and for always driving me to watch the International Space Station fly overhead. And to my mom for being a kick-butt woman in STEM role model, for sending me that first REU opportunity at Fermilab that kicked off my whole career, and for everything you've done to support and encourage me throughout my life. I can only hope to be as great a role model for my future daughters as you've been for me. Finally, thank you Nils for staying unwaveringly by my side even though three states separated us (or an entire country, depending on the route). You believed in me when I doubted myself, challenged me to be the best version of myself, and supported me throughout my many graduate school endeavors. I look forward to whatever the universe has in store for us next.

TABLE OF CONTENTS

LIST OF FIGURES

Figure

LIST OF TABLES

Table

LIST OF APPENDICES

Appendix

ABSTRACT

The minor bodies of the Solar System encode information about the formation and dynamical evolution of the Solar System. The bodies beyond Neptune, trans-Neptunian objects (TNOs), serve as dynamical tracers of gravitational interactions between these bodies and the giant planets. By studying their orbits and surface properties, as both individual objects and as populations, we paint a more complete picture of the formation and evolution history of the Solar System. This thesis uses data from the Dark Energy Survey, a wide-area and relatively deep cosmological survey, to study both individual minor bodies discovered by the survey and populations implied by detected objects.

The largest TNOs provide a window into the formation environment in the distant Solar System because they have sufficient gravity to retain at least some of their original volatiles and ices. While most TNOs are too distant, and therefore too faint, to obtain reflectance spectra that would enable detailed study of their surface compositions, a measurement of their albedo can still provide insight. We use measurements from DES and ALMA to calculate the diameter and albedo of the first dwarf planet candidate detected using DES at $D = 635^{+57}_{-61}(\mathrm{stat})^{+32}_{-39}(\mathrm{sys})$ km and $p_V = 13.1^{+3.3}_{-2.4}(\mathrm{stat})^{+2.0}_{-1.4}(\mathrm{sys})$, implying a rocky-ice composition.

All surveys suffer from inherent biases due simply to the design of the survey. The "survey simulator" approach to debiasing survey detections has gained traction in recent years. I describe the design of the DES survey simulator and use it to characterize the discoveries of interesting TNOs by DES. I describe the simulator's use in a population study of Neptune Trojans, culminating in a population estimate

of 162 ± 73 L4 Neptune Trojans with $H_r < 10$ (consistent with previous estimates). Finally, I use the simulator to debias the orbital clustering of the most distant TNOs discovered by DES. Objects in this class have been used to argue for the existence of a distant massive planet in the Solar System. I find that DES is unable to distinguish between additional planet scenario and the scenario in which the observed objects originate from a uniform underlying distribution.

CHAPTER I

Introduction

1.1 The Trans-Neptunian Region

The Kuiper Belt region of the Solar System consists of small planetesimals and other minor bodies that orbit the Sun with a semimajor axis beyond that of Neptune (30 au). It is impossible to directly observe the conditions in the early Solar System that led to the formation of these objects nor the dynamical processes that led to their current orbits. However, these objects constitute a preserved relic of conditions in the early Solar System and serve as dynamical tracers of the formation and evolution history of the Solar System. By studying them, we can learn how the Solar System formed and evolved, and by extension, how other solar systems evolve, potentially toward conditions for life.

The history of the trans-Neptunian region begins with observations of Uranus and Neptune's orbits that suggested additional unseen mass beyond the orbits of both planets. While we now know the orbital discrepancies were erroneous (Davies et al., 2008), Clyde Tombaugh discovered a new object beyond Neptune in 1930 using telescope at Lowell Observatory. The new object was originally purported to be larger than Jupiter, but it was quickly realized this could not be true once further observations showed it to be an unresolved point source. Of course, this new object is now known as Pluto, and its discovery spurred the realization that there must be

more mass still hiding beyond the orbit of Neptune.

Edgeworth first attempted to quantify the mass of the trans-Neptunian region in 1949 (Edgeworth, 1943), which led to the hypothesis that a large reservoir of planetesimals remained undiscovered beyond Neptune. Two years later, Kuiper postulated the existence of a disk of objects between 38–50 au (Kuiper, 1951). Yet it would take another 40 years for telescope and camera technology to enable the first observations of this hypothesized planetesimal disk.

In 1992, the second trans-Neptunian object (TNO) was discovered – 1992 QB_1 (Jewitt & Luu, 1993). With this discovery, earnest searches for additional bodies beyond Neptune commenced and continue to this day. To date, more than 2000 TNOs have been discovered, accumulated from searches spanning only three decades (see Figure 1.1). These searches have been motivated by the recognition that studying the characteristics and orbits of objects in a remnant debris disk such as the Kuiper Belt would provide insight into the Solar System's formation and dynamical processes that have resulted in what we observe today.

1.1.1 The Dynamical History of the Solar System

One accepted model of Solar System formation is the Nice II model, developed by Levison et al. (2011). This model is a modification of the original Nice model (Tsiganis et al., 2005; Gomes et al., 2005; Morbidelli et al., 2005), in which the giant planets formed much closer to the Sun than their present positions, immersed in a disk of small planetesimal objects with a total mass of tens of Earth masses. Angular momentum transfer from scattering interactions between the planetesimals and the giant planets caused the three outer planets to migrate outward, while Jupiter migrated inward. A violent, global instability was triggered when Jupiter and Saturn crossed their mutual 2:1 mean motion resonance (MMR). Uranus and Neptune were thrown into chaotic, eccentric orbits, resulting in the ejection of 99% of the planetesimal disk and

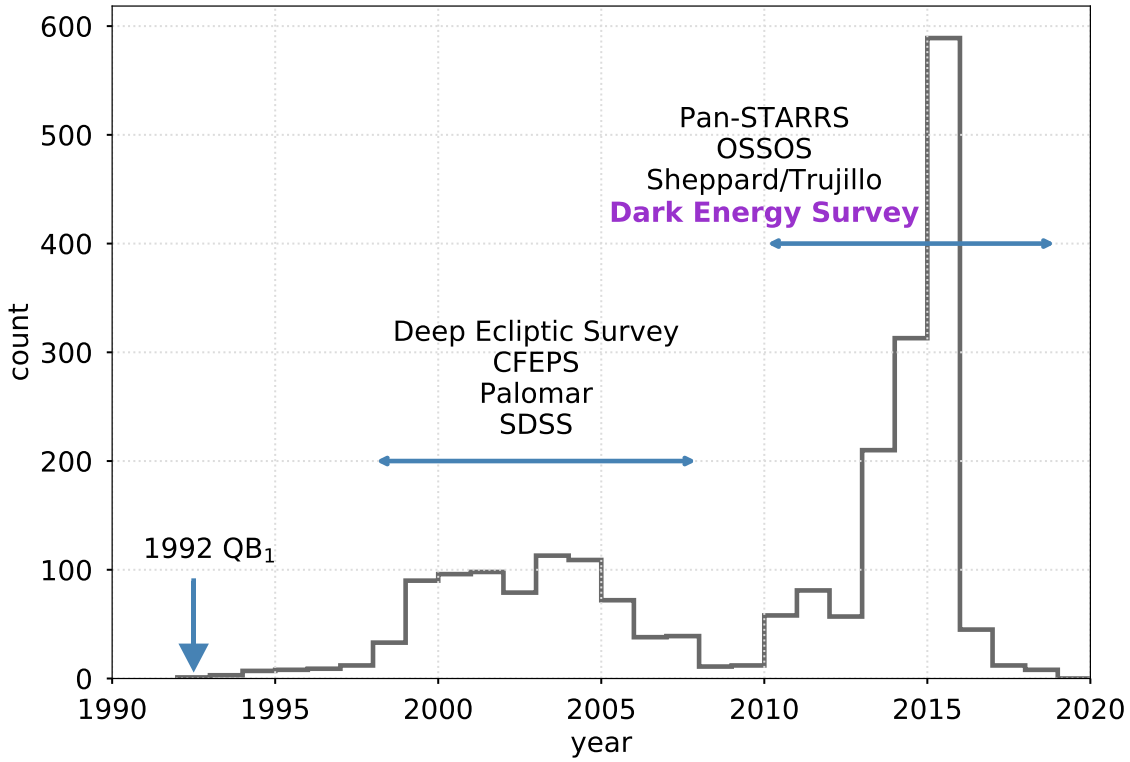

Figure 1.1: A differential histogram of the number of TNOs discovered per year, using data from the Minor Planet Center as of 2019-04-14. The year spans are meant to designate periods of time in which there were multiple TNO surveys active, rather than to designate the exact start and end dates of the listed surveys.

represents a possible cause of the Late Heavy Bombardment noted in the Inner Solar System. The orbits of Uranus and Neptune gradually stabilized via dynamical friction with the remaining planetesimals as they settled into their current configuration.

Development of the Nice II model arose from attempts to overcome some troubling limitations of the Nice model, including the seemingly arbitrary choice of the initial positions of the giant planets, the extremely sensitive response of the instability trigger time to the location of the planetesimal disk edge, and the neglect of gravitational interactions between disk particles. The resulting model begins with the giant planets in a quadruple MMR (i.e., each planet is in an MMR with its neighbor or neighbors) as in Morbidelli et al. (2007). As a result of the resonant capture of the ice giants, the inner ice giant (Ice I) has a larger eccentricity than the other planets. Viscous stirring resulting from interactions between planetesimals leads to a transfer of energy between the disk and the planets that does not require close interactions. Simulations revealed a coupling between the eccentricity of the planetesimals and the planets' semi-major axes. The coupling depended on the planets' eccentricities and thus would maximally affect the planet with the most eccentric orbit. Energy transfer with the disk causes the eccentricities of the planetesimals to increase and the planets to migrate inward, with the eccentric Ice I having the fastest migration rate. The eccentricity of Ice I increases as it drags the other planets with it, maintaining the quadruple MMR. Secular resonance crossings then cause Ice I's eccentricity to fluctuate, sometimes enough to break the quadruple MMR and throw the Solar System into chaos.

Despite being remarkably successful, there are still unanswered questions within the Nice II model. For example, it significantly under-predicts the number of highly inclined TNOs observed (Levison et al., 2008). The Nice II model also fails to describe the orbits of TNOs with perihelia too large to have had a past interaction with Neptune and provides no explanation for the observed clustering in the arguments of perihelia and the longitudes of ascending node of the most distant objects.

Further iterations of these models have striven to more accurately reproduce observed features in the minor body populations. In one such example, Nesvorný (2015) proposed a sudden "jumpy" MMR crossing between Jupiter and Saturn caused by interactions with an ice giant planet to explain the relative lack of excited Main Belt Asteroids that otherwise arise from simulations of a smooth MMR crossing. In this latter case, secular resonances of both Saturn and Jupiter would sweep up Main Belt Asteroids as the giant planets' migration progresses, while a sudden MMR crossing prevents such excitation. Another iteration upon the Nice models includes a fifth giant planet that is eventually ejected from the Solar System completely after repeated encounters with Saturn and Jupiter that cause their orbits to evolve in a piecewise fashion (Nesvorný & Morbidelli, 2012).

Regardless of the specifics of these dynamical instability models and their iterations, each comes to the conclusion that the minor body populations of the Solar System – the Kuiper Belt, Main Asteroid Belt, objects with giant-planet-crossing orbits called Centaurs, etc. – all originated from the same primordial disk and so are expected to share similar properties. In essence, differences between these various populations inform us as to where in the primordial disk they formed and what processes they have undergone, whether collisional, radiative, or otherwise.

1.1.2 Probing Models of Solar System Evolution Using TNOs

The past 30 years of exploration of the Kuiper Belt have answered many questions about the Solar System's formation and evolution, but they have also raised many new questions. In particular, the current inventory of KBOs does not allow us to distinguish between various models of Neptune's migration (Tsiganis et al., 2005; Levison et al., 2008; Brasser & Morbidelli, 2013; Nesvorný & Vokrouhlický, 2016; Lawler et al., 2018b). However, the orbital distributions of the remaining planetesimals that today comprise the Kuiper Belt provide strong constraints on the nature

of Neptune's migration through this region. For example, the objects discovered in MMRs with Neptune can inform models of Neptune's migration, e.g. a "jumpy" migration vs. a smooth migration (Nesvorný, 2015; Nesvorný et al., 2016; Kaib & Sheppard, 2016), where numerical simulations suggest differing relative fractions of objects in the various MMRs depending on the model of Neptune migration used. Furthermore, Hahn & Malhotra (2005) note that many objects originally classified as scattering off of Neptune are in fact in high-order resonances, perhaps indicating that Neptune migrated through an already-excited Kuiper Belt.

Studying the dynamical properties of populations of KBOs alongside their chemical or physical properties enables deduction of the dynamical past of these populations. Spectroscopic observations of TNOs are generally not possible due to their large distances from Earth and correspondingly faint apparent magnitudes. However, measuring their colors using broad bandpass filters provides a proxy to their chemical compositions. The chemical compositions of minor bodies may then provide clues as to where they formed within the protoplanetary disk and what processes they have been subject to. One model attempting to explain the observed differences in the surfaces of small, < 500-km-sized TNOs posits that minor bodies formed in several distinct classes, defined by ice lines of different volatiles and resulting in unique surface properties for each class (Dalle Ore et al., 2013). A second model (Fraser & Brown, 2012) describes compositional class as correlating with dynamical class – objects formed with relatively homogeneous composition between $15 - 45$ au, but rapidly lost specific volatiles depending on surface temperature and therefore the object's location. Dynamical mixing of objects and long-term chemical evolution have since given rise to the variety of surface colors observed today. Wong et al. (2014) have also proposed a collisional element to the dynamical evolution through studies of Jupiter Trojans, which would expose new material to solar irradiation and explain a relative dearth in neutrally colored small Jupiter Trojans.

Neptune Trojans, despite being thought to originate from dynamically excited TNOs, have been observed to be much more neutral in color (similar to Jupiter Trojans) than their hypothesized progenitor population. Lin et al. (2019) report the discovery of the first ultra-red and the two highest-inclination Neptunian Trojans by the Dark Energy Survey. They suggest that Neptune Trojans appear bluer (despite being predicted to originate from the redder Kuiper Belt; Nesvorný & Vokrouhlický 2009) due to collisions with Plutinos. This hypothesis can be tested by studying the colors of both Neptunian Trojans and Plutinos as a function of their inclinations.

As more TNOs have been discovered, they have been classified into various subpopulations based on similar orbital characteristics. This classification serves as way to group objects into populations that may have common and distinct origins, providing clues to how they arrived at their present orbits. Orbits of Solar System bodies are described using six parameters: semimajor axis a, eccentricity e, inclination i, argument of perihelion ω, longitude of ascending node Ω, and mean anomaly M (which is related to the true anomaly ν by $M = E - e \sin E$, where $E = \cos^{-1}(e + (1 - e\cos E)\cos\nu)$ is the eccentric anomaly). The semimajor axis and eccentricity describe the size and shape of the orbit. The inclination describes the tilt of the orbit relative to the mean plane of the Solar System, and the argument of perihelion and longitude of ascending node describe the remaining orientation of the orbit. The mean anomaly is a quantity that advances along the orbital path from the perihelion location uniformly in time and describes the position of the object in its orbit. The longitude of perihelion, $\varpi = \omega + \Omega$, is another commonly used parameter that describes the orientation of the perihelion direction in physical space. Finally, the perihelion distance q is often quoted for trans-Neptunian objects because it is a measure of how closely an object's orbit approaches that of Neptune at $a = 30.1$ au and therefore how strongly the object may be perturbed by Neptune. Figure 1.2 depicts the parameters that define an orbit.

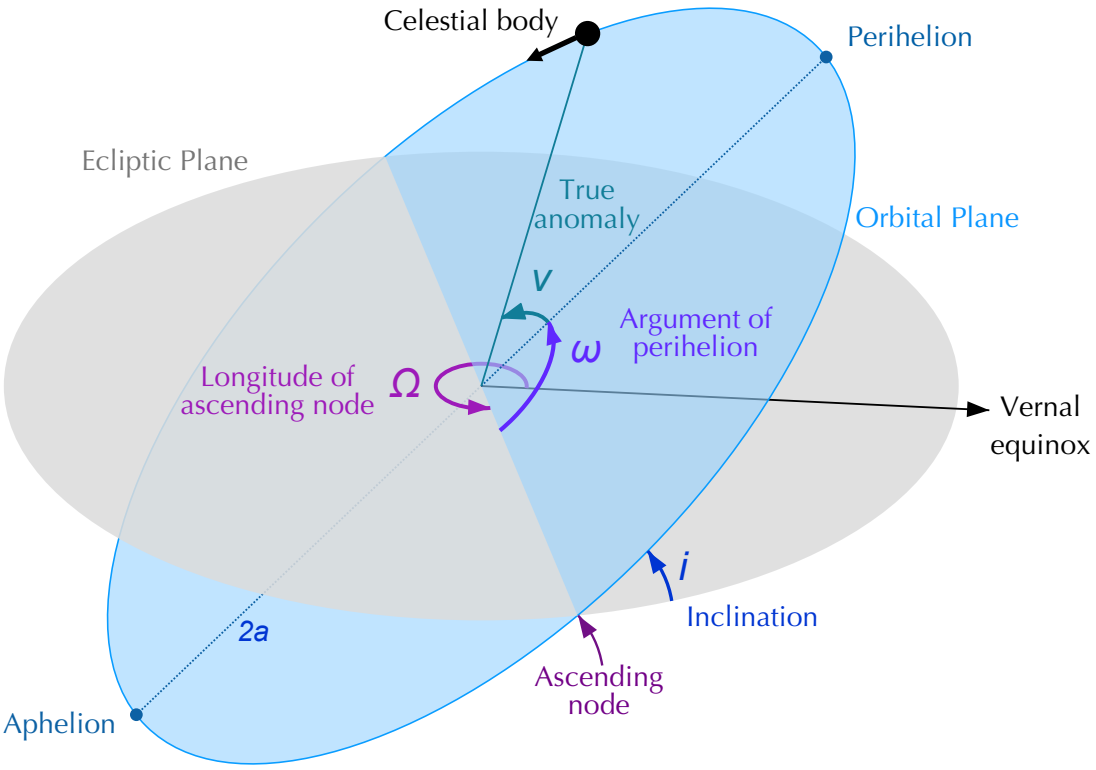

Figure 1.2: Depiction of the Keplerian orbital elements. This image is based off of the image https://commons.wikimedia.org/wiki/File:Orbit1.svg, licensed under a CC BY-SA 3.0 license.

With orbital elements in hand, objects can then be classified into different dynamical populations through the use of N-body integrations for several million years of Solar System time. The behavior of the orbit over time determines its dynamical class. TNOs can generally be divided into one of three populations: resonant objects, whose orbital periods are an integer ratio to that of Neptune; dynamically cold objects, whose orbits generally have low inclination and eccentricity; and dynamically hot objects, whose orbits generally have higher inclination and eccentricity. The cold and hot objects can be further divided into more specific classes that probe different characteristics of Neptune's migration (see Section 2.3.1 for more details).

In this thesis I consider the characteristics of individual objects, in addition to their membership of different TNO populations, in order to probe the formation and evolution history of the Solar System.

1.2 Surveying the Trans-Neptunian Region

Since the discovery of 1992 QB_1, a number of dedicated TNO surveys have turned toward the sky, resulting in the discovery of more than 2000 TNOs to date. The first astronomical survey dedicated to searching for new TNOs was the Deep Ecliptic Survey (DEcS, Millis et al. 2002), which imaged 550 deg^2 near the ecliptic plane from 1998-2003. DEcS discovered nearly 500 TNOs, enough to show that the edge of the Kuiper Belt lies ∼50 au from the Sun, a result that still stands today.

Subsequent TNO surveys include the Palomar Distant Solar System Survey (2007-2008, Schwamb et al. 2010), the Canada-France Ecliptic Plane Survey (CFEPS, 2003-2009; Jones et al. 2006; Petit et al. 2011), Pan-STARRS 1 (2010–, Kaiser et al. 2002), and the Outer Solar System Origins Survey (OSSOS, 2013-2016; Bannister et al. 2016, 2018), among others.[1] The collective efforts of all of these surveys have resulted in

[1]Michelle Bannister has compiled a nice list of TNO surveys through 2014 at https://github.com/mtbannister/tnosurveys.

the discovery of the ∼2200 known TNOs.

This thesis uses data collected by the Dark Energy Survey (DES, Abbott et al. 2006), an optical survey currently imaging a large portion of the Southern sky in five wavelength bands in order to measure the dark energy equation of state. The project was granted 525 nights over five years, beginning September 2013, to complete this measurement. It was granted an additional 52 nights from August 2018 to January 2019 to complete the survey to full depth after operations fell behind schedule. The wide area and magnitude depth required to achieve its original purpose will make DES one of the most powerful TNO surveys to date. DES consists of two interleaved surveys: the 5000 deg^2 Wide survey extending from $i \approx 0°$ to $i \approx 80°$ with an r-band magnitude depth of 23.8; and the Supernova survey, consisting of eight "shallow" 3 deg^2 fields and two "deep" fields imaged on a weekly cadence with single r-band exposure depths of 24.1 and 24.7, respectively.

Most dedicated TNO surveys employ specific observing strategies to maximize discovery capabilities in the region beyond Neptune. In particular, repeated visits to the same field are spaced in time such that the motion of a TNO on the sky is easily recognized as a straight line of points separated by a few factors of the point-spread function of a typical image. For TNOs, which have hourly rates of motion from $\sim 5''$ per hour to less than $1''$ per hour, the observing cadence is typically 30 minutes to over an hour between images. DES instead makes irregular repeated visits to the same field, with consecutive exposures sometimes occurring weeks apart. In order to repurpose the dataset of DES for TNO discovery and characterization, the observing cadence must be taken into account. The next section discusses this and other sources of potential bias in more detail.

1.2.1 Describing Survey Biases

To first order, whether or not a TNO is detected depends on whether it is bright enough to be observed by a particular telescope or survey. TNOs are only visible because they reflect sunlight. This reflected light is already decreased by a factor of $1/r_{\odot}^2$, where $r_{\odot}$ is the distance from the Sun to the object. The object does not reflect all of the sunlight, a property characterized by the albedo p. The flux that reaches Earth is ultimately reduced by an additional factor of $1/r_{\oplus}^2$, where $r_{\oplus}$ is the distance from the object to Earth. Because the distances of TNOs are generally much greater than the variation in distance induced by Earth's motion around the Sun, it is common to approximate $r_{\odot} \approx r_{\oplus}$ such that the observed brightness of a TNO from Earth depends on $1/r_{\odot}^4$.

The brightness of TNOs is often expressed in terms of the absolute magnitude, H, which is defined as the apparent magnitude an object would have if viewed from a phase angle of 0° at a distance of 1 au. This can be written functionally as

$$H = m - 5\log_{10}\left(\frac{r_{\oplus} r_{\odot}}{r_0^2}\right) + 2.5\log_{10} q(\alpha) \tag{1.1}$$

$$\approx m - 5\log_{10}\left(\frac{r_{\oplus} r_{\odot}}{r_0^2}\right) \tag{1.2}$$

where m is the apparent magnitude of the object, $r_0 = 1$ au $= 149,597,871$ km is the reference distance, and $q(\alpha)$ is the phase function (typically taken to be equal to one for TNOs).

Because TNOs are generally too distant and/or too small to be resolved in Earth- or space-based telescopes, it is impossible to directly measure the size distribution. Instead, the H distribution serves as a proxy for the size distribution, with the two related by the albedo of the objects.

The previous paragraphs described a specific type of observational bias known as *flux bias*, where surveys preferentially discover near and bright TNOs. Other sources

of observational bias include (Kavelaars et al., 2008):

- *Pointing bias* – the on-sky location of a survey sculpts the parameter space of TNOs sampled by the survey, in sometimes subtle ways. It is clear that an object will only be discovered by a survey if it falls within an exposure of that survey. However, a more subtle example of pointing bias can be seen by noting that an object of inclination i spends more time near ecliptic latitudes of $\pm i$ than near zero. Since most TNO surveys focus near the ecliptic, where there are more objects to find, this produces a bias toward better sampling of low-i populations and worse sampling of high-i populations. As the relative ratio of cold to hot TNO populations is of interest when modeling Neptune's migration through the Kuiper belt, pointing bias can inadvertently skew preferred migration models if not accounted for.

- *Ephemeris bias* – to enable tracking and recovery of an object discovered by a survey, an assumed orbit can be fit to an arc of hours or days to predict future positions and inform future survey pointings. This assumed orbit is generally circular. However, more extreme objects with high eccentricities, for example, rapidly diverge from the assumed orbit and can be lost if not followed up within an adequate amount of time. This source of bias can be corrected for by designing a blind survey in which the targeted area of sky is visited repeatedly.

- *Detection bias* – the temporal separation of successive images of a region of sky determines the maximum distance at which objects can be discovered. In order to be noticed as a possibly moving object, the object necessarily must have moved more than one resolution unit (typically $\sim 1''$ for ground-based surveys) between successive exposures of the same target region. For example, one exposure every ten minutes would be sufficient to detect main belt asteroids,

which can move 60″ in an hour. However, TNOs move at 5″ per hour or less, and their motion would not be detectable in such a tight cadence.

The use of a survey simulator can be leveraged to account for all biases of a survey. In this method, a candidate TNO orbit is generated together with an absolute magnitude, defining its position and apparent magnitude at the date-time of every survey exposure. Because the exposure limiting magnitudes are known for a characterized survey, it is straightforward to determine whether a TNO would have been detected by a survey. In this way, models of TNO populations can be forward-biased and compared to real survey detections, thereby enabling constraints on migration models of the giant planets. The limiting magnitudes and survey pointings for DES are known, and I use a survey simulator extensively throughout this work to study DES detections in the context of the full Solar System.

1.3 The Largest TNOs: Dwarf Planets

The apparent magnitude of an object is a strong function of its size and distance. The objects that are bright enough to study in detail are often also the largest objects. It is no coincidence that the asteroid belt (at heliocentric distances of 3–5 au) is much more completely studied to small object sizes than the trans-Neptunian belt (at heliocentric distances of 30–50 au).

The apparent magnitude of an object also strongly depends on its geometric albedo, defined as the ratio of an object's actual brightness at zero phase angle to that of a flat, fully reflecting, diffusively scattering disk (Stansberry et al., 2008). Measurements of a point source in visible wavelengths alone are not sufficient to uniquely determine both an object's size and albedo, since visual brightness does not necessarily correlate with size – one cannot distinguish between a small, shiny object and a large, dark object with visual brightness alone. If the object is large enough to obtain

thermal measurements, however, then this degeneracy can be broken.

An object's albedo, p, determines how much light is reflected from the surface and consequently, how much light is absorbed by the object. Furthermore, the amount of light absorbed by an object affects its equilibrium temperature and therefore its thermal flux. Because the object's albedo affects its apparent flux at both optical and thermal wavelengths, obtaining measurements in both regimes allows for the unique determination of both albedo and size. The temperature of an object in global radiative equilibrium is determined by setting the incoming radiation power to the object equal to the emitted power from the object, $P_{in} = P_{out}$, with

$$P_{in} = F \cdot 4\pi R^2 \cdot (1-p) \tag{1.3}$$

$$= \frac{L}{4\pi a^2}(1-p)\pi R^2 \tag{1.4}$$

$$= \frac{R^2}{a^2}(1-p)\frac{L}{4} \tag{1.5}$$

where F is the flux received by the object from the Sun, R is the object's radius, $L = \sigma T_s^4 \cdot 4\pi R_s^2$ is the Sun's total luminosity (where σ is the Boltzmann constant, T_s is the effective temperature of the Sun, and R_s is the radius of the Sun), and a is the object's semimajor axis. The emitted power from the object is given by

$$P_{out} = \epsilon\sigma T_{eq}^4 \cdot 4\pi R^2 \tag{1.6}$$

where ϵ is the emissivity of the object and T_{eq} is the object's equilibrium temperature. Setting $P_{in} = P_{out}$ yields

$$T_{eq}^4 = \frac{(1-p)}{4\epsilon}\left(\frac{R_s}{a}\right)^2 T_s^4 \tag{1.7}$$

An object's thermal flux can be related to its equilibrium temperature if a surface temperature distribution is known. However, the surface temperature distribution is generally not known, especially for objects at Kuiper Belt distances, and so requires

that assumptions about the object's rotation and surface properties be made. Radiometric measurements are possible only for a small subset of TNOs because the 50K temperatures typical at Kuiper Belt distances render many TNOs too faint to observe at thermal wavelengths.

Once an object's albedo is known, one can relate the apparent magnitude (and thus absolute magnitude) to a diameter. Because the sample of TNOs for which albedos are known is quite limited, consisting mostly of the largest TNOs, it is typical to assume a value of 4% in order to estimate object size (Lykawka & Mukai, 2005). However, the dwarf planets with measured albedos have shown varied values of this parameter: Eris, at $96\%^{+9}_{-4}$ (Sicardy et al., 2011); Sedna at $32 \pm 6\%$ and 2010 EK_{139} at $22\%^{+2}_{-5}$ (Pál et al., 2012); and 2002 UX_{25} at $10 \pm 1\%$, Orcus at $23 \pm 2\%$, Salacia at $4.2 \pm 0.4\%$, and Quaoar at $12 \pm 1\%$ (Brown & Butler, 2017).

Dwarf planets are particularly interesting objects to study because they are likely large enough to have held on to volatiles and ices during their lifetimes, a claim supported by their generally higher albedos. These ices will reflect more light than the rocky terrain of the object, which is presumably why dwarf planets appear to exhibit higher albedos overall. A complete census of albedo and size measurements for objects > 400 km will elucidate the surface properties of these objects, for which it is often not feasible to obtain full reflectance spectra. Furthermore, it is important to keep in mind the strong variation in albedos exhibited by > 400 km-class objects when estimating the sizes of objects discovered in a survey – it is often imprecise to assume that a particular value of albedo accurately describes objects too faint (and thus too small) to be discovered by a survey.

1.4 On the Hypothetical Distant Planet in the Solar System

The recent proposal of a new, unseen planet in the distant Solar System has garnered substantial interest from both the scientific community and the general

public. Trujillo & Sheppard (2014) first noted an apparent alignment in the arguments of perihelion around 0° of the most distant objects, with $a > 150$ au and $q > 30$ au. These objects have since come to be known as "extreme" TNOs, or ETNOs. Trujillo & Sheppard (2014) argued that observational bias could not explain this apparent clustering because a survey should be as likely to find an object with $\omega = 180°$ as it is to find an object with $\omega = 0°$. They proposed that a massive, exterior planet could force such an alignment. Batygin & Brown (2016) developed the hypothesis further by noting an additional clustering in the longitudes of ascending node, calling their exterior perturber "Planet Nine." The past three years have seen increased focus on searching for new ETNOs, and the sample size is now a couple dozen with $a > 150$ au. With the information added by the ETNOs discovered in the past three years, Batygin et al. (2019) revised the Planet Nine hypothesis to its current form: a $\sim 5M_{\oplus}$ object with $a = 400 - 800$ au, $e = 0.2 - 0.5$, and $i = 15 - 25°$. Figure 1.3 shows the orbits of the known ETNOs together with the proposed orbit for Planet Nine.

The objects used to argue for the Planet Nine hypothesis have been discovered by a variety of surveys, the majority of which have not reported their exposure pointings and limiting magnitudes. This makes precise studies of the effects of observational bias on the apparent orbital clustering of the ETNOs impossible. Furthermore, the observational bias of such distant and eccentric objects are much more subtle and severe than for a garden-variety cold classical TNO, for example. In particular, such eccentric objects are generally only detectable very near perihelion. Additionally, many TNO surveys have focused near ecliptic latitudes less than 10°. The combination of these two factors results in the preferential detection of ETNOs with $\omega \sim 0°$. Shankman et al. (2017) used the OSSOS sample of ETNOs together with the OSSOS survey simulator to argue that observational bias completely accounts for the apparent orbital clustering of the ETNOs, eliminating the need for a new, distant planet. Conversely, Brown (2017) and Brown & Batygin (2019) use the discovery circumstances

Figure 1.3: A depiction of the known ETNOs with $a > 250$ au and $q > 30$ au plotted with the proposed orbit for Planet Nine (teal ellipse, $a = 500$ au, $e = 0.25$, $i = 20°$). Gray objects denote ETNOs reported to the MPC as of 2019 April 14. The objects can be roughly divided into aligned (with Planet Nine) and anti-aligned populations. The objects discovered by DES are denoted by the purple colors: 2013 RF_{98}, 2015 BP_{519}, ws301g157, and ws302g153.

and current census of objects reported to the Minor Planet Center to estimate the observational biases of each ETNO, concluding that there is a $< 1\%$ chance that the observed clustering actually arises from a uniform underlying distribution in orbital angles.

1.5 Thesis Outline

In this thesis, I present an overview of the Dark Energy Survey Solar System effort and describe results that have come from the first five years of this work.

In Chapter II I describe DES, its survey strategy, the construction of transient catalogs, the moving object pipeline, and the procedure for classifying detected objects into different dynamical populations. I conclude the chapter with an investigation into how the survey's power could be expanded by the use of digital tracking to recover objects fainter than the single exposure limiting magnitude. I focus on Neptune Trojans for this initial investigation, but the general procedure can be expanded to any TNO population.

Chapter III reports the discovery and thermal analysis of a dwarf planet candidate discovered using DES, 2014 UZ_{224}, and is based on Gerdes et al. (2017). I use observations at visual wavelengths taken by DES in addition to observations at submillimeter wavelengths taken by ALMA to uniquely determine the object's diameter and albedo.

Chapters IV and V comprise the description of the DES Survey Simulator and its applications to date. These two chapters are based on a paper to be published as Hamilton et al. (2019). In Chapter IV I discuss the design of the Survey Simulator and summarize its applications to characterize three new ETNOs, two new high-inclination Neptune Trojans, and the Plutino population detected by DES. Chapter V examines the evidence for a massive, distant planet in the Solar System motivated by the apparent orbital clustering of the ETNOs using the self-contained dataset of

Table 1.1: Symbols and abbreviations frequently used throughout this work

Orbital Elements	
a	semimajor axis
e	eccentricity
i	inclination
ω	argument of perihelion
Ω	longitude of ascending node
ϖ	longitude of perihelion
M	mean anomaly
H	absolute magnitude
Abbreviations	
TNO	trans-Neptunian object
ETNO	extreme trans-Neptunian object
KB	Kuiper belt
DES	Dark Energy Survey
DECam	Dark Energy Camera
MMR	mean motion resonance

DES ETNOs.

Finally, in Chapter VI I summarize this work and offer comments on future outlooks.

CHAPTER II

Solar System Science with the Dark Energy Survey

2.1 Overview of the Dark Energy Survey

The Dark Energy Survey (DES, Abbott et al. 2006) is a cosmological survey of 5000 deg^2 of the Southern Hemisphere sky in optical wavelengths using the Dark Energy Camera (DECam, Flaugher et al. (2015)) on the 4-meter Blanco telescope at the Cerro Tololo Inter-American Observatory in Chile. To accomplish its primary goal of measuring the dark energy equation of state, in addition to other cosmological parameters, the survey aimed to take ten tilings in each of the $grizY$ bandpass filters. These five filters span a wavelength range of $\sim 400 - 1100$ nm, which allows for the calculation of photometric redshifts of the hundreds of millions of galaxies DES observed.

DECam is a prime-focus, 570 mega-pixel optical imager with 62 $2k \times 4k$ fully-depleted, red-sensitive CCDs spanning a 3 deg^2 field of view. The camera further has 12 $2k \times 2k$ CCDs used for guiding and focus. The pixels in each CCD are $15\mu\text{m} \times 15\mu\text{m}$ and have a plate scale of $0.263''$ per pixel. Two and a half of the 62 CCDs failed during the course of the survey and were not used for science operations after their failure. Fortuitously, one of the failed CCDs did come back online toward the end of Y5. DECam will remain available as an instrument on the Blanco telescope as part of a deal between DES and CTIO that allowed DES full use of the telescope for the

duration of the survey.

To achieve its cosmology goals, DES was nominally awarded 525 nights of observing from August 2013 to February 2018. Science Verification (SV) observations were taken from November 2012 through February 2013 and cover 250 deg^2 to the full survey depth. While SV was intended to be a test data set, it has proven to be useful for weak gravitational lensing studies (e.g. Abbott et al. 2016a). Years 1-5 of the survey consisted of two complementary sub-surveys. The Supernova Survey (DES-SN) imaged 10 individual DECam fields, amounting to $\sim$27 deg^2 in total, on an approximately weekly cadence in the *griz* bandpass filters. Eight of the ten SN fields are "shallow" with successive images in the *griz* bands taken over a 15-minute interval to an r-band single exposure limiting magnitude of $m_r \sim 23.8$. The remaining two fields are "deep" with exposure sequences ranging from 10 minutes in g-band to over an hour in z-band and reach an r-band single exposure limiting magnitude of $m_r \sim 24.5$. The Wide Survey covered the full survey footprint in the *grizY* bandpass filters to a single-exposure limiting magnitude of $m_r \sim 23.5$, with the goal of achieving 10 tilings per filter by the end of survey operations. The *griz* exposures were 90s for the duration of the survey, while exposures in the Y band were extended from 45s to 90s after the completion of Y3. Table 2.1 summarizes the DES exposure strategy.

The full survey depth was not attained in the nominally awarded period due to a combination of factors, most notably the El Niño event of 2015–2016. As a result, DES was awarded 52 additional nights from September 2018 to January 2019 to complete the full survey, termed Year 6. Motivated by the need to complete all ten tilings in each bandpass in the Wide Survey, there were no DES-SN exposures taken during Y6. Furthermore, because observations in the Y-band could be taken in worse conditions than for the other bandpasses (e.g. during wispy clouds, in other poor seeing conditions, or with a bright moon), Y-band observations were completed by the end of Y5. Thus, only *griz* observations were needed in Y6. Figure 2.1 shows

Table 2.1. Exposure Summary of the DES Supernova and Wide Surveys.

	Band	T_{exp} (s)	N_{exp}	Total T_{exp} (s)
SN-Shallow	g	175	1	175
	r	150	1	175
	i	200	1	200
	z	200	2	400
SN-Deep	g	200	3	600
	r	400	3	1200
	i	360	5	1440
	z	330	11	3630
Wide	$griz$	90	1	90
	Y^*	45	1	45
	$Y^\dagger$	90	1	90

*SV–Y3 only

†Y4–Y5 only

the exposure coverage for Years 1-6 of DES. Note that this figure shows all bands together.

2.1.1 DES as a Solar System Survey

DES's combination of area and survey depth makes it a powerful cosmological survey. In order to achieve the deep co-added images needed to do precision cosmology measurements, each field is visited repeatedly over the duration of the survey. While repeated visits are not necessarily spaced evenly in time (aside from DES-SN exposures) this strategy also makes DES well suited to study and discover minor bodies in the Solar System (Dark Energy Survey Collaboration et al., 2016). In particular, the footprint's location largely off of the ecliptic plane makes DES especially powerful for identifying new members of high-inclination Solar System populations, such as in the scattered disk in the Trans-Neptunian region. These populations have traditionally been less well-studied because most previous Solar System surveys have focused primarily along the ecliptic, where the object density is highest (e.g the Deep Ecliptic

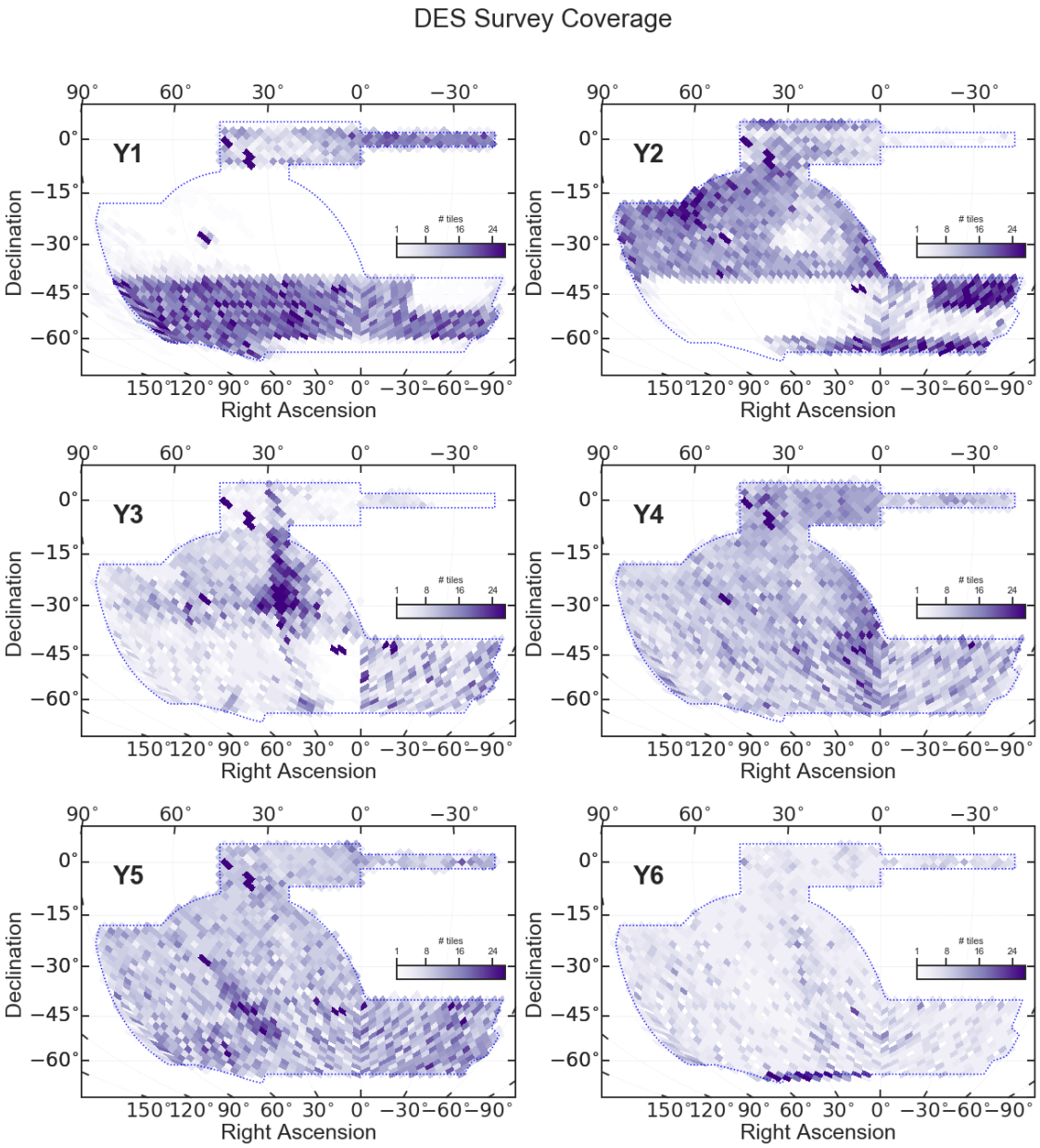

Figure 2.1: Coverage maps of DES for Year 1 (Y1) through Year 6 (Y6). Darker color indicates more visits to a region of sky, while lighter color indicates fewer visits. The white regions indicate areas of the footprint that did not have exposures taken of that region in the given year. Because we use detections from all *griz* bands for object discovery, these coverage maps include all four bands simultaneously.

Survey (DEcS, Millis et al. 2002; Elliot et al. 2005), the Canada-France Ecliptic Plane Survey (CFEPS, Kavelaars et al. 2009; Petit et al. 2011), or the Outer Solar System Origins Survey (OSSOS, Bannister et al. 2016, 2018)).

Early efforts to detect Solar System objects using DES began in the DES-SN fields, two of which fall at moderate ecliptic latitudes. Because the goal of DES-SN was to accurately sample SN lightcurves, these fields were visited approximately every 7-10 days. This regular cadence simplified the early Solar System moving object search, as the uncertainty in the orbital elements (and therefore positions) of objects discovered would be mitigated by the weekly observations. However, DES's power as a Solar System survey lies in its broad coverage of 1/8th of the sky through the Wide Survey, and we are now able to process transient observations from the entire survey area.

We have previously reported on the discoveries of new L4 Neptune Trojans, including the two highest inclination, stable Neptune Trojans yet discovered (Gerdes et al., 2016; Lin et al., 2019); a new distant dwarf planet candidate (Gerdes et al., 2017); two new $a \sim 171$ au TNOs with similar orbital elements (Khain et al., 2018); and a new ETNO, defined in this work as objects with $a > 250$ au and $q \gtrsim 30$ au, with the highest inclination yet observed in this population (Becker et al., 2018). The following sections provide more detail on how these objects, and many others, were detected with DES.

2.2 Construction of the Transient Catalog

In this Section, I describe the procedure by which the transient catalog used to search for Solar System objects is produced. I also describe the iterations the pipeline has gone through until present day.

2.2.1 Difference Imaging Transients

To obtain a catalog of transient observations, we employ difference imaging techniques initially developed for DES-SN (`DiffImg`, Kessler et al. 2015) that have since been expanded to the Wide Survey. As described in Kessler et al. (2015), template images of each search region are constructed using images at previous epochs of each SN field. Transient objects are then found by image subtraction, and artifacts and low-quality detections are rejected using machine learning methods described in Goldstein et al. (2015). The surviving sources are compiled into a transient catalog.

The shallow DES-SN fields are completed in a *grizz* sequence, and each band is processed separately. Therefore, the shallow fields are naturally a transient catalog at a single epoch. Conversely, nominal processing of the deep DES-SN fields, which have multiple exposures in a single band, coadds the exposures by band before executing `DiffImg`. The fastest-moving TNOs we are concerned with are the Neptune Trojans, which at 30 au can move as fast as 5″ per hour. Once coadded, the deep DES-SN fields can have total exposure lengths of 600–3630 seconds (i.e. up to one hour, see Table 2.1). A Neptune Trojan moving at 5″ per hour will smear into a 5″ streak in the longest coadd, which is significantly wider than the $\sim 1''$ point-spread function of a typical DES exposure. Such an object may be detectable in individual deep DES-SN exposures but be lost in the coadd. Therefore, `DiffImg` in the deep DES-SN fields is executed on each exposure individually in addition to the full coadd.

The main difference between the SN and Wide Survey difference imaging is that the construction of template images in Wide Survey processing uses general regions of sky rather than the particular DECam tiling. This distinction is made because the same stars and galaxies fall near the same pixels of DECam in SN exposures, while the Wide Survey consists of overlapping tilings. Thus, template images must be treated carefully. The specifics of this procedure are beyond the scope of this thesis. Once template images are constructed, `DiffImg` proceeds in the same way as

the nominal SN difference imaging processing.

To date, $\sim$ 40% (41,140 *griz* exposures) of the final anticipated data set from DES has been processed through `DiffImg`. We do not include Y-band exposures because (1) they can have limiting magnitudes up to $\sim$ 1 magnitude brighter than the other bands and (2) all Y-band exposures through Year 3 were only 45 seconds. Figure 2.2 shows the exposures processed through `DiffImg` in the context of the DES footprint. Regions at low to moderate ecliptic latitudes were prioritized because the Solar System object density is higher there. Because our data set uses the exposures in the Wide Survey that have been processed through `DiffImg`, I refer to the data set as "`wsdiff`" throughout this thesis.

2.2.2 Single-Epoch Catalog Transients

While powerful, the `wsdiff` catalog requires immense amounts of computing- and person-hours to produce — a single CCD in a shallow SN or Wide Survey image takes about 10 minutes to process (Kessler et al., 2015). CCD failure rates of $10-15\%$ are also common, so someone must monitor the computing jobs to fix errors or restart processing. The pipeline can fail for a variety of reasons, including but not limited to insufficient density in the star catalogs used to perform photometry measurements or a failure in determining the image kernel so that images can be transformed and subtracted pixel by pixel. The computing- and person-time required for `DiffImg` processing is a large part of the reason that only 40% of data taken from SV–Y5 has been processed.

Further, because `DiffImg` uses some of the image flux to accurately gauge the background flux counts, there is a small loss in achievable exposure depth after `DiffImg` has been run. This poses a significant problem for the DES TNO search – the number density of TNOs by apparent magnitude behaves as $N(< m) \sim 10^{0.8m}$, meaning that the majority of detectable objects fall near the limiting magnitude of

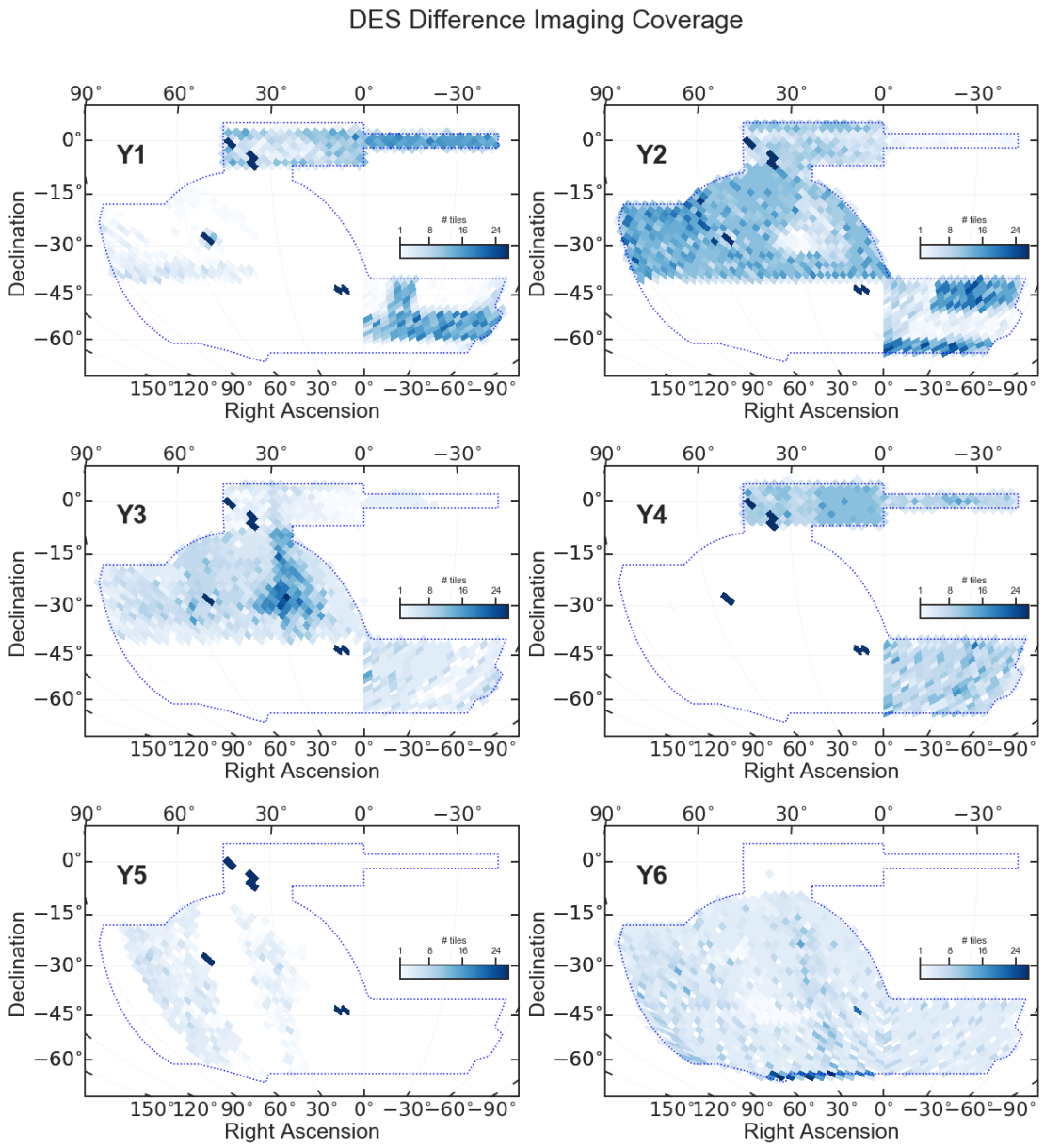

Figure 2.2: Coverage maps of the DES `wsdiff` data set from DES Year 1 (Y1) through Year 6 (Y6). Darker color indicates more visits to a region of sky, while lighter color indicates fewer visits. The white regions indicate areas of the footprint that have not been processed through `DiffImg` at all. Nightly `DiffImg` was instantiated partway through Y5, which is why only part of Y5 and most of Y6 are complete. The supernova field exposures in Y5 have been processed through `DiffImg`, and only Wide Survey images were taken in Y6. However, only `wsdiff` exposures through Y4 have been searched using the TNO linking pipeline. Because we use detections from all *griz* bands for object discovery, these coverage maps include all four bands simultaneously.

the exposure. A loss of even 0.3 mags can translate to almost a factor of two difference in the number of detectable objects.

Motivated by these problems, a new transient catalog has been developed by Pedro Bernardinelli of the University of Pennsylvania. Instead of performing image subtraction on each search image using a template image, the new catalog is produced by comparing the locations of sources in the search image to those in a deep coadd image of the same region. The signal-to-noise ratio (SNR) of stationary sources will increase in the coadd images, while transient sources will be removed. Thus, common sources between the coadd and search images are stationary sources, while any other sources are transient. The resulting single epoch (SE) catalog is then ready to be processed through a moving object pipeline (see Section 2.3). The specific details of how the SE catalog is produced will be described in Bernardinelli et al. (2019). Processing of the SE catalog has begun and is expected to be complete by the end of Summer 2019. Between the gains in limiting magnitude, ability to process the entire survey area, and CCD failure no longer being a concern, the output of the SE catalog could be as many as 1000 TNOs (D. Gerdes, personal communication).

2.2.3 Characterizing Detection Efficiency Using Injected Fake Objects

In order to turn our discoveries into meaningful science results about Solar System formation, we must understand how efficiently we are able to reconstruct moving transients with DES. To accomplish this we must determine the efficiencies of both detecting objects and of linking individual observations over several nights into a single orbit. To address both of these cases, I make use of generated fake TNOs.

The DES SN group's `DiffImg` software contains the necessary tools for embedding stationary fake transients (fakes) into real DES images (see Kessler et al. 2015 for details on the procedure). The output of `DiffImg` reveals how many fakes were detected after being subject to real, variable effects such as the lunar phase, variable seeing,

nearby bright stars, etc. I expanded `DiffImg`'s existing tools to handle fake moving objects, e.g. objects in a different on-sky position in every exposure, in addition to fake supernovae that remain stationary but change in apparent magnitude.

The generated fake TNOs fall into two categories:

1. **Garden-variety TNOs:** $a = 40 - 60$ au, $q > 30$ au, $i < 60°$, and H such that $m < 27$.

2. **Distant, detached TNOs:** $a = 200 - 600$ au, $q > 60$ au, $i < 120°$, and H such that $m < 27$.

For each exposure midpoint (equal to the exposure start time plus half of the total exposure time), I calculate each object's position. I then write the on-sky coordinates and apparent magnitudes of detections that fall within a DECam field of view of the pointing coordinates to a csv file that is read in by `DiffImg`. The object was considered detected in an exposure if the `REJECT` flag from `DiffImg` was equal to 0, indicating the observation passed all quality checks, and if the AUTOSCAN (Goldstein et al., 2015) machine learning score was > 0.5, indicating that detection sufficiently resembled a point source. Figure 2.3 shows the observed apparent magnitude versus injected apparent magnitude for fakes implanted into the SDSS Stripe 82 region in DES Y1–Y4.

2.3 Object Detection

A comprehensive description of the DES moving object detection software is forthcoming, but I provide an overview here. Once a transient catalog is constructed, we search for pairs of observations temporally separated by 60 nights or less whose direction and rate of motion are consistent with that of Earth parallax. These pairs are subsequently extended to triplets via the same process. We then attempt to connect pairs and triplets by transforming to a heliocentric coordinated system such that the

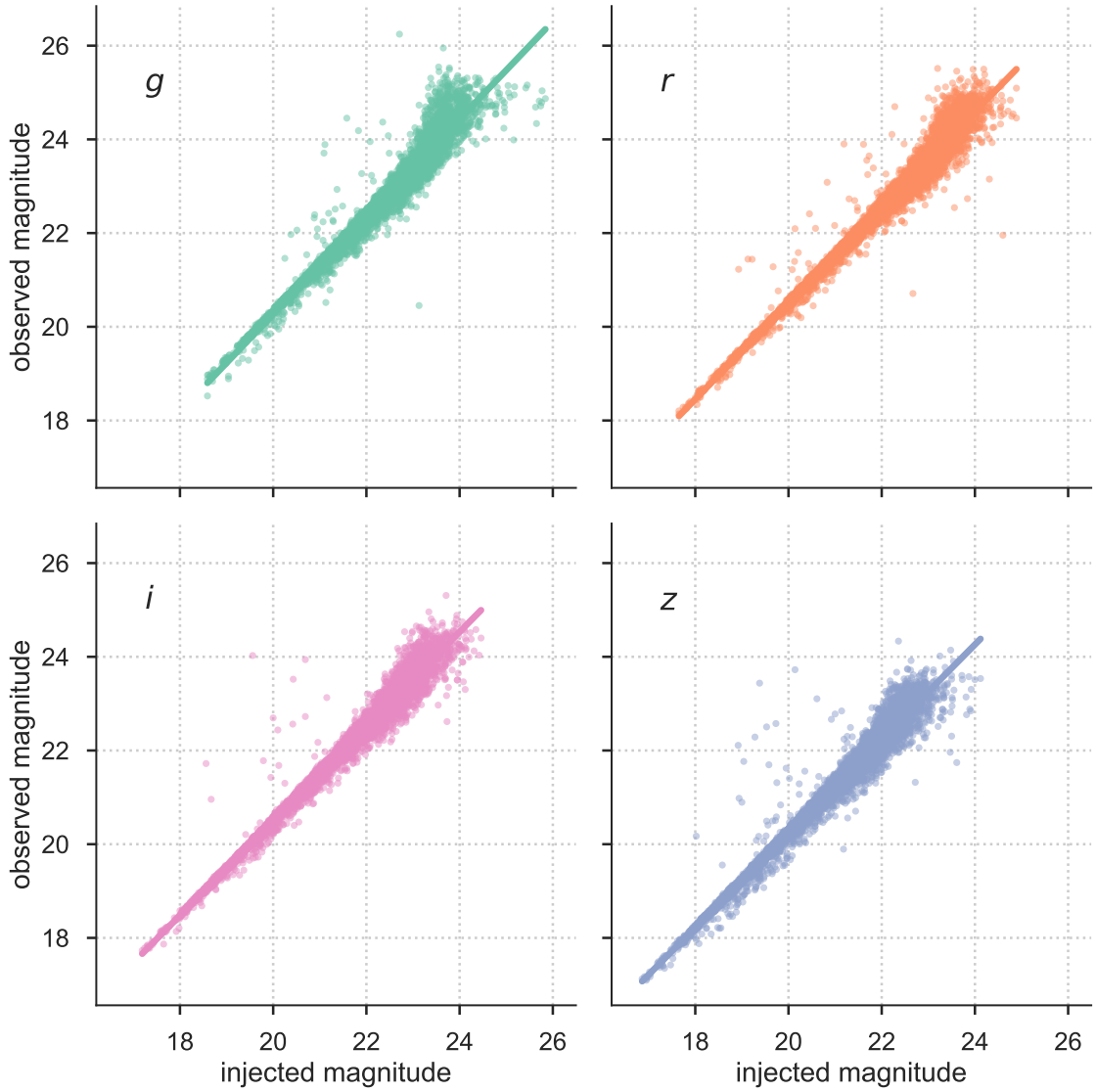

Figure 2.3: The observed apparent magnitude versus injected apparent magnitude for fakes implanted into the exposures of the equatorial SDSS Stripe82 region in DES Y1–Y4. These plots include only the observations considered detected as defined in the text. This region lies at low ecliptic latitudes and so has the highest density of implanted Solar System object detections. `DiffImg` reconstructs the apparent magnitude very well until the object's apparent magnitude approaches the limiting magnitude of the exposure (typically 23.5–24).

object's motion is no longer subject to Earth's parallax motion and its trjactory is instead a straight line at roughly constant ecliptic latitude. Candidate orbits can then be fit to a Keplerian orbit using a Python wrapper[1] around the `orbfit` software developed by Bernstein & Khushalani (2000). Orbit solutions are kept if the per-degree-of-freedom $\chi^2 < 2$.

DES is primarily a cosmological survey whose original design, aside from the supernova survey, had little need for any temporal resolution in order to search for transient objects. Thus, the temporal cadence for repeated visits to a particular on-sky location can be sporadic and the DES moving object search pipeline does not rely on the recovery of "tracklets," a strategy commonly employed by dedicated Solar System surveys. Instead, the DES moving object search begins with an input catalog of single-epoch transient detections, which are then searched and linked into orbits via the procedure outlined above. As of writing, DES has detected 341 TNOs with at least five observations on at least four nights and a fit to a Keplerian orbit with a per-degree-of-freedom $\chi^2 < 2$. The properties of the TNOs are shown in Figure 2.4 and listed in Table B.1. Their positions in the context of the DES footprint and previously reported TNOs are shown in Figure 2.6.

2.3.1 Object Classification

With 341 TNOs already detected, and many more expected from the new transient catalog described in Section 2.2.2, it was imperative to develop a method to robustly classify the detected objects into different dynamical populations. The criteria for doing so is described in Khain et al. (2019), but I provide a brief overview here. We generate ten clones of each detected object using the best-fit orbit and covariance matrix generated by the linking code. We then run numerical simulations

[1] https://github.com/dwgerdes/pyOrbfit

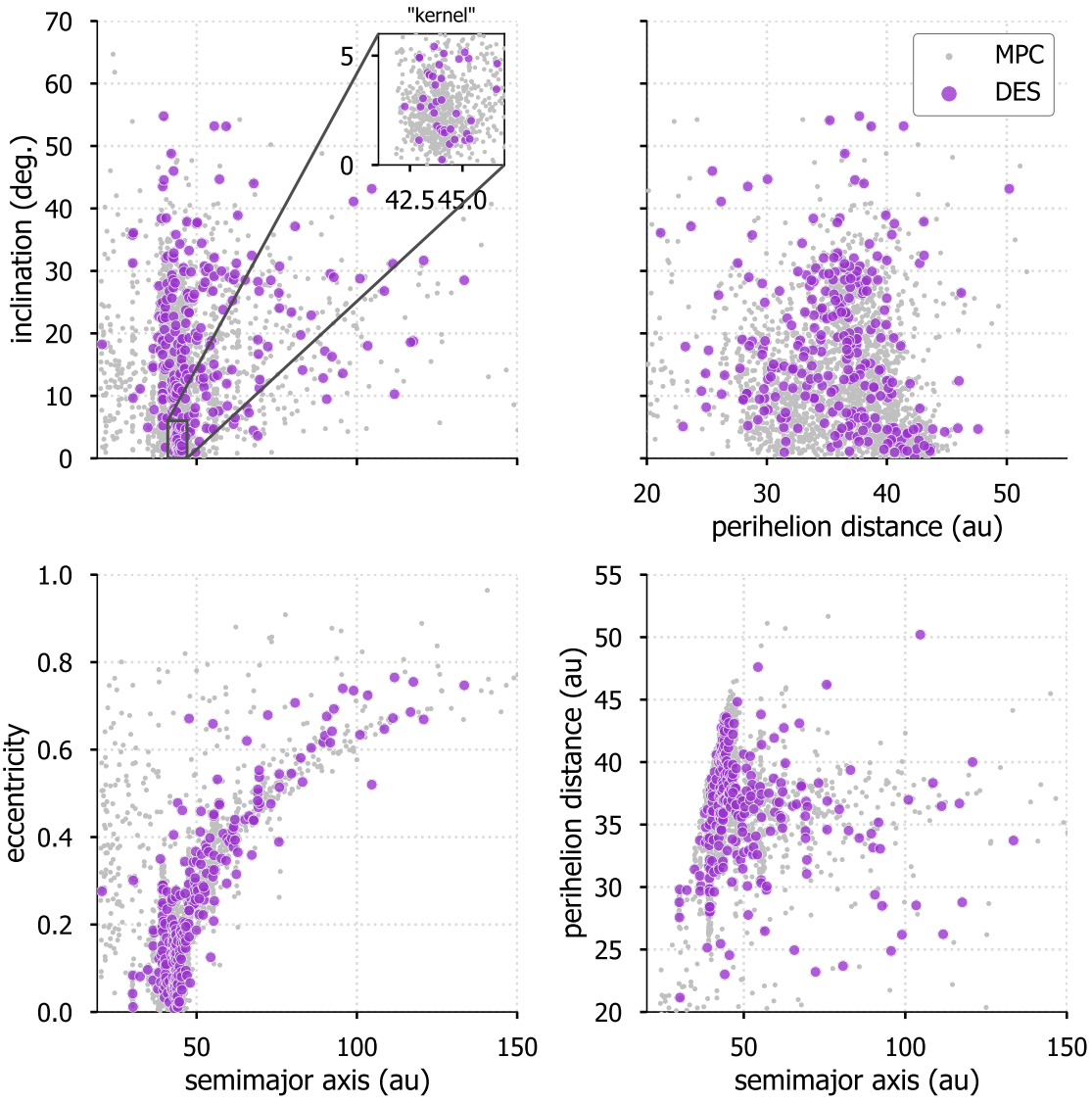

Figure 2.4: Orbital element relationships for the 341 DES objects (purple) and objects from the MPC (gray). Objects in these plots have $a, q > 20$ au. While DES does have some coverage of the low-eccentricity, low-inclination "kernel" of cold classical Kuiper Belt Objects (inset in top left panel), the bulk of DES detections are at $i > 10°$, reflecting DES's coverage at high ecliptic latitudes.

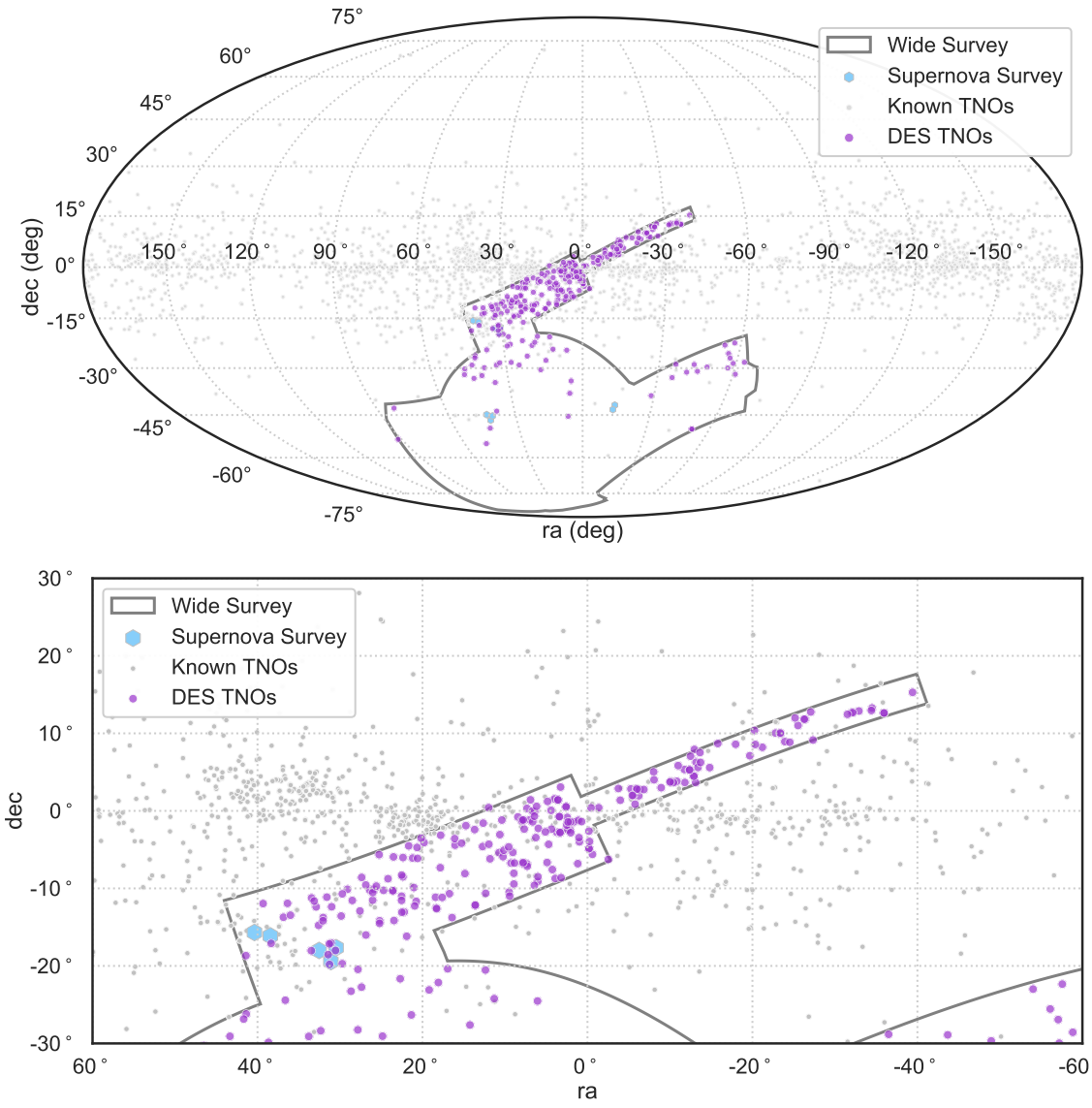

Figure 2.6: *Top:* The Dark Energy Survey footprint in ecliptic coordinates with all known TNOs as of March 2018. All TNOs are plotted at their discovery positions. The DES Wide Survey area is denoted by the dark gray outline, and the SN fields are shown as the blue hexagons. Gray points represent all TNOs in the Minor Planet Center database, while purple points show DES detections. *Bottom:* Same as *Top*, but zoomed in on the low ecliptic latitude region covered by DES, $-60° < \mathrm{ra} < 60°$ and $-30° < \mathrm{dec} < 30°$.

for 10 Myr.[2] The order in which the dynamical classes are listed below is the order they are considered in the classification algorithm.

- **Comets** are objects with a Tisserand parameter with respect to Jupiter of $T_J \left(= \frac{a_J}{a} + 2\sqrt{\frac{a}{a_J}\left(1 - e^2\right)} \cos i\right) < 3.05$ and perihelion distance $q < 7.35$ au.
- **Oort Cloud objects** are those with $a > 2000$ au.
- **Centaurs** are objects with perihelion distances within the orbit of Neptune, $q < a_N$, and so experience strong interactions with the giant planets.
- **Resonant objects** are objects with periods that are an integer ratio to that of Neptune. An object in a $p : q$ resonance has a libration argument defined by

$$\phi = p\lambda_N - q\lambda + r\varpi_N + s\varpi,$$

  where $p, q, r,$ and s are integers that satisfy the relation $p - q + r + s = 0$; λ_N and λ are the mean longitudes of Neptune and the object, respectively; and ϖ_N and ϖ are the longitude of perihelion of Neptune and the object, respectively.
- **Scattering disk objects** are objects whose semimajor axes change by more than a few au over the course of the simulation because they are actively scattering off of Neptune.
- **Extreme TNOs** are objects with $a > 150$ au and $q > 30$ au.
- **Detached objects** are non-scattering objects beyond Neptune's gravitational influence with eccentricity $e > 0.24$ and generally with large perihelion distances.
- **Classical belt objects** are what remains after all previous categories are examined. They are non-resonant, non-scattering objects with $e < 0.24$.

[2]For long-period objects ($a \gtrsim 100$ au), 10 Myr may not be long enough to fully capture the object's dynamical behavior. For these objects, the integration time is increased to 100 Myr.

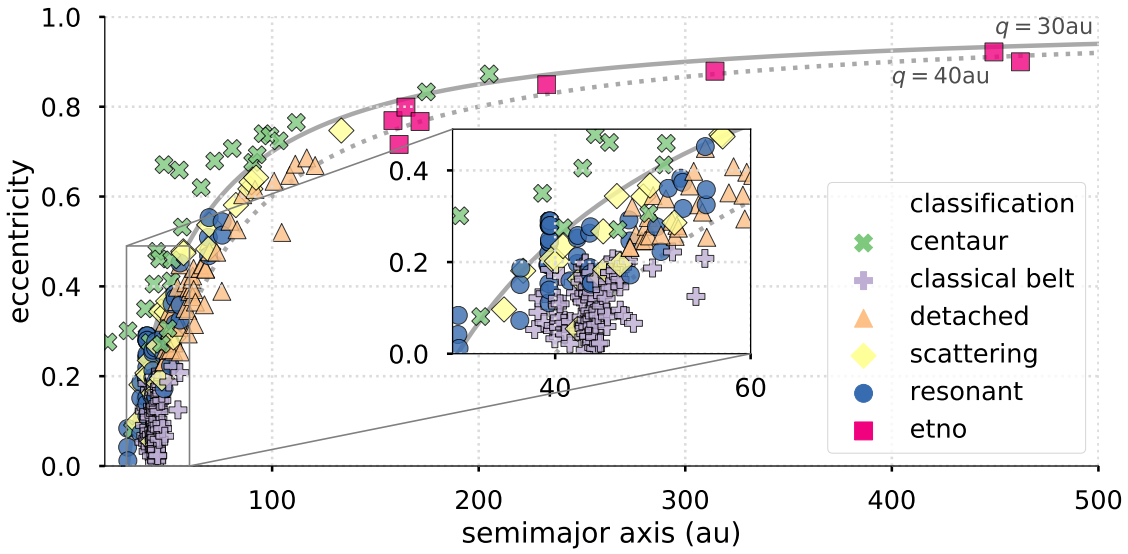

Figure 2.7: The eccentricity versus semimajor axis of the objects detected by DES. Each object class is denoted by a different marker and color. The solid line indicates a perihelion distance of 30 au, while the dotted line indicates a perihelion distance of 40 au. The zoomed inset offers a better look at the TNOs discovered by DES with semimajor axis within the Kuiper Belt ($a \approx 30 - 55$ au). The classification procedure and results are detailed in Khain et al. (2019), and this figure is modeled after Figure 7 in that paper.

Figure 2.7 shows the eccentricity versus semimajor axis for each of the DES TNOs.

2.4 Expanding the Discovery Power of DES: A First Look at Digital Tracking

The 23.5 and 24.5 limiting magnitude depths in the r-band of the SN fields is an advantage DES already has over previous TNO surveys, but it is possible to achieve even fainter limiting magnitudes using a technique called "digital tracking" (Bernstein et al., 2004; Heinze et al., 2015). In conventional processing of SN field data, exposures are stacked (or "co-added") in sky coordinates. Transient objects are then identified by passing the image stack through `DiffImg`. In digital tracking, images are shifted and co-added in many iterations according to various different orbital trajectories,

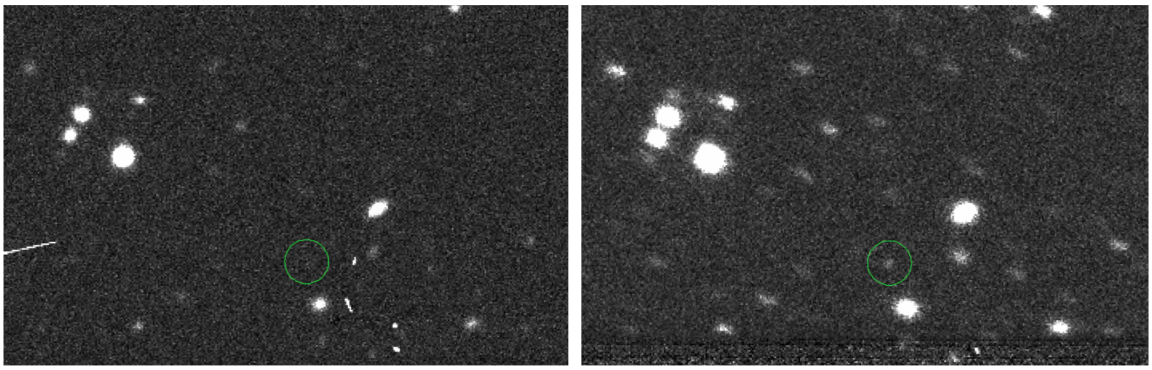

Figure 2.8: Demonstration of digital tracking for the $a = 360$ au, $q = 36$ au TNO 2013 RF_{98}, which was discovered in the deep SN-X3 field of DES with apparent magnitude $m_r = 24.4$. The left panel shows a single 330s z-band image in the SN-X3 field, and 2013 RF_{98} is hardly visible. The right panel shows a digitally-tracked image of the 11 consecutive 330s z-band images in the same SN-X3 sequence, and 2013 RF_{98} is now detected at 9σ significance.

defined in a grid of total hourly motion and velocity vector direction. This results in effective exposure times on the order of one hour that, once we have found a trial trajectory matching that of a real object, reveal bodies hidden in individual exposures. Figure 2.8 shows the power of digital tracking for 2013 RF_{98}, a $m_r = 24.4$ object discovered in the deep SN-X3 field of DES. Additional output of digital tracking includes precise measurements of the positions, motions, and brightnesses of new objects essentially for free.

Because SN field exposure sequences are usually completed within an hour, I can approximate a linear trajectory for a distant object. This makes a full digital tracking analysis easily feasible in the SN fields. I estimate that, for a single night of data, digital tracking will yield nearly a full magnitude of extra depth in both the shallow and deep fields. Assuming that the TNO number density follows a power-law flux distribution $N(< m) \sim 10^{0.8m}$ (Bernstein et al., 2004), this equates to nearly a factor of five increase in the number of TNOs we can discover with DES over the conventional search method.

The most logical place to begin is a search for Neptune Trojans. This population of TNOs is in a 1:1 mean motion resonance with Neptune, orbiting around its L4 and L5 Lagrange points, and is ideal for preliminary studies because Neptune's L4 Lagrange point is currently located near the S and X fields of the DES-SN survey. The Nice II model predicts a sharp cutoff in the Trojan size distribution around 80 km since these objects are theorized to be captured bodies from the planetesimal disk as opposed to collisional fragments. Digital tracking will allow us to probe the Trojans to sizes of approximately 40 km and will give valuable insight into their origins.

The Trojans all orbit approximately 30 au from the Sun, greatly simplifying the parameter space needed for a digital tracking analysis since all objects have approximately the same hourly motion across the sky. Prior to analyzing real data, I first studied a sample of nearly 13,200 fakes generated according to the following distributions of orbital elements:

- a constant at 30 au
- e drawn from the distribution

$$p(e) \propto \begin{cases} e \ \exp^{\frac{-1}{2}\left(\frac{e}{\sigma_e}\right)^2}, & e > e_c \\ 0, & e \leq e_c \end{cases}$$

  where $e_c = 0.12$ and $\sigma_e = 0.044$ (Parker, 2015)

- i drawn from a Gaussian with $\langle i \rangle = 21.9°$ $\sigma_i = 16°$, and $i_c = 60°$ (Parker, 2015)
- ω, Ω, M, H drawn from uniform distributions

To define the grid of possible object trajectories to use in digital tracking, I calculated the positions and rates of motion for each fake for each SN-S and SN-X field exposure in Year 1 of DES (1074 total exposures). This resulted in nearly 211,600 observations after accounting for CCD chip gaps. Because the motion of TNOs on

the sky is dominated largely by Earth's parallax motion, it is more practical to define the grid in terms of total hourly motion and position angle (i.e. the angle from North through East of the hypothetical TNO's velocity vector), rather than the change in on-sky coordinates. Figure 2.9 shows the results of the simulations, color-coded by month. It is clear that the trajectory grid will need to change according to the time of year. Figure 2.11 shows the results of dividing a DES season into approximately two-week-long periods, which is a more reasonable length of time to use a single trajectory grid.

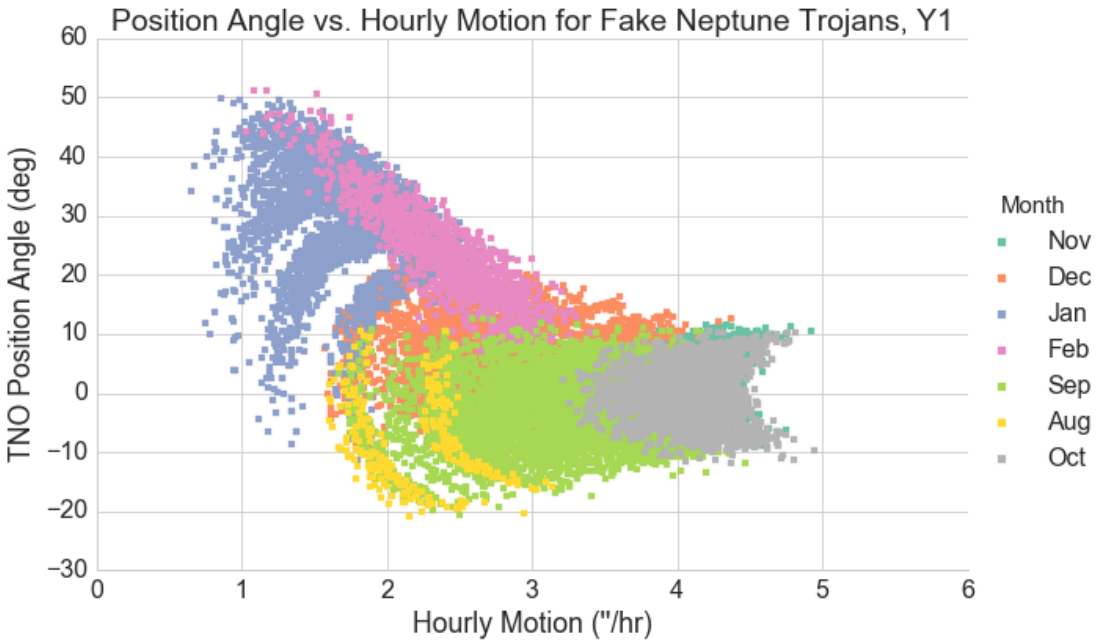

Figure 2.9: Position angle vs. total hourly motion for ∼13,200 fake Neptune Trojans from August through September of 2013 (Year 1 of DES), calculated in ecliptic coordinates. Note that in October and November, when the SN-S and SN-X fields are at opposition, the position angles are near 0° and the total hourly motion is near a maximum.

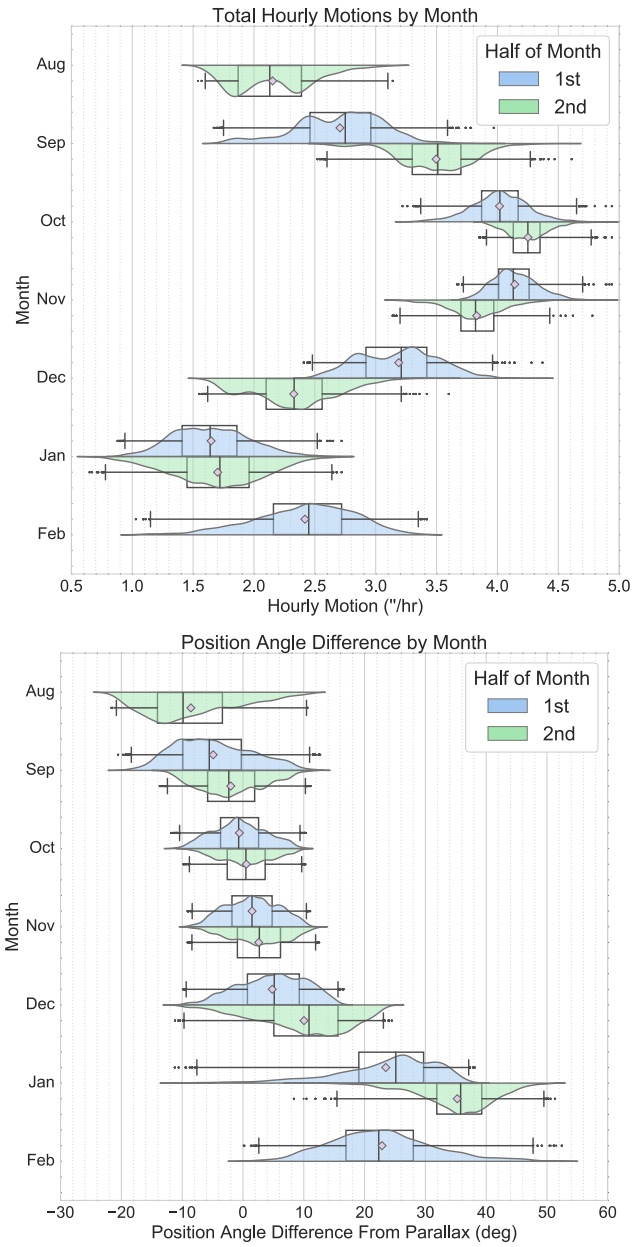

Figure 2.11: *Top:* The variation in total hourly motion during the course of DES Y1. Observations are separated by month and color-coded by the half of the month in which they occur. The violin plots represent the kernel density estimation (KDE). Superimposed are corresponding box plots, with the distribution mean denoted by the purple diamond, and the 3σ confidence interval encompassed by the whiskers of the box plot. *Bottom:* The same as the top plot, now showing variation in the difference of the TNO position angle from the position angle of the parallax vector.

2.5 Summary

In this chapter, I outline DES's potential to be a powerful Solar System survey. The DES survey area largely lies at high ecliptic latitudes, offering a new look at the poorly-studied high inclination populations of the Solar System. We take advantage of the `DiffImg` software already developed by the DES-SN working group to identify and characterize stationary transient objects and adapt it to also be able to characterize moving transient objects. While `DiffImg` has proved to be a powerful dataset for trans-Neptunian object detection, it suffers from lack of person-power, high CCD failure rates, and loss of detection sensitivity. These issues motivated the construction of a new, superior transient catalog based on catalog-level coadds and detections as opposed to image-level subtraction. Processing of this new transient catalog is currently underway.

Once a transient catalog is produced, we then link observations into TNO orbits by constructing pairs and triplets of observations whose on-sky motion is consistent with an object on a Keplerian orbit in the Kuiper Belt, subject to Earth's parallax motion. To simplify the algorithm, we first remove the contribution from Earth parallax, and the resulting TNO trajectory is a straight line at roughly constant ecliptic latitude. Candidate orbits are fit using the code of Bernstein & Khushalani (2000), and kept if the per-degree-of-freedom $\chi^2 < 2$. The 341 TNOs DES has detected are outlined in Appendix B.

I finally detail the digital tracking method that can be used to expand DES's capabilities by shifting and stacking images along candidate trajectories such that the moving object remains stationary in the final coadded image. Stationary stars appear streaked, while the signal of a faint moving object is enhanced, allowing its detection. I explore how digital tracking could be applied to Neptune Trojans as a test case. Development on digital tracking will be continued by University of Michigan graduate student Larissa Markwardt.

CHAPTER III

Discovery and Physical Characterization of a Large Scattered Disk Object at 92 au

Published as: Gerdes, D. W., Sako, M., Hamilton, S., et al. 2017, ApJ, 839, L15.
My primary contributions are detailed in Section 3.6 and have been expanded upon for the purpose of this thesis.

3.1 Abstract

We report the observation and physical characterization of the possible dwarf planet 2014 UZ_{224} ("DeeDee"), a dynamically detached trans-Neptunian object discovered at 92 AU. This object is currently the second-most distant known trans-Neptunian object with secure orbital elements, surpassed in distance only by the dwarf planet Eris. Three additional objects are currently at larger distances (2018 VG_{18}, Sheppard et al. (2018); "FarFarOut," Sheppard & Trujillo, in press[1]; and V774104), but their observational arcs are too short to accurately determine their orbital elements. The object was discovered with an r-band magnitude of 23.0 in data collected by the Dark Energy Survey between 2014 and 2016. Its 1140-year orbit has $(a, e, i) = (109\ \mathrm{AU}, 20.54, 26.8°)$. It will reach its perihelion distance of 38 AU in

[1]https://www.sciencemag.org/news/2019/02/astronomers-discover-solar-system-s-most-distant-object-nicknamed-farfarout

the year 2142. Integrations of its orbit show it to be dynamically stable on Gyr timescales, with only weak interactions with Neptune. We have performed followup observations with ALMA, using 3 hours of on-source integration time to measure the object's thermal emission in the Rayleigh-Jeans tail. The signal is detected at 7σ significance, from which we determine a V-band albedo of $13.1^{+3.3}_{-2.4}(\mathrm{stat})^{+2.0}_{-1.4}(\mathrm{sys})$ percent and a diameter of $635^{+57}_{-61}(\mathrm{stat})^{+32}_{-39}(\mathrm{sys})$ km, assuming a spherical body with uniform surface properties.

3.2 Introduction

The scattered disk and inner Oort cloud populations of trans-Neptunian objects (TNOs) extend well beyond the classical Kuiper Belt, to distances of hundreds of AU. These dynamically disturbed populations must have arisen from very different mechanisms than those that produced the classical Kuiper Belt, as evidenced by marked differences in their sizes (Fraser et al., 2014), colors (Tegler & Romanishin, 2000), albedos (Brucker et al., 2009), and fraction of binaries (Noll et al., 2008). The scattered disk population has been further divided by Gladman et al. (2008) into objects which are actively scattering off Neptune (as indicated by a significant variation in their semi-major axis on 10 Myr timescales), and detached objects (non-scattering, non-resonant objects with $e > 0.24$). The half-dozen longest-period members of these populations display a statistically improbable clustering in argument of perihelion and longitude of ascending node. This finding has motivated the hypothesis of a distant super-earth (Trujillo & Sheppard, 2014; Batygin & Brown, 2016), sometimes called Planet 9. Deep, wide-area surveys capable of probing the distant scattered disk to high ecliptic latitudes have considerable potential to contribute to our knowledge of this region (Abbott et al., 2016b). In this Letter we report the discovery of a large scattered disk object at 92 AU using data from the Dark Energy Survey (DES; Flaugher 2005), with followup radiometric measurements by ALMA. Of known Solar

System objects with reported orbital elements, only the Pluto-sized dwarf planet Eris is currently more distant.

The DES is an optical survey of 5000 square degrees of the southern sky being carried out with the Dark Energy Camera (DECam, Flaugher et al. 2015) on the 4-meter Blanco telescope at Cerro Tololo Inter-American Observatory in Chile. DECam is a prime-focus camera with a 3 square degree field of view and a focal plane consisting of 62 2k×4k fully-depleted, red-sensitive CCDs. To achieve its primary scientific goal of constraining the dark energy equation of state, the DES has been awarded 525 nights over 5 years to carry out two interleaved surveys. The DES Supernova Program (DES-SN, Bernstein et al. 2012) images ten distinct DECam fields (a total of 30 sq. deg.) in the *griz* bands at approximately weekly intervals throughout the DES observing season, which runs from mid-August through mid-February. The Wide Survey covers the full survey footprint in the *grizY* bands to a limiting single-exposure depth of $m_r \sim 23.8$, with the goal of achieving 10 tilings per filter over the duration of the survey. The same combination of survey area and depth that makes DES a powerful tool for precision cosmology also makes it well suited to identify faint, distant objects in our own Solar System. With broad off-ecliptic coverage, it is especially well-suited to identifying members of the scattered disk and other high-inclination TNO populations such as detached and inner Oort cloud objects. We have previously reported on searches for TNOs in the DES-SN fields from the first two DES seasons, where discoveries have included two Neptune Trojans (Gerdes et al., 2016) and the "extreme TNO" 2013 RF_{98} (Abbott et al., 2016b) whose orbital alignment with other members of its class helped motivate the Planet 9 hypothesis. This paper presents our first result from the extension of the TNO search to the full DES Wide Survey, using data collected during the first three DES observing campaigns between August 2013 and February 2016.

3.3 Optical Data and Analysis

This analysis uses data from 14,857 exposures collected in the *griz* bands during the first 3 DES observing campaigns (Diehl et al., 2016). These exposures cover a 2500 square degree region north of DEC$= -40$, about half the full survey area. They contain over 1.1 billion individual object detections.

We identify transient objects using a variant of the DES supernova difference-imaging pipeline, `DiffImg` (Kessler et al., 2015). Each exposure (search image) is subtracted from every other DES exposure (template image) of that region taken in the same band. We do not use template images from the same night to avoid subtracting out the most distant and slowest moving objects, which may appear stationary over a period of several hours.

The difference images created from each search-template pair are then averaged, and statistically significant sources are identified in the combined image. Subtraction artifacts are rejected using a machine-learning technique described in Goldstein et al. (2015). This typically yields ~ 10 good-quality transient detections on each $9' \times 18'$ area covered by a single CCD.

After removal of stationary objects and artifacts with `DiffImg`, our search sample contains about 5 million single-epoch transients. While our selection efficiently retains true astrophysical transients—asteroids, variable stars, supernovae, etc.—the fraction of TNOs in this sample is on the order of only 0.1%.

The apparent motion of a distant Solar System object over periods of several weeks is primarily due not to its own orbital motion but to parallax arising from the motion of the Earth. Our TNO search procedure begins by identifying pairs of detections within 30 nights of each other whose separation is consistent with the seasonally-appropriate parallax expected for a distant object ($\lesssim 4''$/hour). We then attempt to link these pairs into chains of three or more observations, testing each chain for goodness of fit to an orbit using code built on the `fit_radec` algorithm of

Bernstein & Khushalani (2000) (B&K) and requiring $\chi^2/N < 2$.

2014 UZ_{224} was originally detected at a heliocentric distance of 92.5 AU in 7 linked observations on 4 nights between 2014/9/27 and 2014/10/28, with an r-band magnitude of 23.0 and an ecliptic latitude of $-10.3°$. The object was detected in 6 more DES survey images between 2014/8/19 and 2015/1/8, and was recovered in a targeted DECam observation on 2016/7/18. The motion of the object over the period of these observations is shown in Figure 3.1. The orbital elements are obtained using the B&K fitter. These and other data from these observations are shown in Table 3.1. We refer informally to this object as "DeeDee," for "distant dwarf."

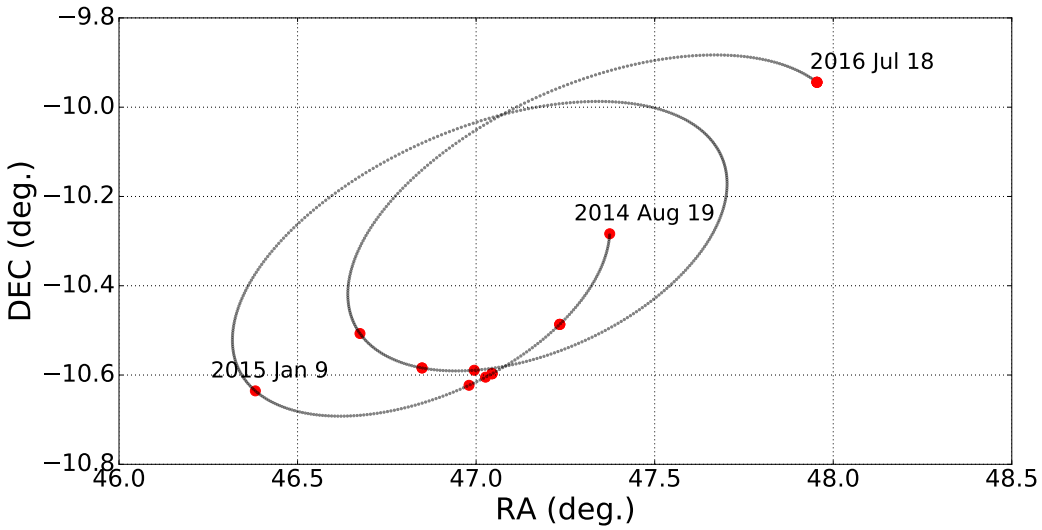

Figure 3.1: The path of 2014 UZ_{224} over the course of its observed 699-day arc. Dots indicate locations at which the object was observed by the DES.

Apparent and absolute magnitudes of Solar System objects are often standardized to Johnson-Cousins V-band magnitudes. We first derived transformation equations for stellar psf magnitudes to relate DES and SDSS magnitudes, then applied the transformations of Smith et al. (2002) to convert from the SDSS to Johnson-Cousins systems, obtaining $m_V = 23.38 \pm 0.05$. The transformation equations depend on the

Table 3.1. Orbital elements and other properties of 2014 UZ_{224}.

Parameter	Value
a (AU)	108.90 ± 7.36
e	0.651 ± 0.030
i (deg)	26.78509 ± 0.00012
ω (deg)	29.55 ± 1.46
Ω (deg)	131.142 ± 0.053
Perihelion (AU)	37.97 ± 0.69
Perihelion date	2142/01/02 $\pm$ 1654d
Aphelion (AU)	179.8 ± 12.1
Period (yr)	1136 ± 115
Epoch JD	2457600.5
Heliocentric distance at discovery (AU)	92.5
Arc length (days)	699
Apparent mag (r)	22.98 ± 0.04
Apparent mag (V)	23.38 ± 0.05
Absolute mag H_V	3.5
$g-r$ (mag.)	0.77 ± 0.11
$r-i$ (mag.)	0.39 ± 0.07
$i-z$ (mag.)	0.22 ± 0.16
Albedo (%)	$13.1^{+3.3}_{-2.4}(\text{stat})^{+2.0}_{-1.4}(\text{sys})$
Diameter (km)	$635^{+57}_{-61}(\text{stat})^{+32}_{-39}(\text{sys})$

$g-r$ color of the object in question, which is uncertain at the level of 0.11 mag. As a cross-check, the measured spectra of five TNOs with similar colors were flux-corrected and found to have a reasonable match to the observed DES magnitudes. From the flux-calibrated spectra of each of these TNOs, we applied a synthetic determination of the V-band magnitude. The central value and spread of these values is consistent with our measurement.

3.4 Orbital Dynamics

We next investigated the dynamical behavior of 2014 UZ_{224} on Gyr timescales. We generated 100,000 clones of 2014 UZ_{224} with respect to the best-fit orbit and its covariance matrix as described in Gladman et al. (2008). Taking the clone with the smallest RMS residual to be the new best-fit, we repeated the clone-generating procedure and identified the clones that yield residuals consistent with observations. Out of these objects, we chose the clones with minimum and maximum semi-major axes, as well as five additional clones interspersed between those two, and numer-

ically integrated the Solar System using all eight clones as test particles. We ran the integration for 1 Gyr using the hybrid symplectic and Bulirsch-Stoer integrator built into `Mercury6` (Chambers, 1999), and conserved energy to 1 part in 10^9. We did not include the terrestrial planets in our integrations, and we replaced Jupiter, Saturn, and Uranus with a solar J_2 (as done in Batygin & Brown, 2016). We included Neptune as an active body, because 2014 UZ_{224}'s perihelion distance of 38 AU brings it into proximity with Neptune.

As shown in Figure 3.2, over 1 Gyr timescales each clone remains confined to a region closely surrounding its measured orbit, with $\delta a/a$ being less than 1% for all clones. This result indicates that despite the potentially destabilizing interactions with Neptune, this object remains dynamically stable and satisfies the formal criteria of Gladman et al. (2008) as a detached TNO. Although the uncertainty on the object's semi-major axis overlaps with the 7:1 mean-motion resonance with Neptune, none of the clones we examined undergoes libration. We also performed several 4.5 Gyr integrations of the best-fit orbit. The object demonstrated stability over the full Solar System lifetime as well.

3.5 Measurement of Thermal Emission

We observed 2014 UZ_{224} with director's discretionary time on the Atacama Large Millimeter/submillimeter Array (ALMA) on 2016 August 19 and 20. The observations were carried out with 41 antennae and baselines between 15-1462 meters. The source was tracked using a user-provided ephemeris. The correlator was configured to observe four continuum spectral windows centered on 224, 226, 240, and 242 GHz, respectively, resulting in a total bandwidth of 7.5GHz. The nearby quasars J0522-3627 and J0238+1636 were used as bandpass calibrators for the first night and the second observations, respectively. The amplitude and phase of observations were calibrated by J0257-1212, and J0423-0120 was used for absolute flux calibration. The

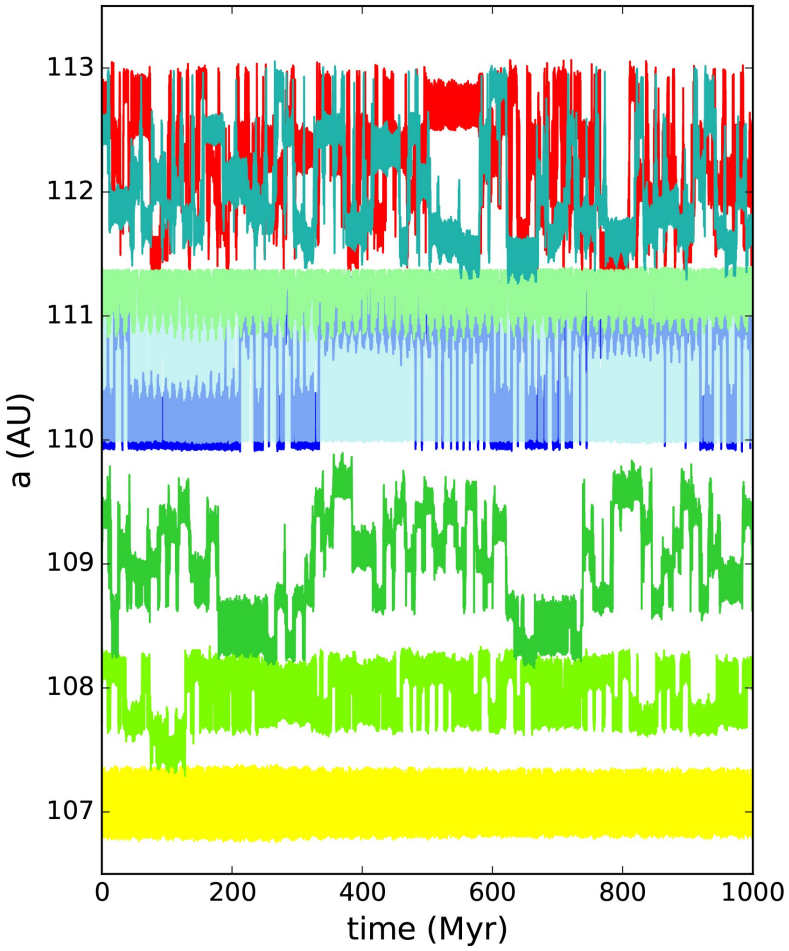

Figure 3.2: Time evolution of semi-major axis over 1 Gyr for each of the eight clones of 2014 UZ_{224} considered in this work, from the minimum (bottom line) to maximum (top) initial semi-major axis. For all clones, $\delta a/a$ is less than 1% in amplitude, demonstrating the long-term dynamical stability of this object in the presence of Neptune.

total on-source integration time was 176 minutes.

The raw data were calibrated by NRAO staff manually using the CASA package version 4.6. The calibrated visibilities of five data sets were then stacked to align the position using the `fixplanet` command. We generated a synthesized continuum image with the CLEAN algorithm and a natural weighting in CASA. The resulting synthesized beam is $0.30'' \times 0.25''$, with a position angle of $-84°$. A bright point-like source is detected at the center of the image, with a peak flux of 47 μJy/beam and a

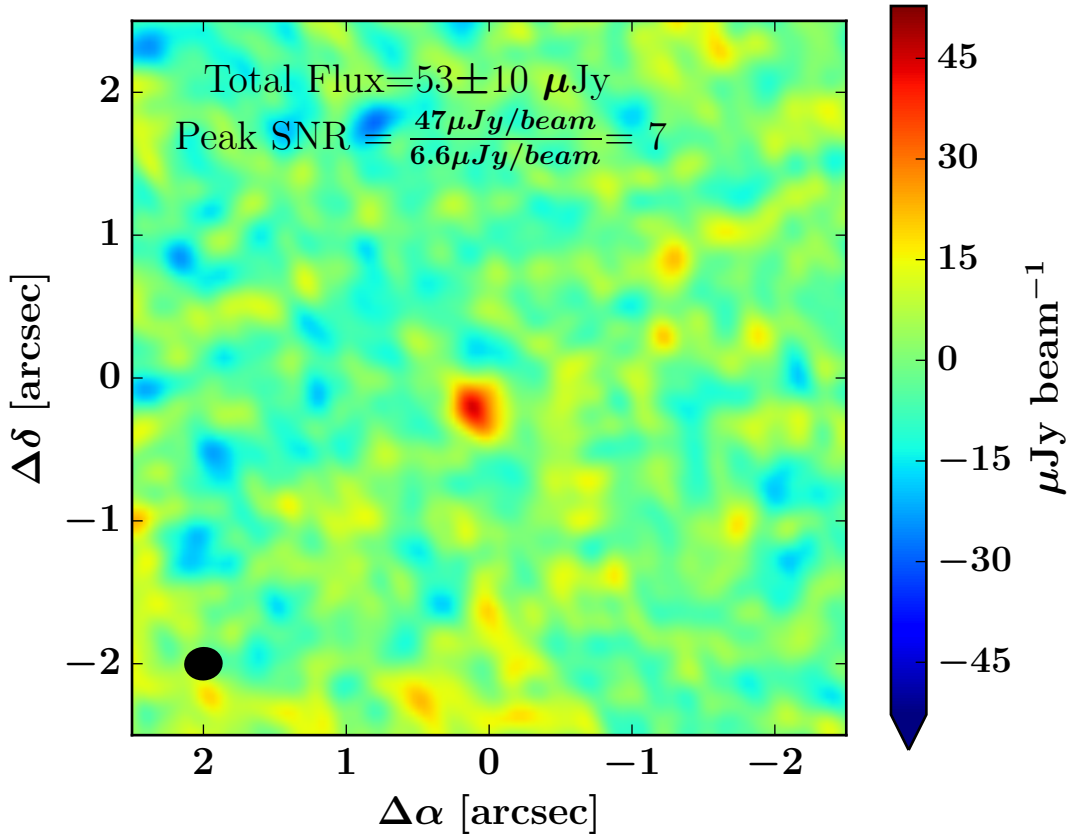

Figure 3.3: Calibrated, stacked image of 2014 UZ_{224} from 3 hours of on-source integration with ALMA. The black ellipse represents the size of the synthesized beam.

signal-to-noise ratio of ~ 7. We used the `imfit` task in CASA to fit the central source with a 2D Gaussian and found the source had a major-axis FWHM of $0.33 \pm 0.05''$ and a minor-axis FWHM of $0.25 \pm 0.03''$, with a position angle of $39''$. The apparent source size is thus consistent with the result of a point source convolved with the synthesized beam. The total flux measured from a 2D Gaussian fit is 53 ± 10 μJy. The final calibrated image is shown in Figure 3.3.

The source appears to be slightly elongated in the North-South direction compared to the synthesized beam. To test whether this apparent elongation was a result of a

binary system, we fit the source with two models: a single point source model and a binary model. The residuals after subtracting either model are very similar, and both were within 1σ of the distribution of noise measured in the background regions of the synthesized image. We conclude that the observations are consistent with a single point source.

3.6 Calculation of Size and Albedo

The absolute magnitude, H, of a Solar System minor body can be related to its diameter through the equation

$$D = \frac{1329\text{km}}{\sqrt{p}} 10^{-0.2H} \tag{3.1}$$

where p is the geometric albedo of the body. The factor of 1329 km ($= 2$ au $\cdot 10^{H_{\text{Sun}}/5}$) arises from the definition of H as the apparent magnitude of a solar system body if it were viewed at 0° phase angle from a distance of 1 au.

From Equation 3.1, we can calculate an object's size from its absolute magnitude only by assuming a value for its albedo. However, TNOs have been shown to show a wide variety of albedos (Lacerda et al. 2014; see also the TNO albedo, diameter, and density database in the NASA Planetary Data System[2], Johnston 2018), making estimating an albedo value for 2014 UZ_{224} difficult. By combining measurements at several different wavelengths spanning both sides of the Rayleigh-Jeans peak, such as using optical measurements (i.e. reflected solar flux or albedo) combined with thermal measurements (related to the object's size) one can determine both the albedo and size

[2]https://pds.nasa.gov

Table 3.2. Solar magnitudes and colors for the DES bandpass filters.

Band	λ_c (nm)	Solar Magnitude
u	355	-25.4296
g	473	-26.5079
r	642	-26.9601
i	784	-27.0499
z	926	-27.0567
Y	1009	-27.0619
$u-g$		1.0783
$g-r$		0.4522
$r-i$		0.0898
$i-z$		0.0068
$z-Y$		0.0052

without having to assume any values. Stansberry et al. (2008) provide the relations

$$F_V = \frac{F_{\odot,band}}{(r/AU)^2} R^2 p_V \frac{\Phi_{vis}}{\Delta^2} \tag{3.2}$$

$$F_\lambda = \frac{R^2 \Phi_{IR}}{\pi \Delta^2} \int \epsilon_\lambda B_\lambda(T(\theta,\phi)) \sin\theta d\Omega \tag{3.3}$$

where the parameters in the above equations are

- F_V – flux of 2014 UZ_{224} in the V-band.
- F_λ – flux of 2014 UZ_{224} at wavelength λ (here, 1.3mm)
- F_{vis} – measured flux density of object in a particular bandpass filter. Here I use the visual V-band.
- $F_{\odot,vis}$ – solar flux in same band. Table 3.2 shows the solar magnitudes in each DES filter, which can be converted to fluxes.
- r – heliocentric distance to the object in AU
- R – radius of the object in km

- p_V – geometric albedo of the object in the V-band, or the percentage of reflected light at zero phase angle of the spherical object (assumed to be diffusely reflecting) as compared to a flat disk of the same size.

- $\Phi(\alpha)$ – phase function in the wavelength regime being considered. The phase angle α is given by the law of cosines:

$$\alpha = \cos^{-1}\left(\frac{d_{BO}^2 + d_{BS}^2 - d_{OS}^2}{2 d_{BO} d_{BS}}\right) \tag{3.4}$$

  where d denotes the (B)ody-(O)bserver, (B)ody-(S)un, and (O)bserver-(S)un distances. The phase angle of 2014 UZ_{224} ranges from $\sim 0.3^\circ - 0.6^\circ$ over the three oppositions of observations, so I neglect the effects of changing phase angle and take both $\Phi_{vis}, \Phi_{IR} = 1$.

- Δ – geocentric distance of the object in AU

- ϵ – bolometric emissivity, taken to be 0.9 ± 0.1 as in Jewitt & Luu (1992), who inferred the value for outer Solar System objects using measurements of Pluto, Callisto, and Ganymede.

- ϵ_λ – the infrared emissivity, taken to be equal to 0.68 at 1.3mm wavelengths (Brown & Butler, 2017).

- $B_\lambda(T)$ – the Planck function, which describes the emission spectral density of a blackbody at temperature T. The functional form of $B_\lambda(T)$ is given in Equation 3.11 below.

- $T(\theta, \phi)$ – the temperature distribution on the surface of the object. θ, ϕ are the polar planetographic coordinates. The form of $T = T(\theta, \phi)$ depends on the surface geography, spin rate, bolometric emissivity (ϵ), thermal inertia, and shape of the object, none of which is generally known. Therefore it is common

practice to assume a simplified thermal model. The temperature distribution is then integrated over the visible hemisphere of the object and changes depending on the thermal model assumed for the object (see Section 3.6.1).

- $d\Omega$ – the solid angle subtended by the elements $d\theta$ and dϕ as seen from Earth

3.6.1 Overview of Thermal Models of Solar System Minor Bodies

In this section, I provide an overview of the models I considered during the course of this analysis.

3.6.1.1 Standard Thermal Model

The Standard Thermal Model (STM; Lebofsky & Spencer 1989, and references therein) describes a nonrotating body. Thus the temperature of the body depends only on the angular distance from the subsolar point:

$$T = T_0 \cos^{1/4}(\theta) \tag{3.5}$$

where $T_0 = \left(\frac{(1-p)S}{\eta\epsilon\sigma}\right)^{1/4}$ is the temperature at the subsolar point and $T = 0$ on the night side. Here $A = q_\alpha p_V$ is the bond albedo (and q_α is the phase integral), $S = \frac{1360 \text{ kW m}^{-2}}{(r/\text{AU})^2}$ is the solar constant at the object's distance, ϵ is the bolometric emissivity, σ is the Stefan-Boltzmann constant, and η is the "beaming factor." η was originally introduced to account for surface roughness and variations in thermal inertia but also serves to interpolate between the STM and its fast-rotator counterpart (described in Section 3.6.1.2) by scaling T_0. In the canonical STM, $\eta = 0.756$ (derived in Lebofsky et al. (1986) based on 10μm measurements of Ceres and Pallas). A pictorial representation of Equation 3.5 can be found on the left of Figure 3.4

Stansberry et al. (2008) assume a value of $q_\alpha = 0.8$ for large, bright KBOs because using the nominal $q_\alpha = 0.39$ results in unphysical geometric albedos. Thus they

use the value of Pluto, $q_\alpha = 0.8$, for the 4 largest TNOs. Note that low-albedo objects will be affected less than high-albedo objects by changes in q_α based on the $(1 - A) = (1 - q_\alpha p_V)$ term in T_0.

3.6.1.2 Isothermal Latitude Model

The Isothermal Latitude Model (ILM, Stansberry et al. 2008) describes a quickly rotating body. Thus the temperature of the body depends only on latitude:

$$T = T_0 \cos^{1/4}(\phi) \tag{3.6}$$

where $T_0 = \left(\frac{(1-A)S}{\pi\eta\epsilon\sigma}\right)^{1/4}$. The extra factor of π reduces the subsolar temperature by 33% as compared to the STM. The canonical ILM assumes $\eta = 1$. A pictorial representation of Equation 3.6 can be found on the right of Figure 3.4.

3.6.1.3 Hybrid Thermal Model

The Hybrid Thermal Model (Stansberry et al., 2008) resembles the STM and ILM, except now I set η to be a free parameter. The net effect of this action is to adjust for differences from the canonical models. In particular, $\eta < 1$ results in a higher temperature than predicted by the model while $\eta > 1$ results in a lower predicted temperature. For example, if using the hybrid STM results in $\eta = 1.09$ this simply means that the temperature distribution on the object is cooler than what is predicted from the canonical STM with $\eta = 0.756$ (that is, T_0 is cooler). Conversely, if using the hybrid ILM results in $\eta = 0.41$ this means that the surface temperature distribution is hotter than predicted by the canonical ILM with $\eta = 1.0$ (that is, T_0 is hotter) Physically relevant values are $0.6 < \eta < 2.6$, probed in Mommert et al. (2012) by using the Near Earth Asteroid Thermal Model (in which all solar phase angles are incorporated and η is allowed to vary) to model the two extremes: (1) a fast rotator

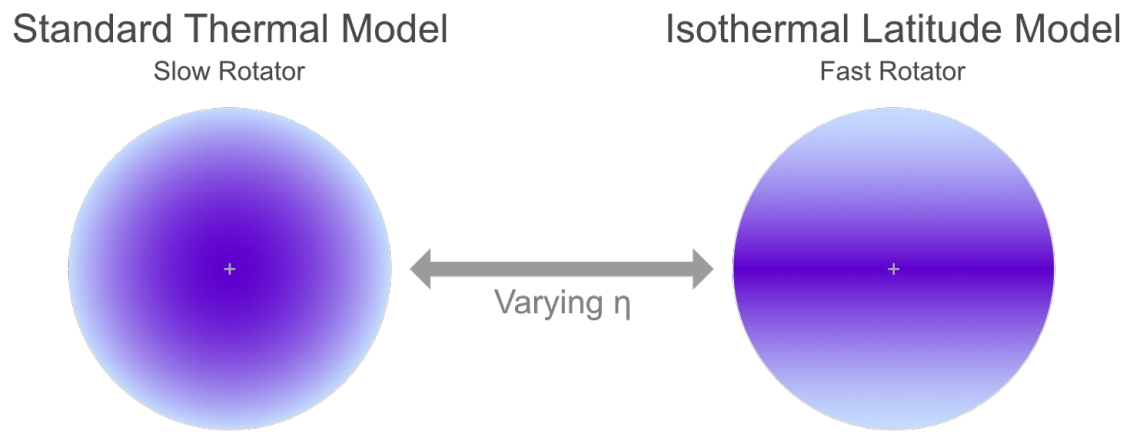

Figure 3.4: Depiction of the temperature distribution in both the STM and the ILM. The beaming parameter η, originally introduced to account for thermal inertia and surface roughness, also has the effect of interpolating between the two models. Hotter temperatures are indicated by darker purple, while the subsolar point is indicated by a "+" in both models.

with low surface roughness and high thermal inertia, which gives an upper bound on η, and (2) a slow rotator with high surface roughness and low thermal inertia, which gives a lower bound on η.

3.6.1.4 TNO-tuned STM

The TNO-tuned STM (Moullet et al., 2011) is the STM with $\eta = 1.25$, the average value found in Stansberry et al. (2008) using *Spitzer* observations. In Mommert et al. (2012), a value of $\eta = 1.20 \pm 0.35$ was derived from the *Spitzer* data presented in Stansberry et al. (2008). I did not use this model because I elected to allow η to explore its full range of physically allowed values.

3.6.2 Combining Measurement and Model to Calculate Size and Albedo

I now solve Equations 3.2 and 3.3 given the two measurements of 2014 UZ_{224} in the V-band using DES and at 1.3mm wavelength using ALMA. This will uniquely determine both the object's size and albedo. I used the several measurements in *griz*

to obtain a V-band magnitude of 23.45 ± 0.05.[3] I rearrange and simplify Equations 3.2 and 3.3 to the following forms:

$$F_V = F_{\odot,V} \frac{p_V}{4} \left(\frac{D}{\Delta}\right)^2 \left(\frac{r}{1\text{ au}}\right)^{-2}, \tag{3.7}$$

$$F_\lambda = \int \epsilon_\lambda B_\lambda(T(\theta,\phi)) d\Omega \tag{3.8}$$

The STM (Section 3.6.1.1) describes a spherical, non-rotating body observed at 0° phase angle and represents the hottest possible temperature distribution. Conversely, the ILM describes a quickly rotating body observed at 0° phase angle and represents the coolest possible temperature distribution. I adopt the Hybrid STM in order to interpolate between the two models.

Obtaining several measurements spanning both sides of the peak of the blackbody emission spectrum would allow us to leave η as a free parameter to fit in the model, significantly constraining the temperature distribution on the surface. However, this is not possible with a single-wavelength measurement, and I must allow η to explore its full range of 0.6 to 2.6 (Mommert et al., 2012). For the remainder of this work I use the Hybrid STM (Section 3.6.1.3) as the base model. Equation 3.8 then becomes:

$$F_\lambda = \frac{\epsilon_\lambda D^2}{2\Delta^2} \int_0^{\pi/2} B_\lambda(T(\theta)) \sin\theta \cos\theta d\theta. \tag{3.9}$$

Adopting the Hybrid STM requires that some assumptions be made regarding the nature of the object's thermal emissions. First, I assume a bolometric emissivity $\epsilon = 0.9 \pm 0.1$, a typical assumption for TNO thermal models. I note, however, that the practice of assuming this value for all wavelengths is only valid for wavelengths $\lesssim 350\mu$m. Brown & Butler (2017) show that for longer wavelengths an emissivity suppression is observed. I adopt a value of $\epsilon_\lambda = 0.68$ at 1.3mm, the average for the

[3] Calculation performed by William Wester (Fermilab)

four objects considered in Brown & Butler (2017) with ALMA's 233 GHz band. I keep $\epsilon = 0.9 \pm 0.1$ as the bolometric emissivity in the surface temperature distribution. The second assumption sets the phase integral $q_\alpha = 0.8$ as derived in Stansberry et al. (2008) for large, bright TNOs, noting that varying q_α from 0.4 to 0.8 results in $< 1\%$ variation in albedo for low-albedo TNOs. The phase angle for an object at ∼92 AU never exceeds 1°, so I neglect any effects arising from a changing phase angle and set the phase angle equal to zero.

Equation 3.8 becomes

$$F_\lambda = \frac{\epsilon_\lambda D^2}{2\Delta^2} \int_0^{\pi/2} B_\lambda(T(q_\alpha p_V, \theta)) \sin\theta \cos\theta d\theta \tag{3.10}$$

where

$$B_\lambda(T(q_\alpha p_V, \theta)) = \frac{2\pi hc^2}{\lambda^5} \frac{1}{e^{hc/\lambda kT} - 1} \tag{3.11}$$

and

$$T(q_\alpha p_V, \theta) = \begin{cases} \left(\frac{(1-q_\alpha p_V) S_\odot}{\eta \epsilon \sigma r^2}\right)^{1/4} \cos^{1/4}\theta, & \theta \leq \frac{\pi}{2} \\ 0, & \text{else} \end{cases} \tag{3.12}$$

I first solved Equations 3.2 and 3.10 for D^2, which gives

$$D^2 = \frac{F_V}{F_{\odot,V}} \frac{4 r_V^2 \Delta_V^2}{p_V} \tag{3.13}$$

$$D^2 = \frac{2 F_\lambda \Delta_\lambda^2}{\epsilon_\lambda} \frac{1}{\int_0^{\pi/2} B_\lambda(T(q_\alpha p_V, \theta)) \sin\theta \cos\theta d\theta} \tag{3.14}$$

When set equal to each other, this gives

$$\frac{\int_0^{\pi/2} B_\lambda(p_V,\theta)\sin\theta\cos\theta d\theta}{p_V} = F_\lambda \frac{F_{\odot,V}}{F_\nu}\frac{\Delta_\lambda^2}{\Delta_V^2}\frac{1}{2\epsilon_\lambda r^2} \tag{3.15}$$

$$= F_\lambda \cdot 10^{-(m_\odot - m_v)/2.5} \cdot \frac{\Delta_\lambda^2}{\Delta_V^2}\frac{1}{2\epsilon_\lambda r^2} \tag{3.16}$$

Equation 3.16 was coded into Mathematica and solved numerically for p_V, whose value was then used in Equation 3.13 to solve for D.

3.6.3 Measurement Uncertainty Analysis

Estimation of the uncertainties in the calculated diameter and albedo were performed following the procedure outlined in Mommert et al. (2012). I employed a Monte Carlo simulation using 5000 clones, where each clone was generated by varying the observed flux densities at both the thermal and optical wavelengths, the heliocentric and geocentric distances associated with the optical measurements, the bolometric emissivity ϵ, and the beaming factor η. The uncertainties are dominated by the statistical uncertainty in the flux measurements. Each parameter, with the exception of η, was varied randomly according to a normal distribution defined by its nominal value and 1σ uncertainty. η was varied according to a uniform distribution from 0.6 to 2.6. The uncertainties in the diameter and albedo were then defined by the lower and upper values that included 68.2% of the clones, centered on the peaks of the resulting distributions of the two parameters. A summary of the parameters and associated uncertainties used in this analysis can be seen in Table 3.3.

Under the assumptions of the preceding sections and using the values summarized in Table 3.3 I measure the geometric albedo and diameter of 2014 UZ_{224} to be

$$\begin{aligned} p_V &= 13.1^{+3.3}_{-2.4}(\text{stat})^{+2.0}_{-1.4}(\text{sys})\% \\ D &= 635^{+57}_{-61}(\text{stat})^{+32}_{-39}(\text{sys})\ \text{km}. \end{aligned}$$

Table 3.3. Parameter values and uncertainties used to calculate the diameter and albedo of 2014 UZ_{224}.

Parameter	Value	Comment
F_λ	53 ± 10 Jy	Flux at 1.3mm
m_V	23.45 ± 0.05	2014 UZ_{224} V-band magnitude
$m_{\odot,V}$	-26.76 ± 0.02	Solar V-band magnitude
Δ_V	91.665 ± 0.277 AU	2014 UZ_{224}-Earth distance, visual
r	92.272 ± 0.282 AU	2014 UZ_{224}-Sun distance, visual
ϵ	0.9 ± 0.1	Bolometric emissivity
ϵ_λ	0.68	Approximate spectral emissivity at 1.3mm
η	$0.6 < \eta < 2.6$	Beaming factor

Here the quoted statistical uncertainty is due to the uncertainties in both the visual and thermal flux measurements, as well as uncertainties in the helio- and geo-centric distance measurements. The quoted systematic uncertainty is due to variation of the model parameters η and ϵ.

As shown in Fig. 3.5, the measured albedo is higher than that of rocky bodies such as asteroids, and of typical classical KBOs, yet notably smaller than ice-rich dwarf planets Eris (96%, Sicardy et al. 2011), Haumea (80%, Fornasier et al. 2013), Pluto (72%, Buratti et al. 2017) and Sedna (32%, Pál et al. 2012), suggesting that 2014 UZ_{224} has a mixed ice-rock composition. An object of this composition and size is likely to have enough self-gravity to reach an approximately spherical shape in hydrostatic equilibrium (Tancredi & Favre, 2008), making 2014 UZ_{224} a candidate dwarf planet.

3.7 Conclusions

We have reported the discovery of 2014 UZ_{224} ("DeeDee") a trans-Neptunian object discovered at 92 AU from the Sun. This object has an estimated size $D \approx 640$ km and albedo $p_V \approx 13\%$, and is most likely a dwarf planet with a mixed ice-rock composition. This discovery adds to the growing inventory of dwarf planets in

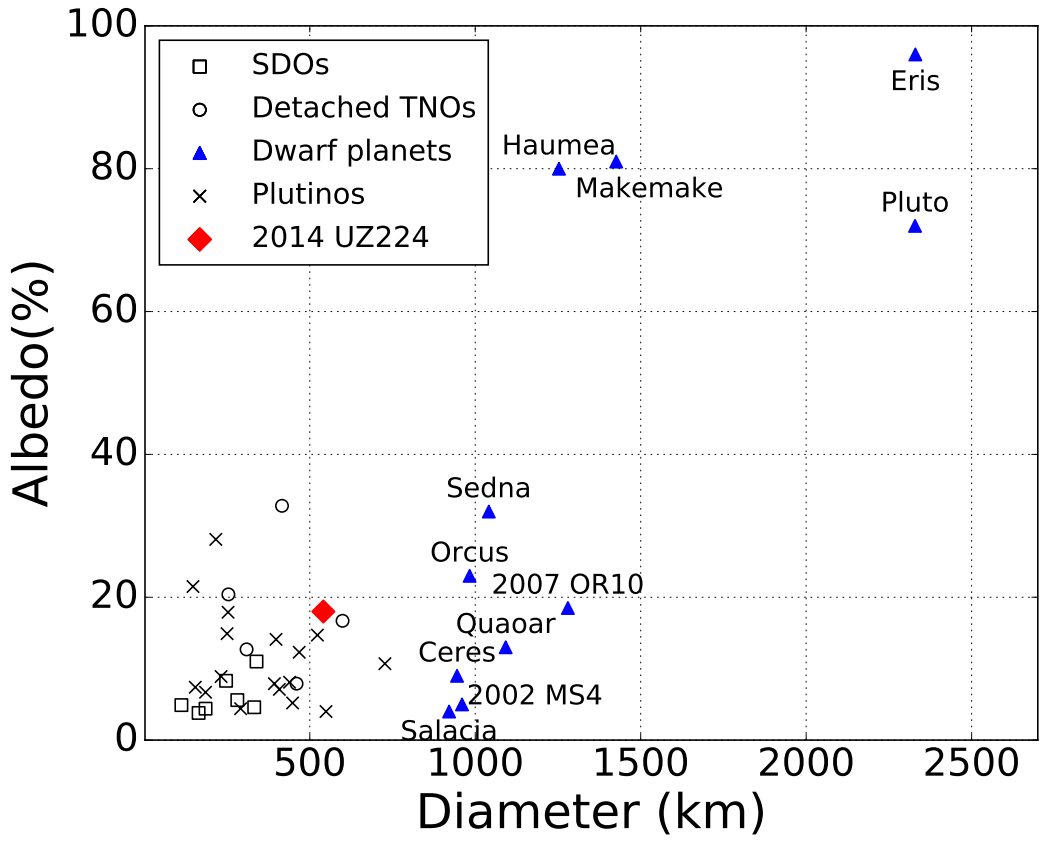

Figure 3.5: Size-albedo relations for selected TNO populations including detached and scattered disk objects (Li et al., 2006; Santos-Sanz et al., 2012), Plutinos (Mommert et al., 2012), and dwarf planets (Sicardy et al., 2011; Fornasier et al., 2013; Pál et al., 2012; Buratti et al., 2017). The object 2014 UZ_{224} is shown as a filled diamond.

the outer Solar System, and indicates that the TNO population displays a nearly continuous distribution of size and albedo.

Neither the orbital nor the physical properties of 2014 UZ_{224} are surprising, as they are in the range of other well-characterized detached TNOs discovered closer to the Sun. The population of detected TNOs is of course strongly biased toward those that are large, near perihelion, and/or have high albedo. Current surveys such as the DES now have the depth and area coverage to discover the counterparts of known objects that are well beyond perihelion. It is also noteworthy that the ALMA facility is easily capable of radiometric detection of a 600 km body at > 90 AU distance. Hence it will be possible to establish sizes and albedos for nearly every body detectable in the visible by DES and similar surveys. As these surveys progress, we will be able for example to determine whether the very high albedo of Eris is characteristic of large bodies at this distance, or whether flux selection has led to the first discovery being atypical.

CHAPTER IV

Constructing a Survey Simulator for Moving Object Analysis in the Dark Energy Survey

This Chapter through Section 4.4 comprises the majority of a **paper to be published as:** Hamilton, S. J., Napier, K. J., Gerdes, D. W., et al. 2019, in prep.

Further, Section 4.4 details the uses of the DES survey simulator thus far and summarize my contributions to the three papers in subsections 4.4.1–4.4.3.

4.1 Abstract

Models of Neptune's migration through the outer Solar System during its formation can be constrained through careful measurements of the orbits of planetesimals in this region. However, determining the true underlying orbital distributions of Kuiper Belt objects from the observed populations is highly nontrivial due to complicated biases introduced by the strategies of a survey. An increasingly popular approach to disentangling survey biases from the inferred distributions of detected Kuiper Belt Objects is through the use of a "survey simulator." This paper presents the design of the Dark Energy Survey Simulator and demonstrates how the strategy of the Dark Energy Survey sculpts the orbital distributions of detected Kuiper Belt Objects. I apply my survey simulator in Chapter V to the most distant Trans-Neptunian Objects

(TNOs) in the solar system, the objects known as "extreme" TNOs whose orbital clustering has been used to argue for a new planet in the distant solar system. I find that the null hypothesis in which the extreme TNOs originate from an underlying uniform distribution in orbital angles is not rejectable.

4.2 Introduction

To date, more than 2000 trans-Neptunian objects (TNOs) have been discovered, accumulated from successful searches spanning only three decades. These searches have been motivated by the recognition that studying the characteristics and orbits of objects in a remnant debris disk such as the Kuiper Belt would provide insight into the Solar System's formation and dynamical processes that have resulted in what we observe today.

To rigorously test hypotheses of the Solar System's evolution and subsequent imprints upon the distributions of minor bodies in the Solar System, the observational biases of a survey that may skew perception of the true underlying populations of the Kuiper Belt must be well-understood. Such biases include *flux bias*, where the brightest objects are discovered preferentially; *pointing bias*, where only the populations with members in the location of survey pointings will be discovered; *ephemeris bias*, where assumptions about an object's orbit are made using a short preliminary discovery arc, consequently leading to a loss in objects if that assumption is incorrect; and *detection bias*, where the temporal separation of successive images of a region of sky influences the distance at which objects can be discovered. (Kavelaars et al., 2008). The existence of observational biases in detected samples of TNOs is a well-known problem, and there have been many attempts since the discovery of the Kuiper Belt to account for such biases. These include the Monte Carlo approaches of Jewitt & Luu (1995) and Schwamb et al. (2009), the Bayesian methods employed by Gladman et al. (1998) and Parker (2015), and even a pseudo-survey simulator

approach by Hahn & Malhotra (2005).

The analytic debiasing approaches are no longer sufficient for the level of detail required to distinguish between different Neptune migration scenarios using the growing inventory of TNOs. To overcome shortcomings of those approaches and disentangle the observed orbital distributions from observational biases, the "survey simulator" debiasing approach has gained popularity. In this approach, models of the intrinsic Kuiper Belt distributions are made subject to the same biases as real Kuiper Belt populations, and the simulated distributions detected by the survey can then be compared to real observations. This approach provides a statistically robust comparison between the synthetic and real observations from a given survey, allowing us to evaluate whether a synthetic population model is statistically consistent with the observed population. Thus, the survey simulator approach is one of model rejection rather than model fitting.

A survey simulator requires that a survey maintain precise knowledge of the telescope pointings, limiting magnitudes by exposure, and efficiency of detection with respect to apparent motion. With this information, one can generate any desired synthetic population of objects, project their positions into survey exposures, and determine whether or not the objects could have been detected. Without knowledge of the discovery circumstances of an object, it is difficult to draw quantitative conclusions about the underlying orbital distributions in the outer Solar System using that object. The survey simulator approach to debiasing TNO surveys has been effectively demonstrated by the Canada-France Ecliptic Plane Survey (CFEPS, Jones et al. 2006; Petit et al. 2011) and the Outer Solar System Origins Survey (OSSOS, Bannister et al. 2016; Lawler et al. 2018a).

4.3 Characterizing the Dark Energy Survey

DES is one of the first deep, large-area, high-inclination surveys being used for Solar System science. DES discoveries, especially those pertaining to the lesser-studied high-inclination Solar System, will prove fruitful for refining models of the structure of the Kuiper Belt. To perform that science, we must characterize DES and carefully quantify its biases toward detecting objects with particular orbital properties. I present my efforts here. My approach differs from that of the OSSOS Survey Simulator primarily due to the fact that the DES design does not allow for the detection of tracklets prior to constructing orbits. Thus, there is no need to be able to resolve such a tracklet and therefore there is no lower limit on the rate of on-sky motion of a solar system object observed by DES.

4.3.1 Determination of Limiting Magnitudes

In order to calculate single-exposure detection efficiencies and limiting magnitudes, I use the ability of `DiffImg` to implant fake sources of a specified magnitude at the pixel level in raw source images. `DiffImg` implants (4 sources per CCD) $\times$ (60 CCDs) $= 240$ stationary fake objects of fixed magnitude $m_x = 20$, where x is the band being considered in $griz$. These so-called mag20 fakes are nominally used to evaluate data quality, where an average signal-to-noise ratio (SNR) < 20 (or < 80 in the deep SN fields) of the 240 fakes flags an exposure to be retaken (Kessler et al., 2015). `DiffImg` can also be configured to implant **either** stationary SN fakes of varying magnitudes **or** moving TNO fakes of varying magnitudes. In a nominal SN `DiffImg` run, images are processed with both the so-called mag20 fakes and the SN fakes implanted. The fake SNe have known, differing magnitudes spanning below and above the single exposure 50% detection threshold and are embedded in every SN field image processed through `DiffImg`. Thus, I can accurately obtain 50% limiting magnitudes for every SN exposure using the fake SNe and usual techniques. Unfortunately, fake TNOs are

not embedded at a sufficiently high density in `wsdiff` exposures to enable limiting magnitude calculations via the same technique in these images.

To overcome this problem, I instead use the mag20 fakes, which are implanted in every `DiffImg` exposure regardless of whether SN or TNO fakes are implanted. At four per CCD, the number density of the mag20 fakes is sufficiently high, so I use the measured SNR of the mag20 fakes to empirically calculate the limiting magnitude of each `wsdiff` exposure.

I begin by constructing a second-order polynomial fit to the measured SNR of the mag20 fakes vs. limiting magnitude calculated via implanted SN fakes for every `DiffImg`-processed SN image of the form:

$$m_{\rm lim} = ax^2 + bx + c, \tag{4.1}$$

where $x = \log_{10}(\mathrm{SNR}_{\rm mag20})$. Then, using the polynomial fit and the measured SNR of the mag20 fakes in every `wsdiff` exposure, I calculate the limiting magnitude of that exposure. The results of the fit are shown in Figure 4.1 and summarized in Table 4.1a.

Because the limiting magnitudes of the SN fields are a product of the DES-SN pipeline, I use those values as given (Kessler et al., 2015). The limiting magnitudes of Wide Survey exposures that have been processed through `DiffImg` (and therefore have had mag20 fakes embedded) are calculated via the procedure outlined above. However, for the remaining Wide Survey exposures, I take a different approach because those exposures do not have associated mag20 fakes. To circumvent this problem, I turn to other measures of data quality. I use the effective exposure time multiplier, $t_{\rm eff}$, defined as

$$t_{\rm eff} = \eta^2 \left(\frac{\mathrm{FWHM}}{0.9\text{”}}\right)^{-2} \left(\frac{b}{b_{dark}}\right)^{-1} \tag{4.2}$$

where η is the atmospheric transmission, b is the sky brightness, and b_{dark} represents

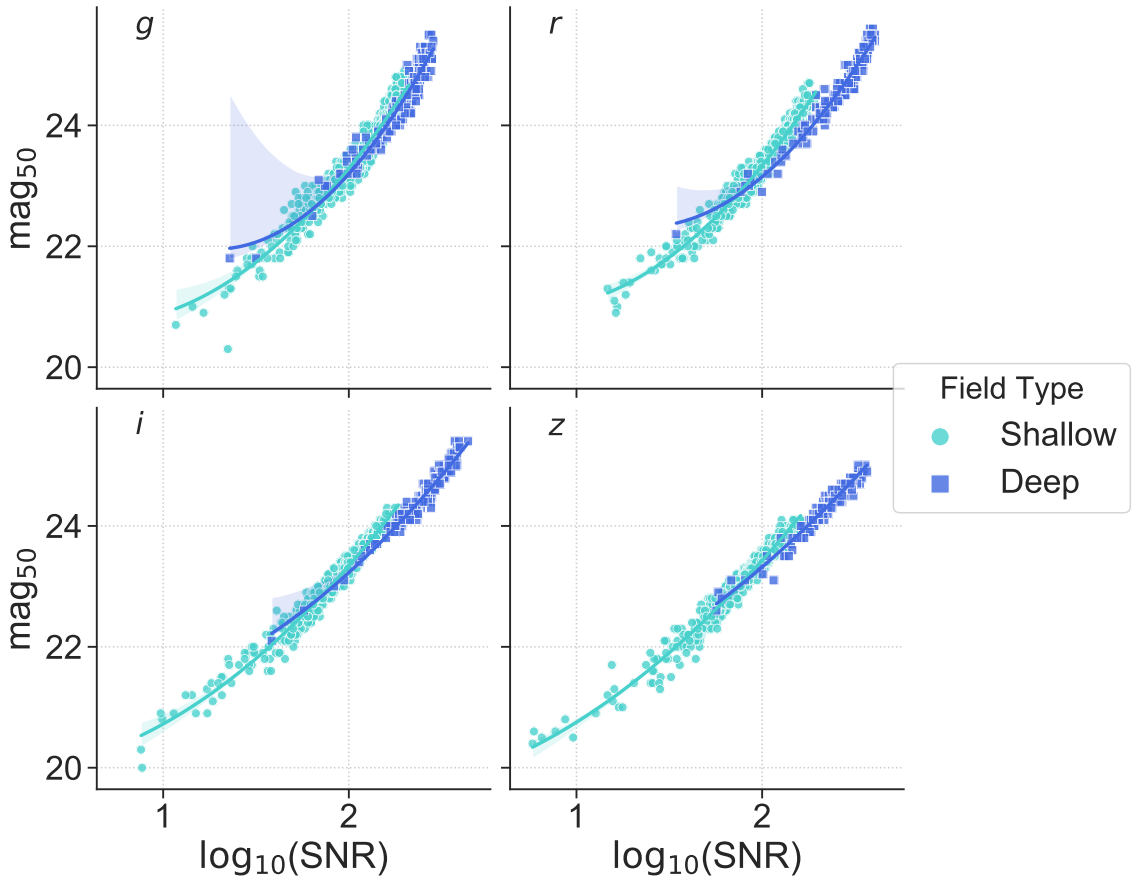

Figure 4.1: Demonstration of the fit to the SNR of the implanted mag20 fakes to the 50% limiting magnitude per exposure, mag_{50}, using Equation 4.1. The teal points represent the fit to the shallow SN fields, while the blue squares represent the fit to the deep SN fields. Fit values are presented in Table 4.2a.

the sky brightness of a dark sky at zenith and varies by filter (H. Neilsen et al., 2016). Because the value of $t_{\rm eff}$ is a standard product of nominal DES data processing, all DES exposures have a measured $t_{\rm eff}$, and the 50% limiting magnitude is a sensitive function of this value. To estimate the limiting magnitude of the non-`wsdiff` exposures, I perform a linear fit to the measured $t_{\rm eff}$ and the known 50% limiting magnitude of the SN exposures:

$$m_{\rm lim} = dy + f \tag{4.3}$$

where $y = \log_{10}(t_{\rm eff})$. The results of this fit are shown in Figure 4.2 and summarized in Table 4.1b. It is important to note that the non-`wsdiff` limiting magnitudes are used solely to study the effects of bias of our full survey on various Solar System populations. When comparing the real detections to model predictions using the survey simulator, I consider only the `wsdiff` exposures and limiting magnitudes.

4.3.2 Survey Simulator Design

The irregular temporal cadence employed by DES to accomplish its cosmological goals introduces significant challenges that need to be overcome in both the detection of real objects and the simulation of synthetic objects in the survey. Perhaps most significantly, it is not generally possible to employ the commonly-used tracklet detection technique employed by other dedicated TNO surveys, where exposures are taken of the same region of sky once every 20 minutes to an hour depending on the target of the survey. Only in the deep supernova fields of the DES-SN program, where 5-11 exposures of the same field are taken consecutively in the same band, is this technique feasible. However, the deep supernova fields comprise such a small percentage of both the current and anticipated final data set that it is not reasonable to employ the tracklet discovery technique in our search.

Additionally, the bulk of the survey area is comprised of the Wide Survey. The DES TNO search specifically uses the 90s exposures taken in the *griz* bandpass

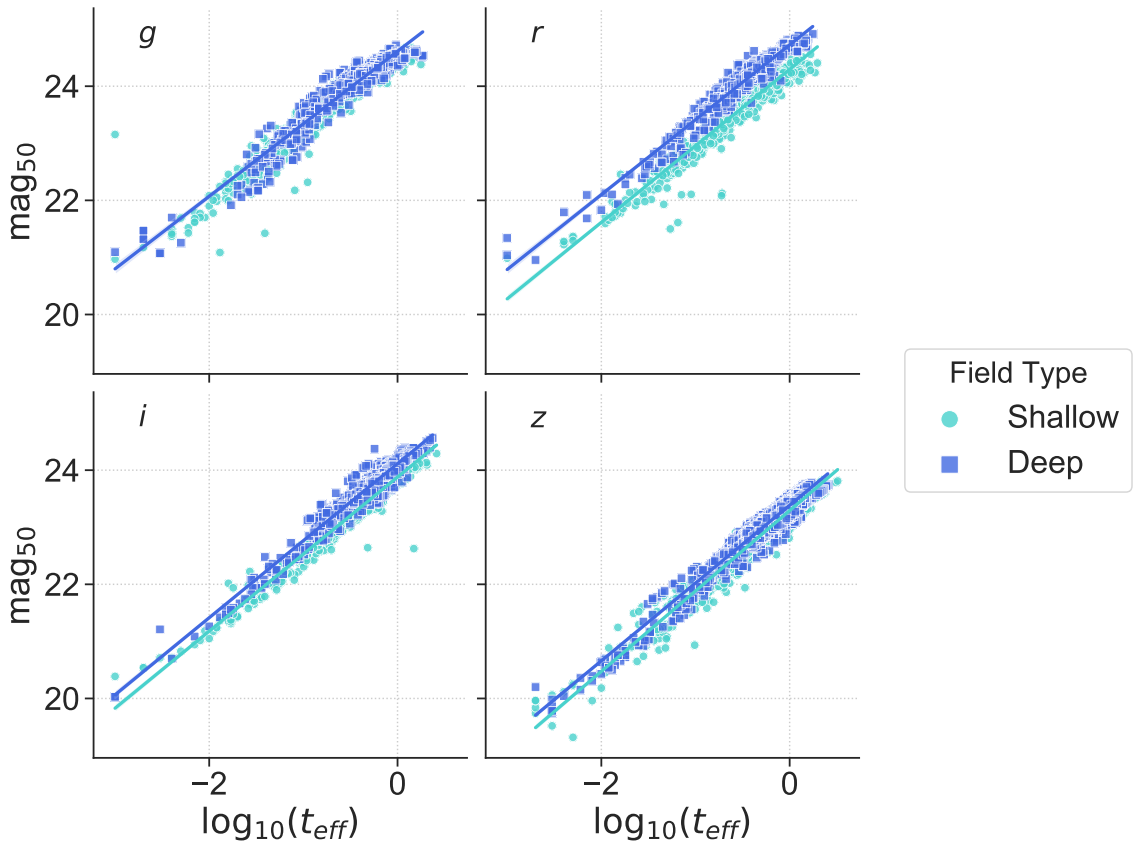

Figure 4.2: Demonstration of the fit to the t_{eff} of exposures with implanted mag20 fakes to the 50% limiting magnitude per exposure, mag_{50}, using Equation 4.3. Colors are as in Figure 4.1. Fit values are presented in Table 4.2b.

Table 4.1: Fit parameters for calculating the limiting magnitude of DES exposures

a) Limiting magnitude fit for `wsdiff` exposures[a]

Field	**Band**	**Fit Values**		
		a	b	c
Shallow	g	1.41	-1.84	21.3
	r	1.51	-2.27	21.8
	i	0.91	-0.10	19.9
	z	0.75	0.42	19.6
Deep	g	2.39	-6.11	25.9
	r	2.00	-5.42	26.0
	i	0.87	-0.69	21.1
	z	0.63	0.10	20.6

[a] Second-order polynomial fit as in Equation 4.1

b) Limiting magnitude fit for non-`wsdiff` exposures[b]

Field	**Band**	**Fit Values**	
		d	f
Shallow	g	0.55	24.6
	r	0.57	24.7
	i	0.59	24.1
	z	0.59	23.4
Deep	g	0.55	24.6
	r	0.58	24.3
	i	0.59	23.9
	z	0.61	23.3

[b] Linear fit as in Equation 4.3

filters. A TNO moving with a rate of $\sim 5''$ per hour (typical of Neptune Trojans near opposition) will only move $\sim 0.1''$ during the exposure, which is far less than the typical point-spread function for a DES exposure ($\sim 0.87''$ in the z band up to $\sim 1''$ in the g band; Morganson et al. 2018). The longest DES exposures are the 360 second i-band exposures in the deep DES-SN program. Even here, a TNO moving at ~ 5" per hour will only move $\sim 0.5''$ during the course of the exposure, still less than the point-spread function. Thus, I need not worry about simulating trailing losses.

I begin by calculating the limiting magnitudes of each exposure in the data set using the method outlined in Section 4.3.1. I note that this step need only be repeated if the dataset is adjusted in some way, e.g. if additional exposures are processed through `DiffImg`, for example. My simulator can then be operated in two modes: 1) generate a specified number of synthetic objects or 2) take an input file containing the orbital elements of previously-generated objects, e.g. the CFEPS L7 model (Kavelaars et al., 2009; Petit et al., 2011). When generating new synthetic objects, the user may specify the parameters of the orbital element distributions they wish to use. For each synthetic object, I then determine the exposures located within 7° of the position of the object on August 15, 2016 (the approximate midpoint of the survey). I choose a radius of 7° because even the fastest-moving TNOs (Neptune Trojans) do not exceed a maximum on-sky separation of 7°from their positions on August 15, 2016 during DES operations. Finally, I project the position of each object into each of these nearby exposures and determine whether the object fell on a CCD during that exposure using the known telescope pointing and the geometry of DECam. To determine whether an object was linked, I then use a parameterization of the moving object search pipeline, which quantifies the linking efficiency as a function of the number of detections of a specific object. I fit a hyperbolic tangent efficiency function to the data of the form

$$\eta(N) = 0.5A \ \tanh\left(\frac{N - N_{50}}{W}\right), \tag{4.4}$$

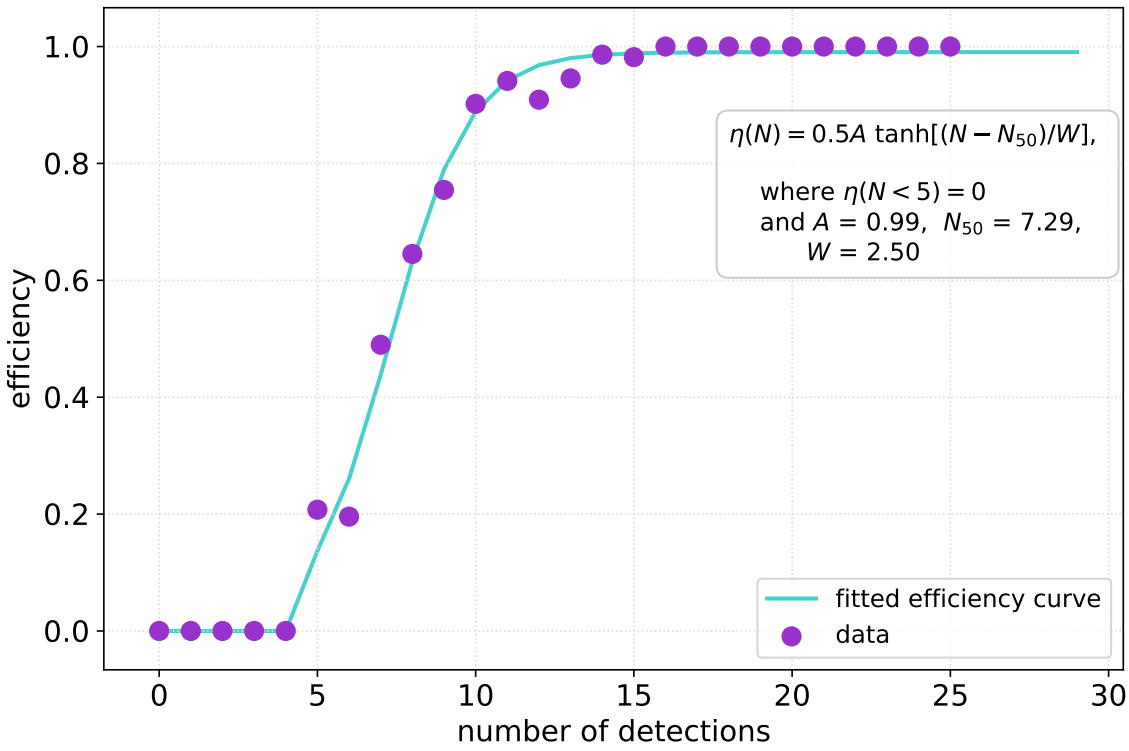

Figure 4.3: The efficiency of linking individual observations into objects vs. the number of observations of an object, calculated using fake sources implanted in the `DiffImg` data. Because the linker forms candidate objects by connecting triplets of observations to pairs, it cannot detect an object with fewer than five observations.

where N is the number of detections and $A = 0.99$, $N_{50} = 7.29$, and $W = 2.50$, noting that $\eta(N < 5) = 0$. These data are presented in Figure 4.3.

4.4 Applications of the Survey Simulator

The following sections describe the analyses for which the survey simulator has been used thus far.

4.4.1 Analysis of a New Highly-Inclined Extreme TNO

The extreme TNOs, described in more detail in Chapter V, are those objects for which $a > 230$ au and $q > 30$ au. Trujillo & Sheppard (2014) first noted an apparent

clustering in the argument of perihelion, ω, of these long-period objects. Batygin & Brown (2016) have further noted the apparent clustering in longitude of perihelion ($\varpi = \omega + \Omega$) of these objects and suggested the existence of an as-yet-undiscovered massive planet in the distant Solar System. In Becker et al. (2018), we report the discovery of a new high-inclination ETNO, 2015 BP_{519}, with $a = 450$ au, $e = 0.92$, and $i = 54.1°$. 2015 BP_{519} further has $\omega = 348.1°$ and $\Omega = 135.2°$. 2015 BP_{519} has the highest inclination of all known ETNOs as of this writing.

Because DES observes primarily at high ecliptic latitudes, it is natural to ask whether 2015 BP_{519}'s high inclination can be at least partially attributed to observational bias. I use the survey simulator to evaluate potential effects of this bias. I generate clones of 2015 BP_{519} with identical values for the orbital elements as above, but allow i to vary uniformly from 0° to 180°. Figure 4.4 shows the results of this simulation. The sensitivity distribution shows some structure but is not zero anywhere, and it is not heavily biased toward the observed value of inclination for 2015 BP_{519}.

2015 BP_{519} also appears to be clustered in ϖ with the other ETNOs. I ran a second simulation to evaluate potential effects of bias on the observed values of ω, Ω, and consequently ϖ for 2015 BP_{519}. The procedure is similar to the described inclination study, except I instead leave a, e, and i as their observed values and allow ω and Ω to vary uniformly from 0° to 360°. Figure 4.5 shows the results of this simulation. The sensitivity functions again show some structure, but DES is not heavily biased toward 2015 BP_{519}'s observed values of these parameters.

4.4.2 Analysis of Three Closely-Associated Distant Objects

In Khain et al. (2018), we report the discovery of two new distant TNOs with similar orbital elements. 2016 QU_{89} and 2016 QV_{89} have values of (a, e, i) of (171.4 au, 0.79, 17.0°) and (171.7 au, 0.77, 21.4°), respectively. Furthermore, de la Fuente Marcos et al. (2017) previously reported the discovery of the TNO 2013 UH_{15}, which

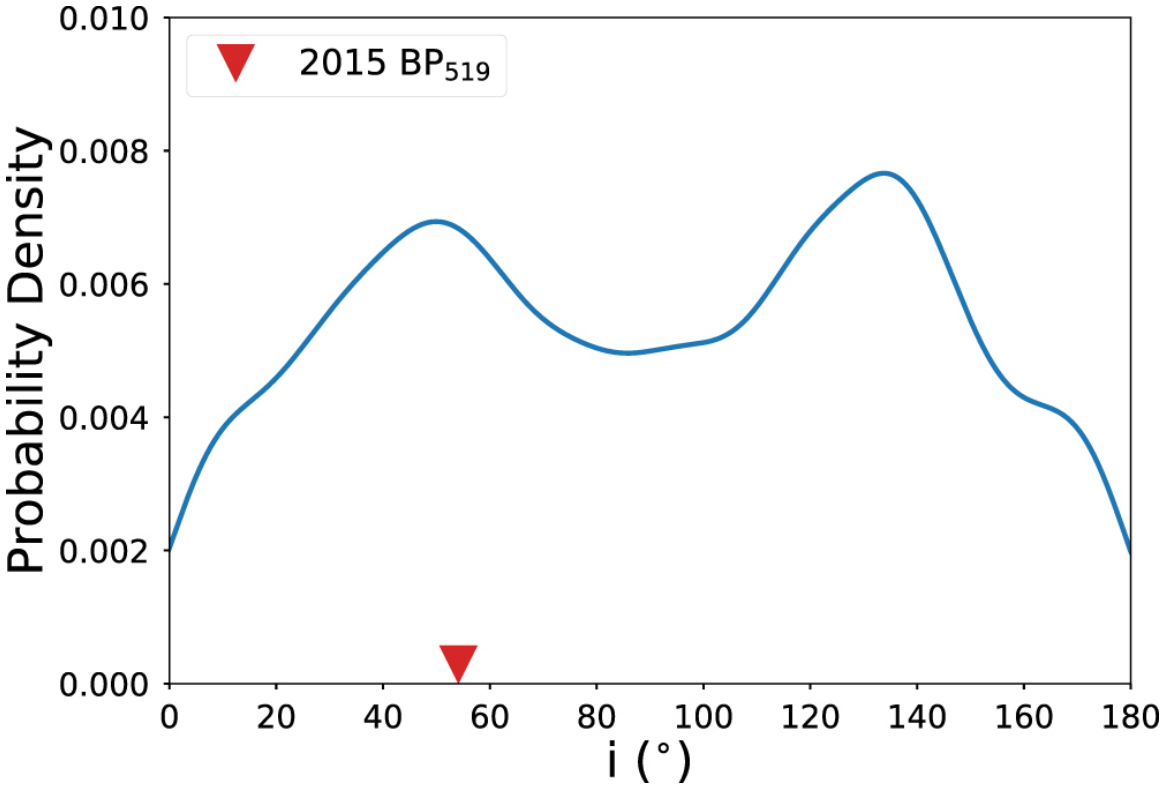

Figure 4.4: The DES selection function for the discovery of objects with the orbital elements of 2015 BP_{519} but varying inclination angles. The value for 2015 BP_{519} is shown as the red triangle. The probability distribution is normalized so that the area under the curve is unity.

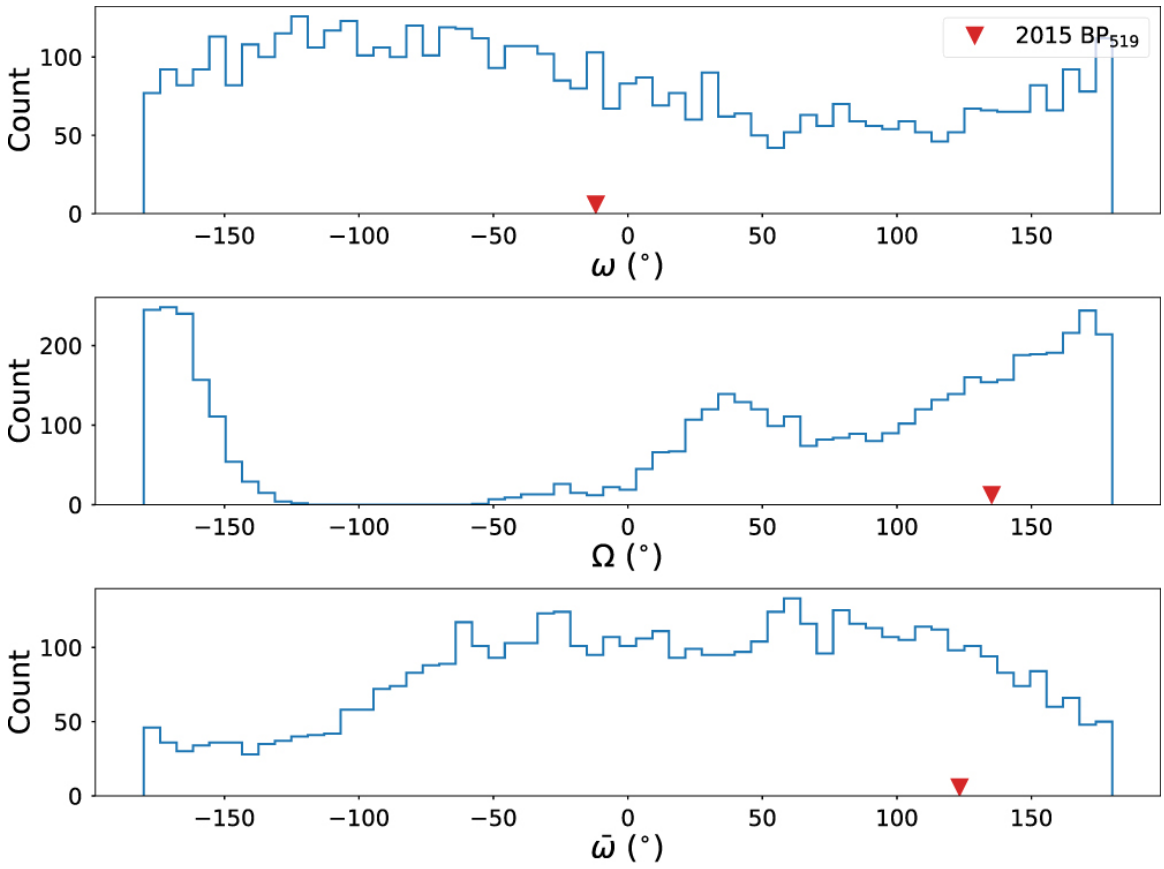

Figure 4.5: The DES selection function for the discovery of objects with the orbital elements (a, e, i) of 2015 BP_{519} but with varying angles ω, Ω. The observed values for 2015 BP_{519} are shown as red triangles in each panel. For objects with the orbital elements (a, e, i) of 2015 BP_{519}, the DES observation bias allows discovery of ω and Ω subtending most of the allowable ranges.

has (a, e, i) of (173.6 au, 0.80, 26.1°). This apparent association prompted us to examine these objects further.

Before pursuing this study further, we first needed to know whether the apparent association between the orbital elements of 2016 QU_{89} and 2016 QV_{89} was due to observational bias (I could not perform a similar analysis for 2013 UH_{15} because it was not detected by DES at all). I injected approximately 440,000 clones of the two DES objects into the survey simulator, allowing a to vary uniformly between 50 and 1000 au with $q > 30$ au and i to vary uniformly between 0° and 180°. These distributions of orbital elements are not intended to approximate the actual underlying distribution, but are rather intended to probe the targeted parameter space. Figure 4.6 shows the resulting (a, e, i) sensitivity functions of the 6446 clones that were detected by the simulation pipeline. The distributions do not show strong preference for the observed (a, e, i) values of 2016 QU_{89} and 2016 QV_{89} so I conclude that the detection of objects with such orbital similarity is not due to observational bias.

4.4.3 Discovery of an Ultra-red Neptune Trojan and Population Estimates

Trojan asteroids are minor bodies that reside in 1:1 mean-motion resonances located at the leading L4 and trailing L5 Lagrange points of major planets. In particular, Jupiter has hundreds of known Trojan asteroids, while Neptune has approximately two dozen known Trojan asteroids. The Trojan populations are thought to have come about as a result of capture mechanisms during the planetary migration era of the Solar System's history rather than in-situ formation. Evidence for the former scenario includes:

- Results from numerical simulations that show the destabilization and loss of the first Trojans (i.e. those that formed in-situ) (Chen et al., 2016; Chiang & Lithwick, 2005; Kortenkamp et al., 2004)

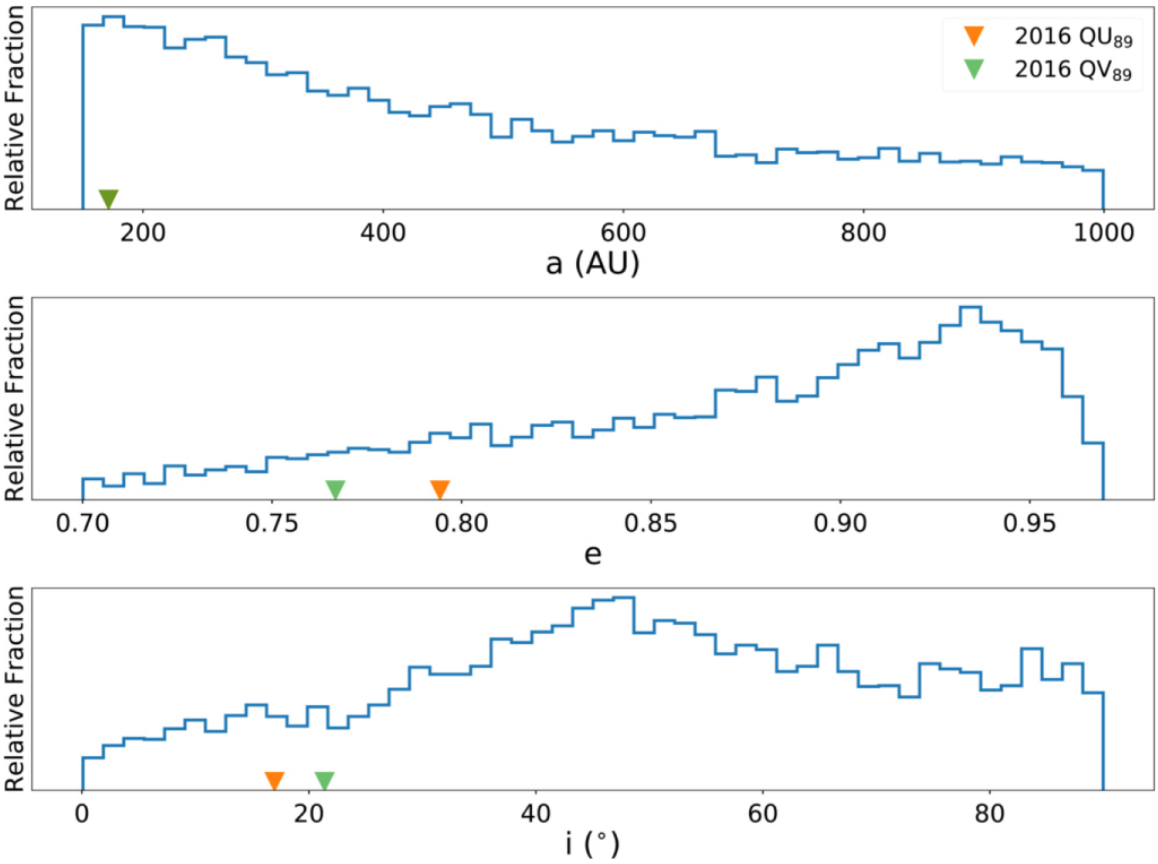

Figure 4.6: DES selection function for objects with $q > 30$ au and $150 < a < 1000$ au. The orbital elements of 2016 QV_{89} and 2016 QU_{89} are denoted by triangles. Note that the two triangles are overlapping in the top panel, due to the objects' similarity in semimajor axis.

- Observations of wide inclination distributions of both Neptune and Jupiter Trojans, which disfavors the more dynamically-calm in-situ model (Sheppard & Trujillo, 2006)

- Results from Nice Model simulations (Gomes et al., 2005; Tsiganis et al., 2005; Morbidelli et al., 2005; Levison et al., 2011) that show the chaotic capture of Jupiter Trojans during planetary migration. Chaotic capture is expected to work similarly for Neptune Trojans.

In Lin et al. (2019), we report the discovery of two new Neptune Trojans at the L4 Lagrange point, both with $i > 30°$. With the two new objects, the number of Neptune Trojans discovered by DES increases to five, and all have $i \gtrsim 10°$. Additionally, one of the new objects, 2013 VX_{30}, has colors of $g - r > 1.0$ and $r - z > 0.6$, classifying it as the first known ultra-red Neptune Trojan.

The existence of an ultra-red Neptune Trojan implies that there must necessarily be both blue/neutral and ultra-red subpopulations. The observed blue-to-ultra-red ratio for the Trojans observed by DES is 4:1. However, DES is a red-sensitive survey, optimized to detect and study high-redshift galaxies, so the detectability of the Neptune Trojan subpopulations likely depends on their colors. I use the survey simulator to quantify the effects of DES's color sensitivity on the observed ratio of blue to red objects.

We produce a synthetic population of L4 Neptune Trojans to pass through the simulator as follows:

- Semimajor axis a constant at 30.1 au.

- Eccentricity e drawn from a Rayleigh distribution ($\propto e \cdot \mathrm{e}^{-e^2/(2\sigma_e^2)}$) where $\sigma_e = 0.044$ (Parker, 2015).

- Inclination i drawn from a Brown distribution ($\propto \sin i \cdot \mathrm{e}^{-i^2/(2\sigma_i^2)}$; Brown (2001)) centered at 0° with $\sigma_i = 26°$, and with a maximum value of 60°.

- Argument of perihelion ω, longitude of ascending node Ω, and mean anomaly M uniform from $0 - 360°$, subject to the resonant condition $\phi_{1:1} = \lambda_N - \lambda_T$ where λ_N and λ_T are the mean longitudes ($\lambda = M + \Omega + \omega$) of Neptune and the Trojan, respectively.
- Mean resonant angle ϕ constant at 60° (the L4 Lagrange point).
- Libration amplitude A_ϕ drawn from a Rayleigh distribution with $\sigma_{A_\phi} = 15$.
- Absolute magnitude H drawn from a divot distribution with $\alpha_b = 0.9$, α_f=0.5, c=3.2, H_b=8.3.
- $g - r = 0.6$, $r - i = 0.2$, and $i - z = 0.1$ for the blue Trojans, while $g - r = 1.0$, $r - i = 0.5$, and $i - z = 0.5$ for the red Trojans.

Out of the 50,022 synthetic Trojans (24,934 blue, 25,088 red) with $H_r < 10$ I injected into the simulator, the moving object pipeline recovered 1,541 Trojans (661 blue, 880 red). Specifically, 15,138 (7,513 blue, 7,625 red) objects fell in the DES footprint, and 3,567 (1,579 blue, 1,988 red) objects were bright enough to have been detected. Figure 4.7 shows the inclination as a function of the longitudinal separation from Neptune for the synthetic Trojans detected by the pipeline. The five real Trojans agree well with the results of the simulation.

With the results of the simulation combined with the five detected Neptune Trojans with $H_r < 10$, we infer a total population of blue and red L4 Neptune Trojans with $H_r < 10$ of 162 ± 73. Furthermore, Gladman et al. (2012) estimate an upper limit on the number of Neptune Trojans at < 300 for $H_g < 9.16$, which corresponds to $H_r < 8.56$ assuming a color of $g - r = 0.6$. Four of the DES Neptune Trojans have $H_r < 8.56$, so using the results of the survey simulation we estimate a population size of 40 ± 20. This result agrees with that from Gladman et al. (2012).

The DES survey strategy requires more sensitivity in redder bands as opposed to bluer. This results in a slighter higher efficiency for detecting redder Solar System

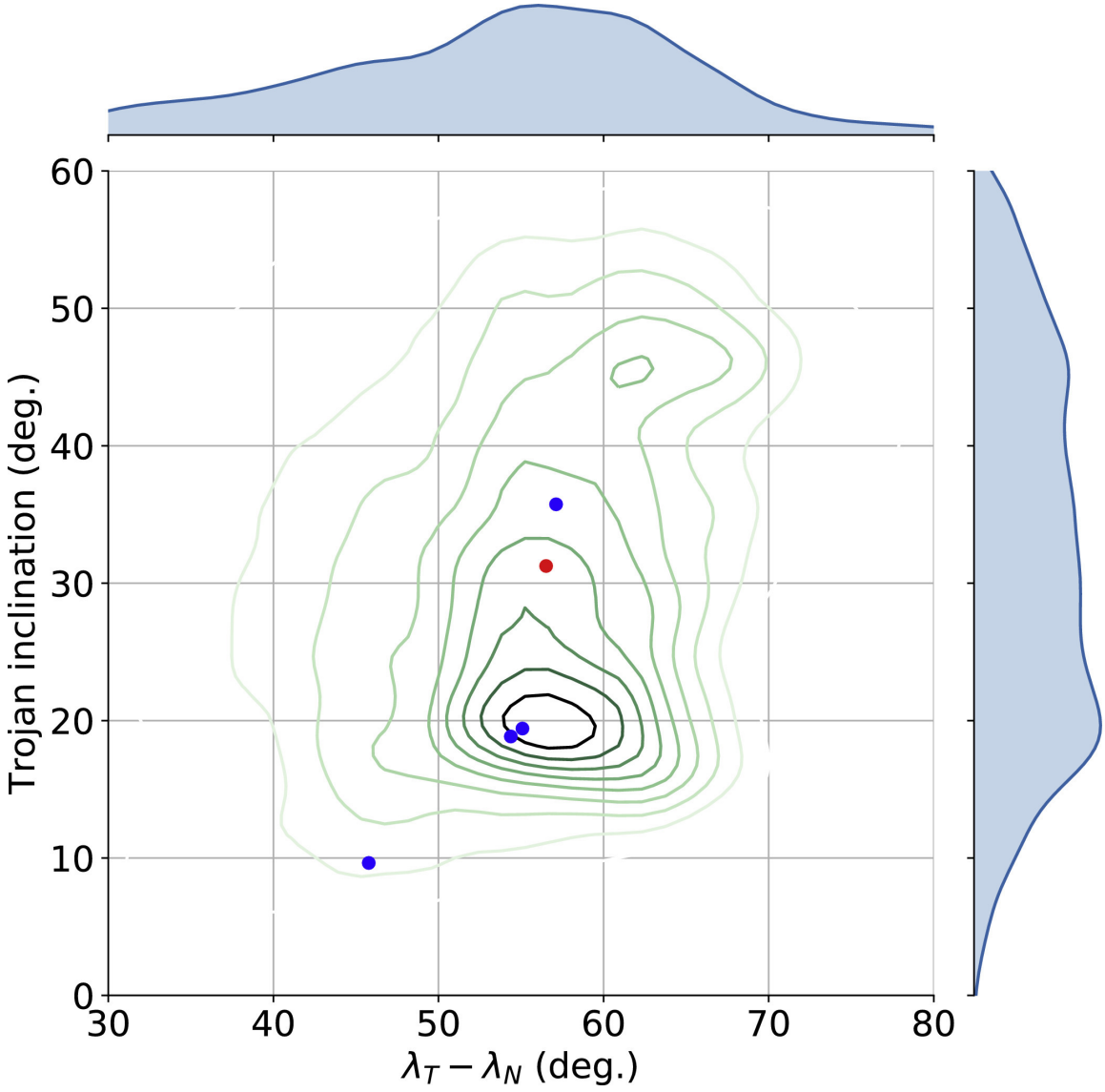

Figure 4.7: Inclination vs. longitudinal separation from Neptune for synthetic Neptune Trojans detected with the DES survey simulator. The five Trojans observed in the data are indicated by dots, with 2013 VX_{30} in red and the others in blue.

objects as well (e.g ultra-red Neptune Trojans). We observe this effect by noting the injected red-to-blue Trojan ratio ($25,088/24,934 = 1.01$) compared to the detected red-to-blue ratio ($880/661 = 1.33$). Correcting for this bias, we see that the actual red-to-blue ratio of the real objects is 5:1.

In Lin et al. (2019), we continue a step further to estimate the true intrinsic blue-to-red ratio of the Neptune Trojan population. Lacerda et al. (2014) find that ultra-red TNOs have a higher average albedo than blue Trojans, 12% compared to 6%. Additionally, Schwamb et al. (2018) find from studies of dynamically excited TNOs (from which Neptune Trojans are thought to originate) that the blue-to-red ratio for this population is 3.4. Combining these results with observations reveals that the blue-to-red ratio for Neptune Trojans could be as high as 17:1.

4.4.4 Plutinos

The plutino population of the Kuiper Belt are objects residing in a 2:3 mean-motion resonance with Neptune, named such because Pluto is one of these objects. The properties of objects in Neptune resonances, such as distributions of eccentricity or inclination or the number of objects in the resonance, encode information about whether the objects were captured into the resonance or whether they formed in-situ. Previous studies (e.g. Volk et al. 2016) have found evidence that the structure of Neptune's resonances (including the Plutinos) is a result of MMR capture as Neptune's orbit migrated outward. While DES is not extremely sensitive to the Plutino population, we report the detection of 14 Plutinos to date. Table 4.3 summarizes their orbital properties.

Table 4.3: Orbital properties of the 14 Plutinos detected by DES.

MPC	DES	a (au)	e	i (°)	q (au)	ω (°)	Ω (°)	r (au)	H_r	T_{peri} (JD)	Epoch (JD)	N_{obs}	Arc (days)
K03Q91B	ws301g1183	39.24	0.19	6.5	31.62	80.59	136.78	45.72	6.4	2421082.9	2456578.71	15	1436
	ws302g227	39.3	0.19	22.44	31.7	259.96	88.49	33.6	7.0	2447812.0	2456328.59	21	368
	ws302g158	39.35	0.22	9.85	30.71	257.86	145.23	31.08	7.3	2459848.5	2456564.83	24	1508
	ws302g61	39.36	0.15	11.6	33.33	75.62	146.69	45.07	5.7	2416814.3	2456564.84	30	1514
k9372	ws301g1077	39.38	0.11	22.35	35.0	42.23	164.18	43.27	5.1	2419001.8	2456537.84	24	1515
	ws302g214	39.38	0.29	19.01	27.95	275.14	173.62	30.96	7.9	2464097.6	2456247.62	30	1832
	ws302g485	39.39	0.28	10.37	28.34	285.48	129.49	29.29	8.1	2460932.1	2456569.7	25	1479
K12TW4D	ws301g208	39.39	0.14	9.58	33.93	190.99	114.62	36.34	6.7	2444151.1	2456544.82	24	1448
	ws302g5	39.4	0.24	24.95	29.83	247.63	58.81	34.54	6.9	2444664.7	2456569.72	32	1510
	ws302g53	39.41	0.25	16.61	29.61	329.34	68.27	30.1	7.5	2459992.1	2456545.8	21	1175
o4555	ws302g101	39.41	0.24	18.8	29.85	172.77	158.75	32.54	6.0	2447941.9	2456569.77	29	1532
	ws302g149	39.42	0.28	43.51	28.41	318.84	32.82	29.03	7.9	2453027.9	2456544.84	15	787
K14SY9K	ws302g117	39.47	0.29	9.4	28.03	315.9	59.9	28.07	7.4	2455802.6	2456569.69	19	419
	ws301g997	39.48	0.28	5.22	28.41	248.8	139.57	28.58	7.6	2458364.4	2456537.86	27	1152

To test the functionality of the survey simulator, I inject synthetic plutinos defined by the best fit model of Volk et al. (2016):

- Semimajor axis a uniform from 39.2–39.6 au.
- Eccentricity e drawn from a Gaussian distribution ($\propto \mathrm{e}^{-(e-e_c)^2/(2\sigma_e^2)}$) where $e_c = 0.175$ and $\sigma_e = 0.06$.
- Inclination i drawn from a Brown distribution ($\propto \sin i \cdot \mathrm{e}^{-i^2/(2\sigma_i^2)}$; Brown (2001)) centered at 0° with $\sigma_i = 12°$.
- Libration amplitude A_ϕ drawn from a triangular function that starts at $A_{\phi,min} = 0°$, rises linearly to a peak value at $A_{\phi,c} = 75°$, and falls linearly to zero at $A_{\phi,max} = 155°$.
- Mean resonant angle $\phi = 180° + A_\phi \sin(2\pi x)$ where x is a random number from 0–1.
- Longitude of ascending node Ω, and mean anomaly M uniform from $0 - 360°$.
- Argument of perihelion ω is then given by $\omega = \frac{1}{2}\phi - \frac{3}{2}M - \Omega + \lambda_N$ where $\lambda_N = M_N + \Omega_N + \omega_N$ is the mean longitude of Neptune.
- Absolute magnitude H drawn from a single-slope distribution with $\alpha = 0.9$.

Figure 4.8 shows the results of this simulation. I note that the inclination and absolute magnitude distributions provide a good match to the observed distributions, but the eccentricity distribution appears not to agree as well. Further investigation has revealed a strong dependence of the observed eccentricity on the object's heliocentric distance as shown in the left panel of Figure 4.10. Notably, the eccentricity distribution of the real detections closely follows that of the closest heliocentric distance bin, $\sim 27 - 34.4$ au. The right panel of Figure 4.10 then explains why this is the case – most of our real detections fall into the $\sim 27 - 34.4$ au distance bin. The exact

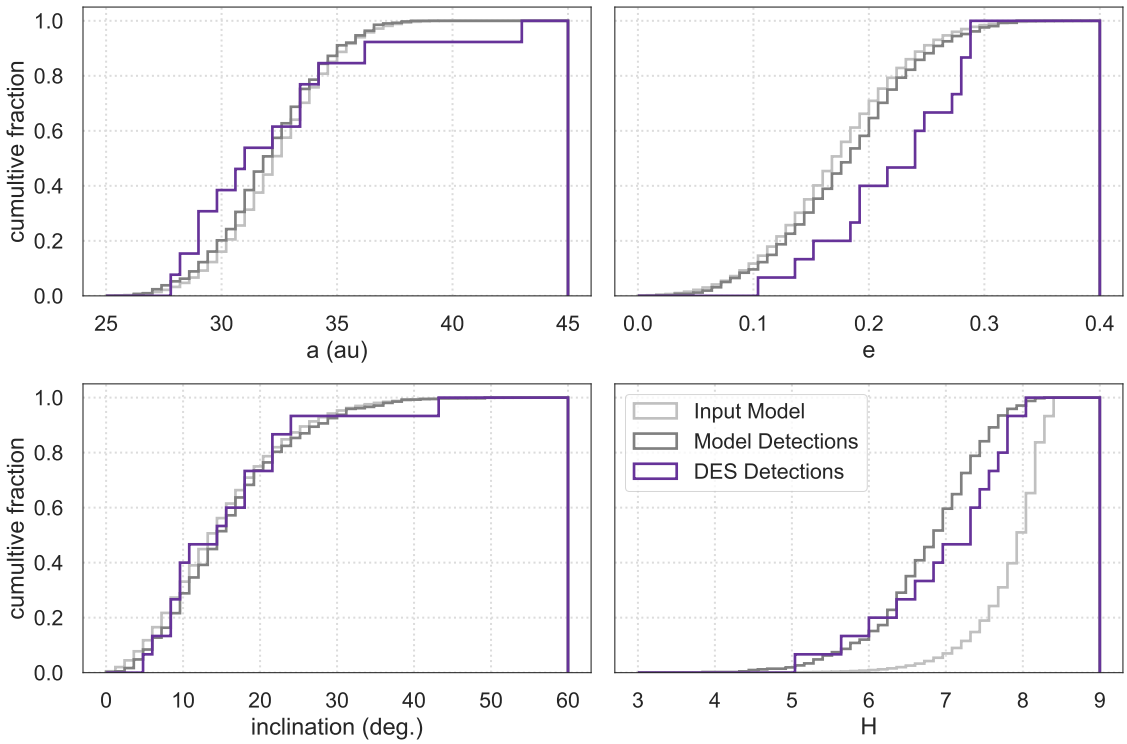

Figure 4.8: Comparison of the a, e, i, H distributions of the input plutino model (light gray), the detections of the input model recorded by the survey simulator (dark gray), and actual DES detections (purple). The a, i, H distributions appear to match reasonably well between the survey simulator detections and real detections. The e distribution appears not to match as well. Future investigations will determine whether this results from the survey simulator or is an indication that a different model is needed to describe the DES plutinos.

cause of the discrepancy between the observed eccentricity distribution and the synthetic eccentricity distribution remains unknown, but the correlation with heliocentric distance provides a promising avenue for investigation.

4.5 Summary

In this chapter, I outline the procedure of the DES survey simulator. The resulting code takes an input model of the Kuiper Belt or other Solar System population and subjects it to the biases of the survey. The simulator considers each object in turn

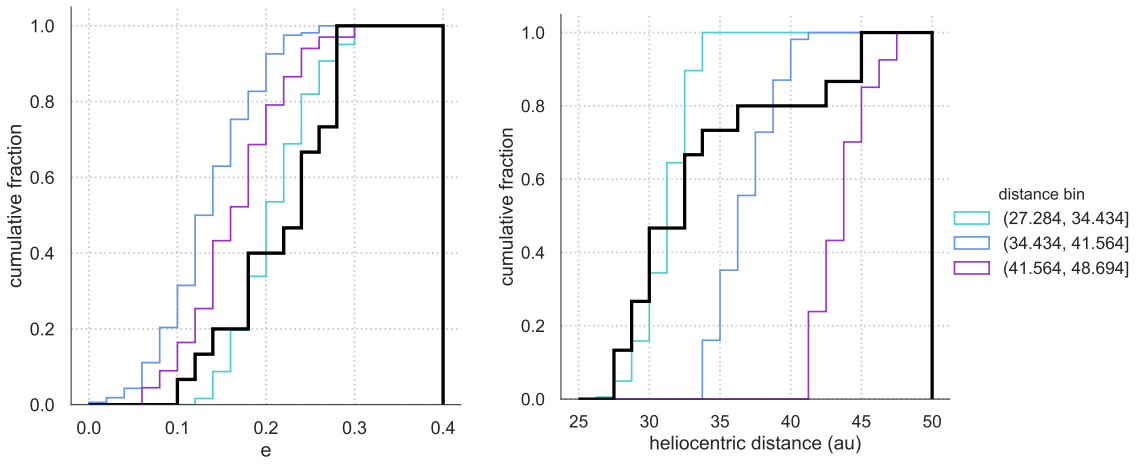

Figure 4.10: The left plot shows cumulative distributions of the eccentricities of the real plutino detections (black) compared to the eccentricities of the synthetic detections by heliocentric distance bin (colored histograms). The real eccentricity distribution appears to closely follow that of the synthetic objects with heliocentric distances of $\sim 27{-}34.4$ au. The right plot shows the cumulative histograms of heliocentric distance and confirms that most of the real detections fall in the same heliocentric distance range of $\sim 27 - 34.4$ au. Interestingly, there is a relative dearth of real detections in the range $34.4 - 41.5$ au, but the exact cause is not yet known.

and determines whether it fell in a DES exposure and whether the object would have been bright enough to observe. The simulator's output is a transient catalog that can be processed like any other transient catalog. It is straightforward to either run the full moving object linking pipeline on the output catalog or to parameterize the linking pipeline in order to more quickly evaluate whether individual detections would have been linked into orbits.

I apply the simulator to a number of newly discovered objects by DES in order to evaluate the effects of observational bias on their observed properties (e.g. orbital elements or colors):

- The high-inclination extreme TNO 2015 BP_{519}, for which the simulator showed there is no significant observational bias associated with 2015 BP_{519}'s high inclination due to DES's coverage at high ecliptic latitudes.

- The closely associated 2016 QV_{89} and 2016 QU_{89}, for which the simulator showed that the apparent similarity between the two objects' orbital elements is not due to observational bias and their discovery in the small-area, 3-square-degree Supernova fields.

- The ultra-red 2013 VX_{30}, together with the four blue Neptune Trojans detected by DES, for which we confirmed that DES detects redder Trojans with higher efficiency. With the results of the simulation, we estimated a blue-to-red ratio for the Neptune Trojans of 17:1 and a total population size of 162 ± 73 objects with $H_r < 10$ and 40 ± 20 objects with $H_r < 8.56$, consistent with previous estimates.

- The plutinos, for which we found that the a, i, H distribution of the 14 DES plutinos generally agreed well with the best fit model defined in Volk et al. (2016), but that the e distribution did not agree as well. Correlation between the real eccentricity distribution and the simulated eccentricity distributions

binned by heliocentric distance suggests an underlying systematic error or a possible needed adjustment to the synthetic model. Near future investigation will elucidate the true cause of the discrepancy.

CHAPTER V

On the Orbital Clustering of Extreme Trans-Neptunian Objects in the Dark Energy Survey

This Chapter from Section 5.2 through Section 5.3 comprises part of a **paper to be published as:** Hamilton, S. J., Napier, K. J., Gerdes, D. W., et al. 2019, in prep.

5.1 Introduction

The naked eye planets (Mercury, Venus, Mars, Jupiter, and Saturn) have been known for centuries. It was not until Galileo pointed a new device called a "telescope" toward the sky that humanity began to study all that had been previously unseen. Perhaps most famously, Galileo discovered the four major moons of Jupiter (Io, Europa, Ganymede, and Callisto) using his telescope, but he unknowingly also recorded observations in 1612 and 1613 of a previously undiscovered planet later realized to be Neptune. Yet Galileo never officially noted the observations as a possible planet, likely because Neptune had just reached quadrature and thus appeared stationary, so Neptune remained hidden for another 230 years.

Uranus also eluded discovery for centuries because it was mistaken for a star. The earliest recorded observations were taken by John Flamsteed in 1690. Pierre Charles

Le Monnier further observed it between 1750 and 1769, but William Herschel was the first to recognize it as a moving object in 1781. He first called it a comet, but when no out-gassing was observed and further observations were taken, the object was confirmed as a planet.

By 1843, it had become clear that Uranus's observed position was deviating significantly from the positions calculated using Kepler's and Newton's Laws. John Couch Adams and Urbain Le Verrier independently and simultaneously calculated the properties (mass, orbit, and position) of a perturbing body that could reproduce the observed deviations in Uranus's position. Johann Gottfried Galle discovered Neptune within 1° of the mathematically predicted position on September 24, 1846.

Since the successes of Neptune's discovery, a variety of new planets have been proposed throughout the years to explain purported deviations in expected positions of the known planets. Le Verrier noted Mercury's perihelion precession in 1859 and proposed a new planet nicknamed "Vulcan" inside the orbit of Mercury. Observations failed to reveal such a planet, and the problem of Mercury's perihelion precession was solved in 1915 with Einstein's Theory of General Relativity. Perhaps most notably, Pluto was predicted in much the same way as Neptune, by using remaining irregularities in Uranus's orbit to predict the position of an exterior planet. Ironically, Pluto was discovered near the predicted position by Clyde Tombaugh in 1930. Newspapers first reported that it was possibly bigger than Jupiter, but Pluto remained unresolved with even the most powerful telescopes. Furthermore, it was too faint to be a Jupiter-sized planet, and its mass was revised throughout the 1900s until the discovery of Charon finally allowed for an accurate mass measurement. At 0.2% the mass of Earth, Pluto could not account for the remaining deviations in Uranus's position. Ultimately, Voyager 2's flyby of Neptune revised estimates of its mass and eliminated the need for another planet.

During the past 25 years of Kuiper Belt exploration, since the second Kuiper Belt

object (1992 QB_1) was discovered by Jewitt & Luu (1993), various distant hypothetical planets have been proposed to explain different structural properties of the Kuiper Belt. One such planet arose from the argument that the mean orbital plane of the distant Kuiper Belt is "warped" (Volk & Malhotra, 2017). That is, objects with $a = 50 - 80$ au are inclined overall, a feature that could be explained by the presence of a Mars-sized planet with $a \sim 65 - 80$ au and moderate inclination. Trujillo & Sheppard (2014) noted the alignment of the arguments of perihelion, ω, around 0° of the most distant TNOs ($a > 150$ au and $q > 30$ au) and postulated that a $5M_\oplus$ planet at ~ 200 au could explain the alignment via Kozai-Lidov oscillations. However, the proposal could not explain the alignment of all TNOs with $150 < a < 500$ au. Nevertheless, the discovery of additional TNOs with $a > 150$ au that exhibited alignment in both argument of perihelion and longitude of ascending spurred the new proposal of a hypothetical distant planet in the Solar System called Planet Nine (Batygin & Brown, 2016; Batygin et al., 2019).

In its original form, Planet Nine was proposed to be a $10M_\oplus$ planet with $a \approx 700$ au, $e = 0.6$, and $i \approx 30°$ The original hypothesis used the six long-period "extreme" TNOs known at that time that were determined to be dynamically stable. This particular iteration of a new, distant planet could also explain several other anomalies noted in the distant Kuiper Belt ($a > 250$ au) that cannot otherwise be explained by gravitational sculpting processes by the other known planets. These anomalies include the clustering in argument of perihelion, ω; clustering in longitude of perihelion, $\varpi = \omega + \Omega$; clustering of the orbital planes, which further incorporates the inclination of the orbit; perihelion distances beyond the gravitational influence of Neptune ($q \gtrsim 45$ au, with Sedna and 2012 VP_{113} having $q > 70$ au); and the presence of highly-inclined and retrograde TNOs.

The current census of long-period TNOs now consists of 14 ETNOs, and the Planet Nine hypothesis has been modified to account for new information provided by the

new objects (Batygin et al., 2019). The best-fit model of Planet Nine is now a $5M_{\oplus}$ planet with $a = 400-800$ au, $e = 0.2-0.5$, and $i = 15-25°$. However, there remain a number of alternative explanations for the anomalous features observed in the distant Kuiper Belt. One proposal by Madigan & McCourt (2016) suggests that the Kuiper Belt's own self-gravity leads to a secular evolution of inclinations and eccentricity that results in a clustering in argument of perihelion. However, this explanation requires a total Kuiper Belt mass of $1-10M_{\oplus}$, much larger than previous estimates of $\sim 0.1M_{\oplus}$, and does not reproduce the clustering in longitude of perihelion and orbital plane.

Perhaps the most viable alternative to the Planet Nine hypothesis is observational bias. That is, the observed orbital clustering of the longest period TNOs is an artifact of the observing strategies of the surveys that discovered them. The ETNOs are on long, elliptical orbits, rendering them detectable only very near perihelion. One can envision a situation in which observing strategies result in detections of ETNOs that appear to be clustered when, in fact, the underlying distributions in orbital angles are uniform. This hypothesis has been examined several times over the past three years. In particular, Brown (2017) and Brown & Batygin (2019) attempt to circumvent the lack of reported discovery circumstances for most of the 14 ETNOs by examining the rest of the TNOs reported to the Minor Planet Center (MPC). To do so, they compare brightnesses and on-sky positions of clones of the ETNOs with uniform orbital angles to detections of real TNOs reported to the MPC. If a clone fell within 1° of a real TNO discovery detection and was at least as bright as the real TNO, it was considered found. This method results in probability distribution functions in the orbital angles of each ETNO, which can then be used to evaluate the likelihood that the underlying orbital distributions are uniform. Brown & Batygin (2019) find that this likelihood is $< 1\%$.

Conversely, the Outer Solar System Origins Survey (OSSOS; Bannister et al. 2016) has independently detected four ETNOs with well-characterized discovery cir-

cumstances. Shankman et al. (2017) used the OSSOS Survey Simulator (described in Jones et al. 2006; Petit et al. 2011; Bannister et al. 2016) to generate ETNOs according to predefined distributions and systematically evaluate which objects would have been detected by OSSOS. The simulations probe the observing biases of the survey and allow a robust comparison between the observed properties of detected ETNOs and the simulated ETNOs. In particular, Shankman et al. (2017) find that the clustering of the OSSOS detections can be explained by observational bias and therefore no Planet Nine is needed. Lawler et al. (2017) further argue that the existence of a distant super-Earth planet would produce distinctly different structure in the scattering disk and distant Kuiper Belt, but that such a signature is currently undetectable by existing surveys.

It is important to note that the bulk of the known ETNOs have been found using three separate surveys with three separate strategies. The surveys of DES and OSSOS were not tailored to minimize bias toward discovering ETNOs. However, on ongoing survey by Sheppard and Trujillo (S&T, Sheppard & Trujillo 2016; Sheppard et al. 2019) has been designed specifically to probe the argument of perihelion space and longitude of perihelion space in a more uniform manner by imaging regions of sky up to $\sim 30^\circ$ above and below the ecliptic plane and spanning all ecliptic longitudes. The known TNOs are roughly evenly distributed between DES, OSSOS, and S&T, and the clustering signal still remains. Yet, how their observational biases combine to influence the population of detected ETNOs remains a topic of study (e.g. Napier et al. 2019). Combining the three surveys together will yield stronger constraints than any of the surveys individually. However, even if a combined study indicates that observational bias accounts for the observed clustering of the ETNOs, the existence of the object 2015 BP_{519} (currently also explained by a Planet Nine) would still require additional explanation beyond the known Solar System.

Motivated by the ongoing tension regarding the effects of observational bias on the

observed orbital properties of the known ETNOs, this chapter examines the inventory of ETNOs detected by the Dark Energy Survey and quantifies the effect of DES's observational biases on the orbital clustering exhibited by these objects.

5.2 Evaluating the Observational Bias of Extreme TNOs Detected by DES

The significance of the physical clustering of the most distant TNOs with $a >$ 150 au and $q > 30$ au (known as "extreme" TNOs, or ETNOs), and more specifically those with $a > 250$ au, has been contested in recent literature (Shankman et al., 2017; Brown, 2017). As of this writing, DES has discovered 10 TNOs with $a > 150$ au and $q > 30$ au, summarized in Table 5.1. Four of these additionally have $a > 250$ au. All 10 objects were discovered in DES `wsdiff` data (see Figure 2.2) relatively close to their perihelia. This is not surprising given their large values of a and e. The objects were detected in the `wsdiff` dataset described in Section 2.2.1 and the transient catalog was processed as outlined in Section 2.3. Notably, all ETNOs with $a > 250$ au have $q > 35$ au. One ETNO, ws302g153, additionally has $q > 45$ au, argued to be a cutoff for detachment from Neptune even when accounting for Neptune's migration through the Kuiper Belt (Brasser & Schwamb, 2015). The DES sample constitutes a second self-contained dataset, after that of OSSOS (Shankman et al., 2017) – that is, the DES ETNO sample is a completely independent sample from any previous sample, with any previously-known ETNOs having been independently discovered using the DES moving object search pipeline.

5.2.1 Observational Bias of Synthetic ETNOs

I assume $q > 30$ au to be consistent with previous works (Shankman et al., 2017; Brown, 2017). I additionally impose $a > 250$ au in order to study the region of

Table 5.1: Barycentric osculating orbital elements of TNOs with $a > 150$ au and $q > 30$ au detected by DES

MPC	DES	a (au)	e	i (°)	q (au)	ω (°)	Ω (°)	r (au)	H_r	T_{peri} (JD)	Epoch (JD)	N_{obs}	Arc (days)
	ws200g520	158.49	0.77	17.4	36.66	27.4	293.44	37.17	6.3	2454070.2	2456540.57	14	1832
	ws200g30	161.46	0.72	4.82	45.92	123.36	219.36	46.08	6.3	2455855.5	2457657.63	8	39
2015 SO_{20}	ws302g147	164.77	0.8	23.41	33.17	354.78	33.63	33.4	6.3	2457992.2	2456545.85	16	443
2016 QV_{89}	ws302g10	171.62	0.77	21.39	39.96	281.09	173.22	50.95	5.7	2469915.1	2456247.59	121	1882
2016 QU_{89}	sn266y4	171.4	0.79	16.98	35.2	303.33	102.9	35.9	7.9	2459260.8	2456575.64	39	1559
	ws302g63	232.92	0.85	13.22	35.11	296.29	118.98	36.81	7.1	2460726.5	2456568.80	32	1525
	ws301g157	314.39	0.88	6.5	38.13	265.48	94.73	38.26	6.8	2455322.0	2456544.71	31	1479
2013 RF_{98}	2013 RF98	358.2	0.9	29.54	36.1	312.05	67.63	36.3	8.6	2455178.3	2456547.84	45	1192
2015 BP_{519}	ws121g0	449.42	0.92	54.11	35.25	348.06	135.21	55.08	4.2	2473015.0	2456988.83	27	1175
	ws302g153	462.24	0.9	12.4	46.01	262.92	104.8	46.34	5.9	2454268.8	2456547.89	19	1822

parameter space most hotly contested by recent literature (Shankman et al., 2017; Brown, 2017; Brown & Batygin, 2019). To evaluate the effects of observational bias on the ETNOs detected by DES, I explore two different orbital element distributions intended to represent a (1) realistic model and (2) a more extreme model:

1. **Baseline model**

   - Semi major axis distributed according to $a \propto a^{0.7}$, with a spanning 250 au to 1000 au
   - Eccentricity e uniform from 0.7 to 1.0, with the constraint that $q > 30$ au
   - Inclination i drawn from a $\sin(i)\times$ Gaussian distribution with $i_{center} = 0°$ and $\sigma_i = 15°$ (Kavelaars et al., 2008; Gladman et al., 2012)
   - Absolute magnitude H drawn from a knee distribution as in Fraser et al. (2014) with $H_{min} = 4.0, H_{max} = 9.0, H_{break} = 7.7, \alpha_b = 0.87$, and $\alpha_f = 0.2$.
   - ω, $\Omega \in [0°, 360°]$ uniformly distributed, making ϖ uniform as well.

   This parametrization is not intended to exactly represent the underlying population, but is rather intended simply to be *more* representative than Model 2 described below.

2. **Uniform model** – Same as Model 1 but with $a \in [250 \text{ au}, 1000 \text{ au}]$ uniformly

distributed and $i \in [0°, 65°]$ also uniformly distributed.

I find some sensitivity to the choice of inclination model, but the choice does not significantly change my conclusions. I proceed using the baseline model above.

My simulations show that DES has at least some sensitivity to nearly the full range of ω, Ω, and ϖ (gray histograms of Figure 5.1). As DES is a largely off-ecliptic survey with only the SDSS Stripe 82 region intersecting the ecliptic plane, our sensitivity to the argument of pericenter, ω, exhibits a single-peaked distribution that is offset from both 0° and 180°. Additionally, because DES observes in the Southern hemisphere, our sensitivity to objects that reach perihelion at northerly latitudes is greatly reduced, as seen from $50° < \omega < 150°$. Finally, DES maintains some sensitivity through all values of the longitude of ascending node, Ω, due to the coupling between Ω and the inclination, i, a feature discussed at length in Shankman et al. (2017) and demonstrated for DES in Figure 5.2. Our bias in ϖ is then strongly peaked near $\varpi \sim 0°$.

5.2.2 Clustering Significance of the DES ETNOs

The DES ETNO detections (purple markers in Figure 5.1) appear to roughly follow the expected bias, though the values in Ω do appear to the eye to be clustered in a region where DES is not most sensitive. Also notable is the outlier in the bottom panel of Figure 5.1 – this object is 2015 BP_{519}, already demonstrated in Becker et al. (2018) to be the most extreme TNO discovered to date. In order to quantify the (dis)agreement of the observations with the biased synthetic detections, whose angles were drawn from uniform underlying distributions, I perform a variety of statistical tests.

As has been done in previous works (Shankman et al., 2017), I use Kuiper's test, a cyclic-invariant version of the Komolgorov-Smirnov test, to compare the detected distributions to the simulated distributions. I randomly draw four objects (the num-

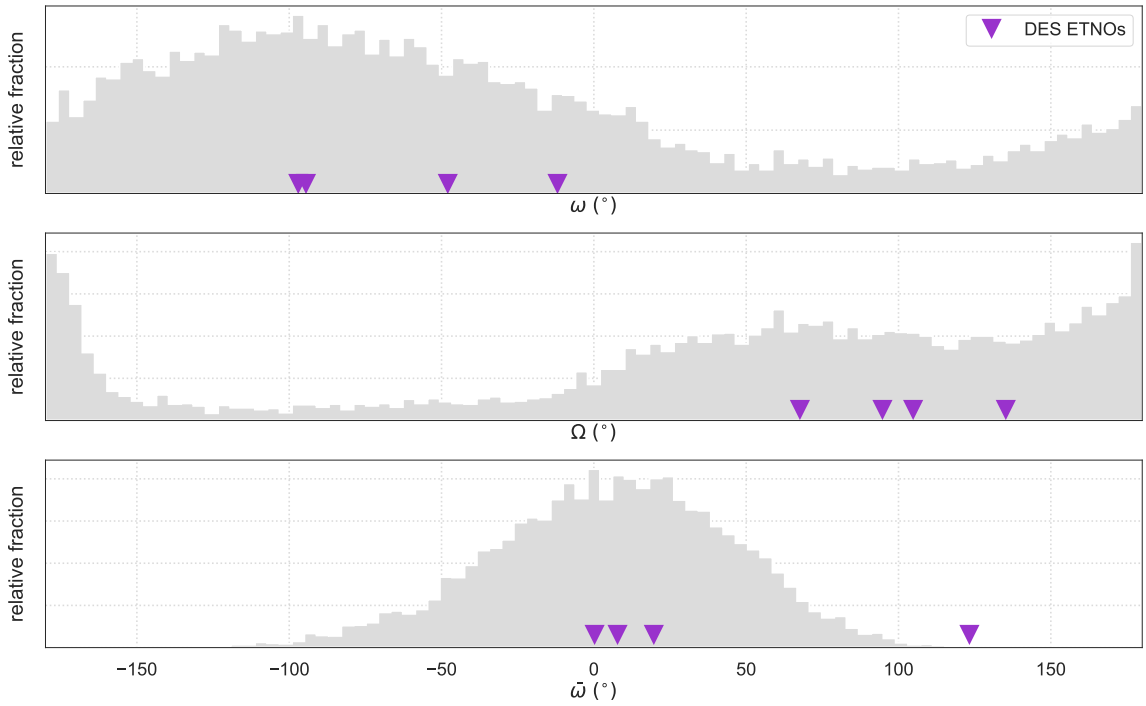

Figure 5.1: The detection bias for $a > 250$ au TNOs in DES. The grey histograms show synthetic TNOs drawn from the pseudo-realistic model after having been forward-biased by the DES selection functions. Purple triangles denote the observed values of the angles for ETNOs detected by DES.

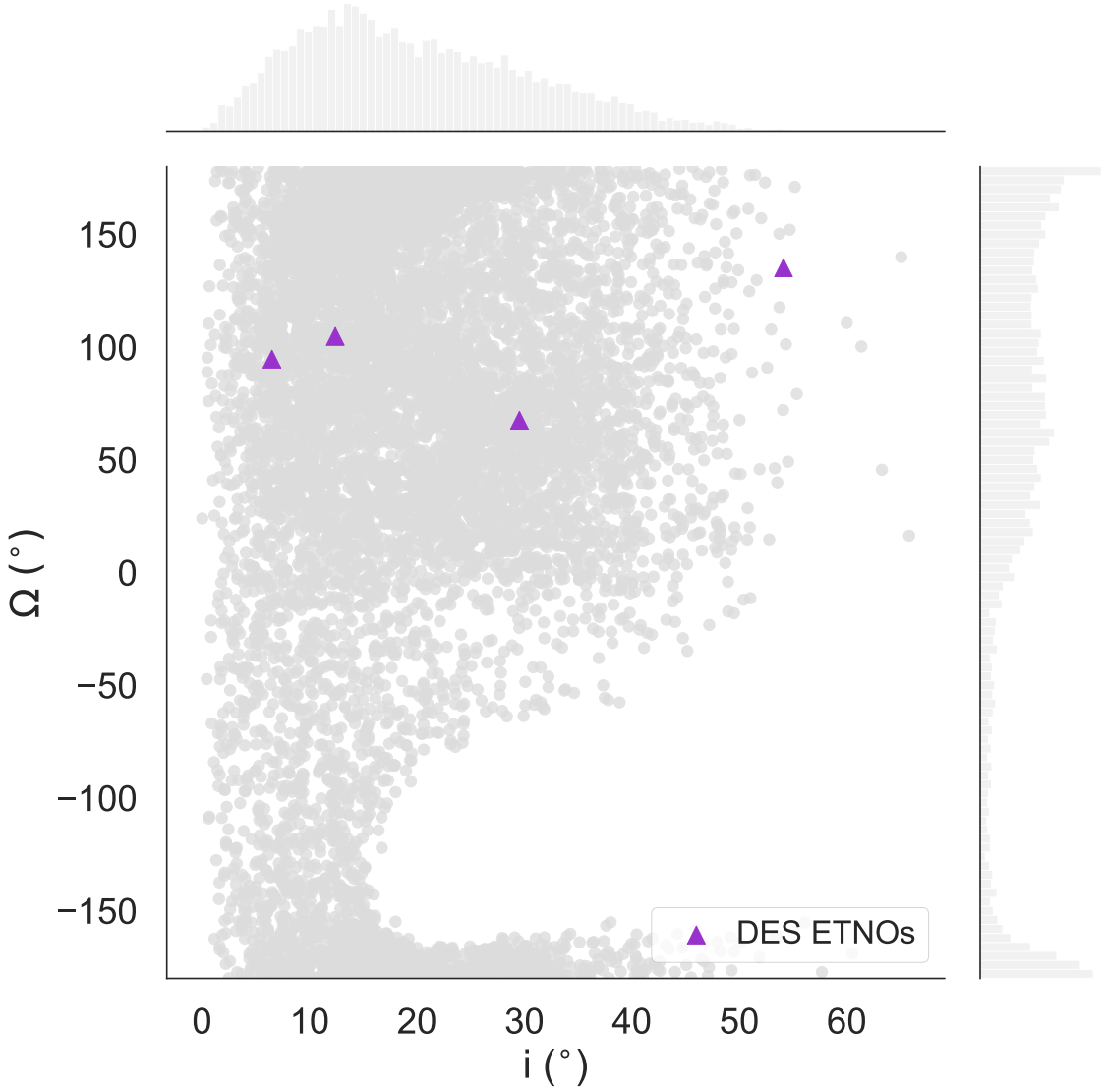

Figure 5.2: Ω vs. i for $a > 250$ au TNOs in DES. The gray points indicate simulated detections from the pseudo-realistic model, while the purple triangles denote real DES detections. I note that despite some sensitivity to the full range of Ω, the detections appear to cluster in the range $60° < \Omega < 140°$, which happens to correspond to the expected region of clustering in Ω by Planet Nine.

ber of real DES detections) 50,000 times from the simulated detections and calculate the Kuiper test statistic, where a larger score indicates dissimilar distributions. I consider ω, Ω, and ϖ in turn. When compared to the Kuiper score for the four real detections, I find that 22% of trials in ω yield a larger test score, meaning the null hypothesis in which the values of ω originate from a uniform underlying distribution is rejectable at 78% (that is, likely not rejectable). I additionally find that 43% of trials in ϖ yield a larger test score than for the real detections, meaning that the null hypothesis is rejectable at 57%. The clustering in Ω is perhaps most suggestive, with only 7% of trials having a larger Kuiper test statistic than the detected sample. The null hypothesis is then rejectable at 93% (that is, likely rejectable). These results are shown in Figure 5.3.

With the one-dimensional Kuiper statistic, some information is lost. In considering a two-dimensional statistic I binned the simulated detections in Ω vs. ϖ. I then determined contours by ordering the 2D bins by probability density and selecting the top n of N_{tot} bins such that $\sum n \leq c \sum N_{tot}$, where c is the contour level being considered. In this way, $c = 0.05$ represents the top 5% of bins, and so on. The binomial probability for contour c is then given by

$$P(c) = \sum_{i=0}^{n_{out}} \binom{4}{i} c^{4-i}(1-c)^{i} \tag{5.1}$$

where n_{out} is the number of objects outside the contour c. $P(c)$ then represents the probability of finding n_{out} or fewer objects outside the contour c, given the assumption that the orbital angles originate from a uniform underlying distribution. Results are shown in Figure 5.5. The probability approaches 1 near $c = 0$ because if 0% of the probability is contained within the contour, one would also expect zero detections to be inside the contour. Similarly, near $c = 1$, the probability again approaches 1 because if all of the probability is contained within the contour, one would also expect

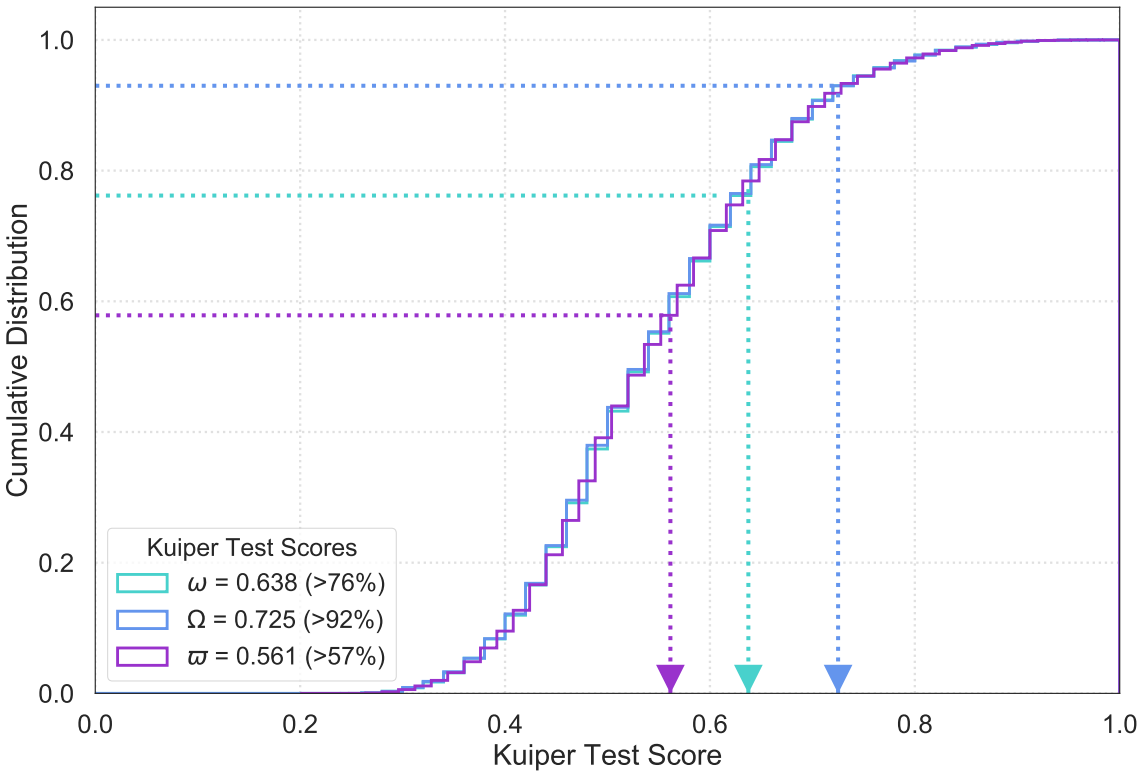

Figure 5.3: The Kuiper test statistic distributions resulting from randomly drawing four objects from the simulated distributions. The triangles denote the Kuiper scores for the real DES detections for each of ω, Ω, and ϖ, with the corresponding $x-$ and $y-$values marked by the dotted lines.

all of the detections to be contained. The goal of this statistical measure is to examine how likely it is to observe the degree of clustering measured without having to specify a specific value. I find the minimum probability to be 8% at $c = 0.3$, indicating that the objects are highly clustered when compared to expectation for the 30% contour. This result is perhaps highly suggestive, but not conclusive, of a higher-than-expected degree of clustering when compared to results of survey simulations.

5.3 Discussion and Conclusions

I have reported the detection of four ETNOs with $a > 250$ au and $q > 30$ au by the Dark Energy Survey. I apply the survey simulator to the population of ETNOs detected by DES to quantify the observational bias of these detections as it pertains to the proposal of a new, distant planet in the Solar System. I find that the null hypothesis in which the orbital angles of the ETNOs originate from a uniform underlying distribution is not rejected, mitigating the need for a new distant planet in the outer Solar System. However, it is difficult to draw strong conclusions with only four detections. Further, Figure 5.1 demonstrates that DES has limited distinguishing power between the null hypothesis where the orbital angles are assumed to be uniform and the clustering argument of Planet Nine at $\varpi \sim 0^\circ$ because the DES selection function peaks where the clustering due to Planet Nine is expected to occur. Stronger constraints can come from combining data from characterized surveys as additional detections are made (Napier et al., 2019).

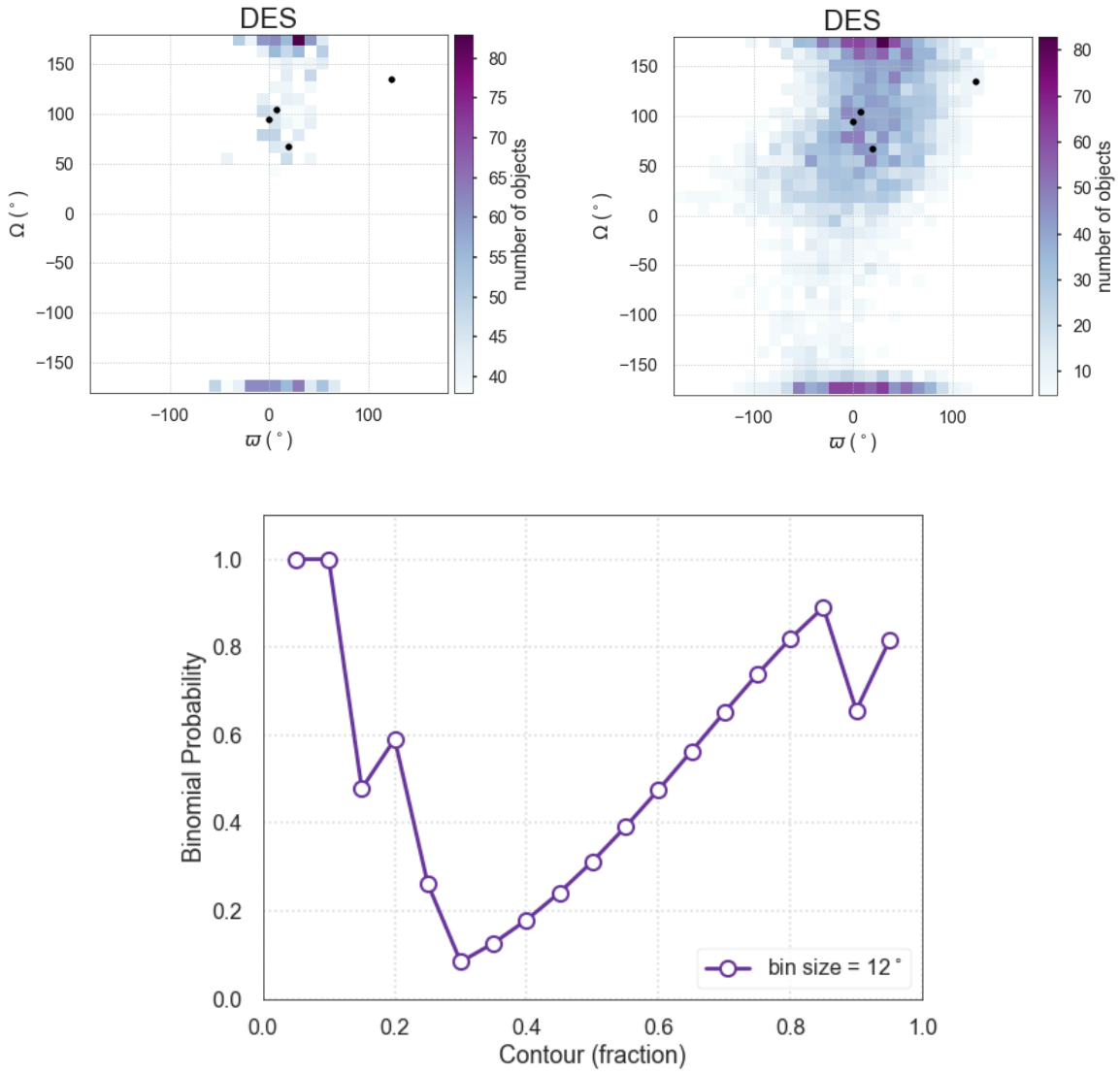

Figure 5.5: A demonstration of the binomial probability calculation for DES detections spanning contours enclosing 5-95% of the probability. The procedure is described in Section 5.2.2. The top left and top right panels show the 30% and 95% contours, respectively. They are discrete contours, rather than smooth contours, because I calculated the probabilities in $12° \times 12°$ bins to ensure sufficient numbers for the statistical calculation. The bottom panel shows the result of Equation 5.1 for each of the contours. Sharp drops occur when a DES detection becomes enclosed within a contour.

CHAPTER VI

Conclusions

6.1 Thesis Summary

The Dark Energy Survey is uniquely positioned to make a significant contribution to the field of TNO research due to its wide area and deep magnitude coverage at high ecliptic latitudes, a region of the Solar System that has not previously been studied thoroughly. This thesis presents initial work and results from repurposing this cosmological survey to study trans-Neptunian objects in the distant Solar System.

Chapter II provided a description of how DES has been adapted to be a powerful TNO discovery machine. I described how the difference imaging pipeline developed by the DES Supernova working group, `DiffImg`, was adapted to produce single-epoch detections of transient objects in both the DES supernova fields and the Wide Survey. The resulting transient catalog was processed using our moving object pipeline, also described in the Chapter, resulting in the detection of 341 objects. Approximately 50 of these were previously known, and approximately 250 had inclinations $i > 10°$. These 341 objects were detected in the `wsdiff` dataset, which comprises approximately 40% of the total survey data. A new and improved transient catalog was recently produced, and analysis of those data through our moving object pipeline is currently in progress. I also described efforts to lay groundwork to expand DES beyond its native discovery capabilities using digital tracking. I presented a prelim-

inary study of constructing a grid in position angle and hourly motion to minimize computation needed using the Neptune Trojans as a test population.

Chapter III discussed the first notable TNO discovery made by DES, 2014 UZ_{224} (also known as "DeeDee"). 2014 UZ_{224} was discovered at a heliocentric distance of 92.5 au and an r-band magnitude of 23.0, which when assuming an albedo in the range 4-20% (roughly typical for TNOs) yielded a diameter estimate of $\sim 600 - 1300$ km. We conducted follow-up observations using ALMA to obtain flux measurements at infrared wavelengths so that we could break the degeneracy between size and albedo. I conducted the thermal analysis using our visual and infrared measurements of 2014 UZ_{224}, examining a variety of viable thermal models for the temperature distribution on the surface. Differences in the models arose due to uncertainty in the object's rotation and surface roughness. I calculated the size of 2014 UZ_{224} to be $D = 635^{+57}_{-61}(\text{stat})^{+32}_{-39}(\text{sys})$ km and its albedo to be $p_V = 13.1^{+3.3}_{-2.4}(\text{stat})^{+2.0}_{-1.4}(\text{sys})$. This makes 2014 UZ_{224} a likely rock-ice mix and likely large enough to be in hydrostatic equilibrium, qualifying it as a candidate dwarf planet.

In Chapter IV I described the DES Survey Simulator. A survey simulator is a crucial component of any Solar System survey because it allows the biases of a survey to be characterized and thus allows for the study of the true underlying distributions of objects detected by the survey. I described the method by which I calculate the limiting magnitudes of DES exposures using synthetic objects embedded by the `DiffImg` pipeline. I described the algorithm by which I determine whether a synthetic TNO would have been detected by DES, and I detailed applications of the survey simulator thus far. It has been used to characterize 2015 BP_{519}, a new ETNO with an inclination $i = 54.1°$; 2016 QV_{89} and 2016 QU_{89}, two new distant TNOs with similar orbital elements; and new Neptune trojans, and most notably the first ultra-red Neptune Trojan, 2013 VX_{30}. Using our new Neptune Trojans, the simulator was further used to estimate the size of the L4 Trojan population and the ratio of blue-to-red Neptune

Trojans. Finally, I used the simulator to characterize the 14 Plutinos detected by DES. The a, i, H distributions of Volk et al. (2016) provide a reasonable match to our data, but discrepancy between the simulated and observed e distributions (possibly due to dependence on the heliocentric distance of discovery) still warrants further investigation.

Chapter V explored the application of the DES Survey Simulator to the TNOs with $a > 250$ au and $q > 30$ au – the "extreme" TNOs. Trujillo & Sheppard (2014) first noted an apparent clustering in the arguments of perihelion of these objects and posited that a massive, exterior planet could force the apparent alignment. Batygin & Brown (2016) and Batygin et al. (2019) noted an additional clustering in the longitudes of ascending node (and consequently the longitudes of perihelion) of the ETNOs, which gave rise to the Planet Nine hypothesis. Studies examining the effects of observational bias on the apparent clustering have reached directly oppositional conclusions (Brown, 2017; Shankman et al., 2017; Brown & Batygin, 2019). The DES sample of ETNOs represents an independent and self-contained sample, separate from previous studies. I found that observational bias can explain the apparent orbital clustering of the DES ETNOs, but I noted that the DES selection function peaks where the orbital clustering is expected to occur. Because the DES sample is small with $N = 4$ and the DES selection function peaks near the expected orbital clustering, I concluded that DES has limited power to distinguish between the null hypothesis and that predicted by Planet Nine.

6.2 Future Outlook

The Kuiper Belt offers a unique probe of the dynamical history of the Solar System's giant planets and environmental conditions during the Solar System's formation. The landscape of the Kuiper Belt has changed dramatically since Jewitt & Luu (1992) discovered 1992 QB_1. Now, after just under 30 years of exploration, we

are starting to understand the Kuiper Belt. Dedicated TNO surveys have revealed intricate structure in every TNO dynamical class, from the cold classical KBOs to resonant object to the scattered disk and detached objects.

Future work with DES will probe the high-inclination regions of the Solar System and add to the census of known TNOs. New high-inclination discoveries, combined with the Survey Simulator described in this thesis, will inform models of Neptune migration. In particular, recent studies have suggested the existence of a dynamically "warm" component of the cold classical Kuiper Belt (Gladman et al., 2018). This is separate from the "kernel" and "stirred" components, also in the cold classical Kuiper Belt. The warm component is posited to have a mean inclination around $i = 4 - 7°$, placing a potential probe of this population well within the reach of DES. Further studies of higher inclination populations will help elucidate the nature of Neptune's migration through the Kuiper Belt – specifically, the inclination distribution of TNOs is sensitive to the migration timescales of Neptune before and after a discontinous change in its semimajor axis, referred to as "grainy" migration. The wide inclination distributions of the dynamically excited Kuiper Belt populations suggest that some dynamical process excited these populations to inclinations in excess of 10°. Current Kuiper Belt constraints suggest that Neptune's migration was slow in addition to grainy, because a fast migration time does not allow enough time for orbits to become sufficiently excited through encounters with Neptune (Nesvorný, 2015). The study further suggests that the doubly-sloped inclination distribution of hot classical Kuiper Belt objects observed by the CFEPS survey lends weight to the two-stage migration model of Neptune suggested by Nesvorný & Morbidelli (2012). However, CFEPS focused primarily near the ecliptic plane. DES's extended inclination coverage promises to glean new insights from the high-inclination populations and provide stricter constraints on the nature of Neptune's migration through the Kuiper Belt.

Perhaps one of the largest untapped potentials of DES at the present time is the

color information it provides about discovered objects. The survey strategy of DES automatically yields information about detected Solar System objects in four colors, *griz*, and while the survey cadence does not allow us to quantify potential effects of a rotational lightcurve on the observed colors, we still obtain mean color information essentially for free. Together with the Survey Simulator, which has already been shown to be effective in debiasing populations of Neptune Trojans with different colors (Lin et al., 2019), DES will measure the colors of hundreds of TNOs. Correlations or relationships between object colors and their dynamical properties will constrain where these objects formed in the planetesimal disk and how, or if, they have migrated from their formation locations.

Analysis has begun on the new and superior transient catalog developed by our colleagues at the University of Pennsylvania. We expect to more than double the number of TNOs detected by DES using this transient catalog, due to its superior depth and survey coverage (especially at high ecliptic latitudes). Perhaps there are new ETNOs hiding in the improved transient catalog, which will further inform the Planet Nine hypothesis. Of course, there were surely be new and exciting discoveries, whicht nearly always come from a massive new dataset that probes a parameter space not previously well-studied.

With the Survey Simulator described in this thesis, future researchers will be able to extract new and enlightening information about the structure and composition of the Kuiper Belt, which will lead to improved constraints of the nature of the giant planets' migration in the early few hundred million years of the Solar System's history. Insight gleaned from the Dark Energy Survey will inform future analyses of new detections, such as what will surely come from the Large Synoptic Survey Telescope starting in 2023.

It has been an exciting time to study the trans-Neptunian Solar System. The discoveries in the past 30 years, or even the past five, have proven that we have much

to learn still about our own cosmic backyard. This thesis adds a drop to the cosmic ocean of knowledge and I look forward to the discoveries that are sure to come.

APPENDICES

APPENDIX A

Installing and Running the DES Survey Simulator

In this dissertation, we construct a survey simulator for the Dark Energy Survey to enable detailed population studies of the outer Solar System. Given an exposure list containing date and time of exposure midpoint, location, and limiting magnitude of the exposure, the survey simulator determines which objects in a given outer Solar System population model would have been detected by DES. Further details are available in Chapter IV.

A.1 Installation

In this appendix, we provide the survey simulator for use by the community, as the procedure should be agnostic to the particular survey described by the exposure list. The code is currently available at:

`https://github.com/sjhamil/DES_SurveySimulator`

The repository is currently a collection of Python scripts. A `requirements.txt` file specifies necessary dependencies. The survey simulator was developed using Python 3.5. It is not compatible with Python 2.x, but should work with Python

3.x. Clone the repository and switch to the `devel` branch by executing the following commands:

```
$ git clone https://github.com/sjhamil/DES_SurveySimulator.git
$ git fetch && git checkout devel
```

Finally, install the necessary dependencies by navigating to the survey simulator directory and executing

```
$ pip install -r requirements.txt
```

The packages and tools required by the simulator are listed in `requirements.txt` and displayed here:

```
1  argparse
2  easyaccess
3  ephem
4  itsample
5  logging
6  matplotlib
7  numba
8  numpy
9  pandas
10 pickle
11 pyyaml
12 scipy
13 shutil
14 time
```

The simulator additionally requires Hsing Wen Lin's `propagate` package, found at https://github.com/sevenlin123/propagate. Clone this repository to a location of your choice and add the path to the `PYTHONPATH` environment variable in your `.bashrc`, `.bash_profile`, or `.zshrc` file.

A.2 Repository Contents

The survey simulator code lives under the `SurveySimulator/` directory in the main repository. The directory contains the following files:

- `README.md` – contains the information in this appendix and additional details.
- `simulator.py` – the main driver of the simulator. Command line arguments include:

  - `--calclim` – Tell the Survey Simulator to recalculate exposure limiting magnitudes.
  - `--genobjects N` – Tell the Survey Simulator to generate N objects. If using the clone mode of operation, this will generate N clones of each object. If using the `orbit_info` mode of operation, this will generate (at minimum) N objects in total. This option is ignored if using `ss_model_object_file`.
  - `--search` – Tell the Survey Simulator to search through the generated/supplied objects and calculate the RA,DEC of each object for each wide survey difference imaging exposure. It then determines whether that RA,DEC falls on a DECam CCD, and if so keeps that observation.
  - `--magcuts` – Tell the Survey Simulator to subject the list of observations from the `--search` step to the limiting magnitudes of each exposure. Observations that are too faint will be removed from the final list.
  - `--qaplots` – Produces quality assurance plots (*Note: currently deprecated*).

- `configs/config_example.yaml` – the example configuration file for the simulator run. Any user-created configuration files should follow this format.
- `generate_objects.py` – the Python script used for generating new objects according to an input model in the config file
- `simtools.py` – functions useful for running the simulator
- `utils.py` – utility functions that are more generally applicable than those in `simtools.py`.

In addition, there are DES-specific files included:

- `sn_status.txt` – contains 50% limiting magnitude and SNR of the mag20 supernova fakes, needed to estimate the limiting magnitudes of `wsdiff` exposures from the DES supernova fields.

- `ccdBounds.py` – contains the chip boundaries of the 62 CCDs in the Dark Energy Camera as measured from the center of the focal plane.

Miscellaneous Files

The following scripts may also be useful for DES members wishing to use the Survey Simulator.

- `fakes/fetch_mag20_fakes.py` – get the mag20 fakes for desired DES year and `wsdiff` season. You will need access to the `destest` database. Command line arguments include:

  - `-s, --season` – the `wsdiff` season to pull. Pass `all` to pull all seasons.
  - `-y, --year` – the DES year to pull. Pass `all` to pull all years.
  - `-t, --topdir` – the top-level directory to save returned fakes to
  - `-k, --kind` – the type of fake to pull (options are `mag20`, `tno`, or `sn`)
  - `--force` (optional) – if specified, pull fakes even if they have already been pulled and saved to `topdir`. Overwrites any data in `topdir`.

- `SurveySimulator/exposure_files/fetch_and_clean_exposures.py` – fetch the exposure numbers and associated information (RA, DEC, date and time of observation, etc) that will ultimately be used for the simulator. You will need access to the `destest` database. Command line arguments include:

  - `-y, --year` – The DES year for which to get/clean exposures. Default is `all` (SV-Y5).

– `--fetch` (optional) – if included, will fetch the exposure information for the DES year specified in `--year`. Saves a temporary file with the information.

– `--clean` – Clean the exposures resulting from `--fetch`. Reads from the temporary file saved by `--fetch`. Operations performed by clean include: transforming MJDs to DJDs (for pyephem), filtering non-`wsdiff` exposures out, assigning a `wsdiff` season to each exposure, assigning a DES year, and assigning a field type (Shallow SN, Deep SN, or Wide).

– `-f, --exp-filename` – the file to save the cleaned exposure list to. Expects a .csv file.

A.3 The Configuration File

In this section, we describe the structure of the configuration file and viable options to specify.

Listing A.1: Example survey simulator configuration file as of 25 February 2019

```
# ‘base_dir‘ should be where the git repository was cloned
base_dir: /Users/sjhamilton/Research/DES/TNOanal/Debiasing/
output_dir: SurveySimulator/output/
run_tag: test/
exposure_file: SurveySimulator/exposure_files/exposures_ed_classified.csv

n_cpu: 4
log_level: DEBUG

# Specify object generation method
# ‘orbit_info‘ or ‘ss_model_object_file‘ must be present in the
# config file
#
# Uncomment one of the below blocks and enter desired parameters

#-- --- --- --- --- --- --- --- --- --- --- --- --- --- --- --- --- --- --- --- --  --
# Generate new objects from model
#-- --- --- --- --- --- --- --- --- --- --- --- --- --- --- --- --- --- --- --- --  --

orbit_info:
    a: power  # Type of distribution to generate
    a_params:
        amin: 150.0
        amax: 1000.0
        power: 0.5
    e: uniform  # Type of distribution to generate
    e_bounds:
        emin: 0.0
        emax: 1.0
    i: rayleigh
    i_params:  # Type of distribution to generate
        imin: 0.0
```

```
        imax: 180.0
        icenter: 0.0
        iwidth: 10.0
        unit: deg  # options are 'deg' or 'rad'
    H: single  # Type of distribution to generate. `single`, `knee`, and
               # `divot` supported
               # `uniform` also supported, but don't use that
    H_params:
        Hmin: 4.0
        Hmax: 9.0
        Hbreak: 7.0
        slope1: 0.9
        slope2: 0.2
        contrast: 1.0
        # If contrast==1 --> knee distribution
        # If contrast==1 and slope1==slope2 --> single slope distribution

    # Only `uniform` is supported for om, Om, M
    om: uniform
    om_params:
        ommin: 0.0
        ommax: 360.0
        unit: deg  #options are 'deg' or 'rad'
    Om: uniform
    Om_params:
        Ommin: 0.0
        Ommax: 360.0
        unit: deg  #options are 'deg' or 'rad'
    M: uniform
    M_params:
        Mmin: 0.0
        Mmax: 360.0
        unit: deg  #options are 'deg' or 'rad'


#-- --- --- --- --- --- --- --- --- --- --- --- --- --- --- --- --- --- --- --  --
# Read objects from previously generated model
#-- --- --- --- --- --- --- --- --- --- --- --- --- --- --- --- --- --- --- --  --

#ss_model_object_file: ../solarsystem_models/CFEPS_L7/L7SyntheticModel_v09_res.csv


################################################################
# DES-specific
################################################################

# Calculating limiting magnitudes
# model_dir is the directory in which the SN mag20 are saved. These are used
# to calculate limiting magnitudes. For now, I've provided my latest limiting
# magnitude file, so you don't need to worry about this
# fake_type refers to the type of fake object to use for calculating limiting
# magnitudes

model_dir: /Users/sjhamilton/Downloads/SNfakes/
fake_type: mag20

# mode specifies whether to use the wsdiff exposures or all des exposures
# options are 'wsdiff' or 'fullsurvey'
mode: fullsurvey

# Years refers to DES observing years (SV-Y5)
# Seasons refers to wide survey DiffImg processing campaigns
years:
    - all
seasons:
    - all
```

Setting Up the Simulator Run

Lines 1-8 in the configuration file (Listing A.1) set up the overall simulator run information.

- `base_dir` (l. 2)– specifies the location of the cloned git repository. This setting tells the simulator where to find files needed for execution.
- `output_dir` (l. 3) – specifies the location of the base output directory. If a relative path is specified, the path appends to the location of the `simulator.py` script.
- `run_tag` (l. 4) – specifies the subdirectory under `output_dir` into which the data of the current simulator run will be written. The subdirectory is created if it does not yet exist.
- `exposure_file` (l. 5) – specifies the location of the exposure file to use for the simulator run. The exposure file must contain the columns:
  - `expnum` – the exposure number or identifier
  - `band` – the bandpass filter used for the exposure
  - `ra, dec` – the on-sky coordinates of the exposure
  - `date` – the Julian date of the midpoint of the exposure
- `n_cpu` (l. 7) – specifies the number of CPUs to use for the simulator run.
- `log_level` (l. 8) – the python logging level to use.

Specifying the Orbital Population to Simulate

Lines 16-72 in the configuration file determine the fake solar system objects that will be used in the simulator run. The simulator can either generate new objects according to a model specified in the `orbit_info` block, or it can read

in a file of previously-generated objects, specified by `ss_model_object_file` on Line 72. If both the `orbit_info` block and `ss_model_object_file` are uncommented, `ss_model_object_file` will take priority.

We now describe the `orbit_info` block starting on Line 20 in more detail. Each orbital element is specified by giving a distribution type and associated parameters defining the distribution. The general structure is

```
orbit_info:
    <element> : distribution_name
    <element>_params:
        <parameter list here>
```

Each orbital element may have different viable distributions and parameter lists, so we now describe each element separately.

- Semimajor axis, a – supported distributions are `power` (where the distribution is $\propto a^x$ and x is specified by the `power` parameter, described below) or `uniform`. The parameters to specifiy for a are
  - `amin` – the minimum value for a in AU
  - `amax` – the maximum value for a in AU
  - `power` – the power law index. This option is ignored if generating a `uniform` distribution.
- Eccentricity, e – Currently, the only supported distribution for e is `uniform`. However, while generating objects e is constrained such that the perihelion distance q satisfies $30 < q < 200$ AU. In the future, this constraint will be specified in the configuration file.
- Inclination, i – supported distributions are `uniform`, `rayleigh` ($\propto i \cdot e^{-i^2/(2\sigma_i^2)}$), and `brown` ($\propto \sin i \cdot e^{-(i-i_c)^2/(2\sigma_i^2)}$). The parameters to specify for i are

  - `imin` – the minimum value allowed for i
  - `imax` – the maximum value allowed for i
  - `icenter` – the central value of the distribution, used only when generating a `brown` distribution.
  - `iwidth` – the width of the distribution, used only when generating a `rayleigh` or `brown` distribution.
  - `unit` – the units of the previous four parameters (options are `rad` or `deg`).

- Argument of perihelion, ω (denoted by `om` in the configuration file) – currently, the only supported distribution is `uniform`. The parameters to specify for ω are
  - `ommin` – the minimum value allowed for ω
  - `ommax` – the maximum value allowed for ω
  - `unit` – the units of the previous two parameters (options are `rad` or `deg`).

- Longitude of ascending node, Ω (denoted by `Om` in the configuration file) – currently, the only supported distribution is `uniform`. The available parameters for Ω are similar to those for ω.

- Mean anomaly, M – currently, the only supported distribution is `uniform`. The available parameters for M are similar to those for ω and Ω.

- Absolute magnitude, H – Supported distributions are:
  - `single`, a single slope distribution in which $\frac{dN}{dH} \propto 10^{\alpha H}$ and α is the slope.
  - `knee`, a distribution comprised of bright-end and faint-end components in which

$$P(H)dH \propto \begin{cases} 10^{\alpha_1 H} dH, & H \leq H_{break} \\ 10^{\alpha_2 H} dH, & H > H_{break} \end{cases}$$

where α_1 and α_2 are the bright- and faint-end slopes, respectively.

- `divot`, similar to `knee` except that at H_{break} there is an additional discontinuity in the distribution.

$$P(H)dH \propto \begin{cases} c10^{(\alpha_2-\alpha_1)H_{break}}10^{\alpha_1 H}dH, & H \leq H_{break} \\ 10^{\alpha_2 H}dH, & H > H_{break} \end{cases}$$

where c is called the "contrast" and describes the size of the step discontinuity in the differential H distribution.

A depiction of these three distributions can be seen in Figure A.1. The parameters to specify for H are

- `Hmin` – the minimum allowed value for H
- `Hmax` – the maximum allowed value for H
- `Hbreak` – the absolute magnitude at which the distribution transitions from the bright-end distribution to the faint-end distribution
- `slope1` – the bright-end slope of the H distribution
- `slope2` – the faint-end slope of the H distribution
- `contrast` – Used only in `divot`. It is the ratio between the differential number of objects on the bright side of the divot to that on the faint side. The divot is located at `Hbreak`.

Note that if the `divot` distribution is specified but `contrast`==1, this is equivalent to `knee`. Alternatively, if the `divot` distribution is specified but `contrast`==1 and `slope1`==`slope2`, this is equivalent to `single`.

The survey simulator currently does not internally include the capability to generate resonant populations (e.g. Neptune Trojans, Plutinos, twotinos, etc). We recom-

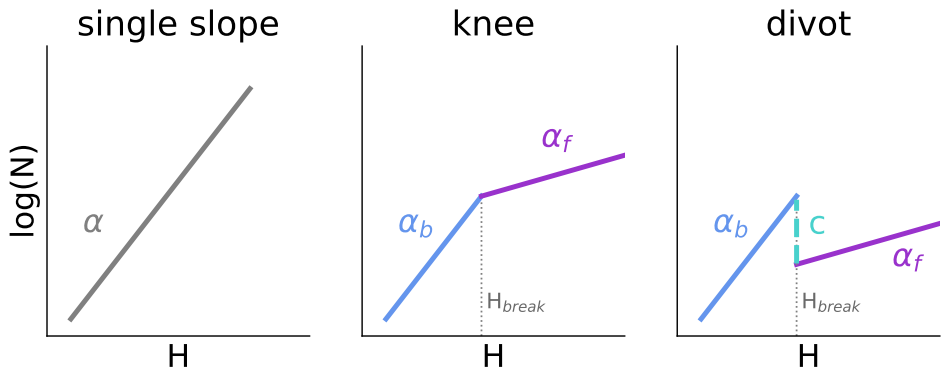

Figure A.1: A depiction of the three absolute magnitude distributions supported by the DES survey simulator. The single slope distribution is parameterized in log space by a slope α. The knee distribution is described by a two-sloped distribution where α_b parametrizes the bright end of the distribution and changes to the faint-end slope α_f at the break magnitude, H_{break}. The divot distribution is similar to the knee distribution but with a discontinuity at H_{break} described by the contrast c.

mend generating resonant objects separately and using the `ss_model_object_file` option.

DES-Specific Configuration Options

Lines 75-98 are configuration parameters for DES-specific runs of the simulator.

- `model_dir` (l. 66) – the path to the mag20 fake observations from difference imaging. This is only used if the simulator is recalculating DES exposure limiting magnitudes.

- `fake_type` – the type of fake object to be used to calculate DES limiting magnitudes (mag20, TNO, or SN). The TNO fakes are generally not distributed densely enough to be used to calculate limiting magnitudes, so it is recommended to leave this parameter set to `mag20` for now. `fake_type` is only used if the simulator is recalculating DES exposure limiting magnitudes.

- `mode` – the DES survey simulator currently operates in two modes: `wsdiff`,

which evaluates object detectability only for the DES wide survey exposures that have been processed through difference imaging, and `fullsurvey`, which does not restrict the exposure list to `wsdiff`-only exposures.

- `years` – the DES years to consider in the simulator run (options are SV, Y1, Y2, Y3, Y4, Y5, Y6, or `all`)
- `seasons` – the `wsdiff` seasons to consider in the simulator run. Options are 118 through 121, 198, 199, 240 through 242, 250 through 252, 301, and 302. Alternatively, the user may specify `all`.

A.4 Survey Simulator Execution and Output

The survey simulator is run using the script `simulator.py`. Executing `$ python simulator.py -h` yields the help message below:

```
$ python simulator.py -h

usage: simulator.py [-h] [--calclim] [--genobjects GENOBJECTS] [--search]
                    [--magcuts] [--qaplots] -c CONFIG

optional arguments:
  -h, --help            show this help message and exit
  --calclim             Calculates exposure-by-exposure magnitude limits in
                        g,r,i,z.
  --genobjects GENOBJECTS
                        Generates *at least* GENOBJECTS fake objects/orbital
                        elements from input elements or distributions
  --search              Figure out which exposures/CCDs an object would have
                        fallen in during DES.
  --magcuts             Decides whether we would have made an individual
                        detection on the object.
  --qaplots             Returns a histogram of the angular orbital elements
                        that we detect.
  -c CONFIG, --config CONFIG
                        Path to the YAML config file containing run info.
```

The `--calclim` option currently is DES-specific. In general, this should not need to be used unless the exposure file specified in the configuration file has changed (e.g. new exposures have been added). Further, the `--genobjects` option is not necessary unless objects are being generated by a population model described by the `orbit_info` block in the configuration file. Finally, the `--qaplots` is still included but is currently deprecated.

We now describe the basic flow of the simulator. For this, we assume that all command line flags have been passed to the program (excluding the deprecated `--qaplots`).

1. If `--calclim` has been passed, the exposure limiting magnitudes are recalculated following the procedure outlined in Chapter IV.

2. The `--genobjects GENOBJECTS` is the next command to be processed, only if the `ss_model_object_file` is not uncommented in the configuration file. If `ss_model_object_file` is specified, then the `--genobjects` option is ignored. This option generates `GENOBJECTS` objects following the population model described in the `orbit_info` block in the configuration file.

3. The simulator then processes the `--search` option. This option tells the simulator to project the on-sky positions of the synthetic objects to the approximate midpoint of the exposure list (for DES, this is August 15, 2016). The simulator then keeps only those objects that lie within 7° of at least one survey exposure.

4. The final step of the simulator is the `--magcuts` option. This option tells the simulator to subject the output of the previous step to the exposure limiting magnitudes. Whether an observation of an object is kept is determined by drawing a random number from 0.0 to 1.0 and evaluating whether the random number fell below the magnitude efficiency curve for that specific exposure and observation magnitude, given by a hyperbolic tangent function defined by the 50% limiting magnitude and the width of the function turnover. Functionally this looks like:

    - **Keep** the observation if $x \leq 0.5A\left(1 - \tanh\left(\frac{m_{50} - m_{obs}}{w}\right)\right)$
    - **Reject** the observation $x > 0.5A\left(1 - \tanh\left(\frac{m_{50} - m_{obs}}{w}\right)\right)$

where x is the random number, m_{50} is the 50% limiting magnitude, m_{obs} is the magnitude of the specific observation being considered, and w is the width of the hyperbolic tangent function.

The simulator writes data into three subdirectories:

- `orbits` – contains the synthetic objects. If using a previously generated population of objects, the file will be symbolically linked into this directory.
- `insurvey` – contains the output of the `--search` step. These are the objects that fell in at least one survey exposure.
- `found` – contains the output of the `--magcuts` step. These are the objects that would have had detections in the survey after being subject to the limiting magnitudes of each exposure.

The final step of determining which detections would have been linked into objects remains up to the user. The data in `found` essentially comprises a transient catalog that can be processed in the same way the user would process a real transient catalog.

APPENDIX B

Full List of TNOs Detected by the Dark Energy Survey

Table B.1: Barycentric osculating orbital elements of 341 TNOs detected by DES. Dynamical classifications are as outlined in Chapter II

cen = Centaur, cb = Classical Belt, sdo = Scattered Disk, det = Detached, p:q = Object in p:q Resonance, etno = ETNO

MPC	DES	a (au)	e	i (°)	q (au)	ω (°)	Ω (°)	r (au)	H_r	T_{peri} (JD)	Epoch (JD)	N_{obs}	Arc (days)	Class
2015 VT152	2015 VT152	19.34	0.18	39.76	15.84	48.3	137.89	22.55	9.5	2470438.5	2457340.5	8	24	–
K03QB2C	ws301g428	20.5	0.28	18.24	14.84	22.19	158.66	26.09	8.5	2472416.6	2456578.73	19	1436	cen
2016 QF86	2016 QF86	21.13	0.31	13.63	14.6	227.31	274.83	27.46	8.4	2473548.5	2458600.5	46	1206	–
2013 RG98	2013 RG98	23.11	0.17	46.04	19.24	351.46	145.8	22.8	9.0	2465071.5	2458600.5	101	834	–
2014 SB349	2014 SB349	25.79	0.18	15.53	21.25	359.54	117.08	24.48	9.3	2465347.5	2458600.5	29	832	–
2014 VR39	2014 VR39	27.62	0.27	32.74	20.19	245.29	181.81	20.79	10.5	2459472.5	2456980.5	9	41	–
2014 QP441	2014 QP441	29.96	0.06	19.42	28.05	4.6	96.47	29.24	9.3	2467576.5	2458200.5	114	1219	–
2014 UU240	2014 UU240	29.96	0.05	35.8	28.48	76.44	81.91	nan	8.3	2477911.5	2458200.5	13	755	–
2013 VX30	2013 VX30	29.98	0.08	31.31	27.56	215.19	192.58	nan	8.3	2458565.5	2458200.5	60	1567	–
2014 QO441	2014 QO441	30.03	0.11	18.85	26.79	115.72	106.86	33.16	8.3	2429448.5	2458600.5	183	798	–
K14UO0U	ws13g10	30.04	0.04	35.75	28.78	79.97	81.99	30.89	7.8	2478735.0	2456959.83	15	1126	1:1
K13V30X	ws302g99	30.09	0.08	31.26	27.57	215.49	192.54	27.64	8.1	2458602.1	2456567.79	74	1566	1:1
K11SR7O	ws302g126	30.16	0.01	9.64	29.8	117.75	113.53	30.47	7.3	2431681.9	2456545.88	22	1527	1:1
U9239	ws302g71	30.24	0.3	36.1	21.15	96.1	187.04	28.4	6.4	2446185.4	2456547.85	27	1527	cen
	ws301g225	32.38	0.08	11.12	29.75	332.67	16.69	29.81	7.9	2454428.9	2456537.77	25	1485	cen
K14UM5C	ws302g116	34.77	0.1	4.94	31.41	242.78	139.63	31.41	7.3	2457030.3	2456951.73	9	37	sdo
	ws200g542	36.38	0.07	14.82	33.74	288.51	204.39	38.92	7.1	2492843.7	2456543.59	11	1504	3:4
	ws302g151	36.4	0.15	14.54	30.9	335.9	70.52	31.37	7.6	2461063.3	2456547.89	18	1525	3:4
	ws302g68	36.49	0.19	17.56	29.68	263.29	161.14	31.11	7.8	2463553.5	2456569.69	28	1510	3:4
	ws200g468	36.73	0.18	7.8	30.09	328.2	265.19	38.32	6.3	2435363.5	2456548.69	6	27	sdo
	ws301g658	37.9	0.05	19.38	35.9	83.08	180.23	38.12	7.0	2434471.5	2456565.66	13	1458	cb

Continued on next page

MPC	DES	a (au)	e	i (°)	q (au)	ω (°)	Ω (°)	r (au)	H_r	T_{peri} (JD)	Epoch (JD)	N_{obs}	Arc (days)	Class
	ws301g203	38.24	0.09	22.72	34.78	59.73	22.68	36.87	6.8	2471364.7	2456537.86	23	1172	cb
	ws240g1	38.24	0.12	27.6	33.56	244.64	8.01	34.91	7.2	2447409.3	2456904.6	18	1135	cb
2015 QT11	2015 QT11	38.45	0.05	26.64	36.56	15.42	72.27	37.43	8.7	2470606.5	2458200.5	43	859	–
	ws200g333	38.71	0.35	17.29	25.14	35.87	183.48	45.08	5.3	2432061.2	2456543.67	10	1124	cen
C0348	ws13g6	38.86	0.07	24.84	36.21	357.96	140.5	39.23	4.0	2480015.8	2456904.85	15	456	cb
	ws13g5	38.96	0.13	38.39	33.88	300.12	169.46	36.15	7.3	2469327.4	2456958.85	7	842	cb
K03Q91B	ws301g1183	39.24	0.19	6.5	31.62	80.59	136.78	45.72	6.4	2421082.9	2456578.71	15	1436	2:3
	ws302g227	39.3	0.19	22.44	31.7	259.96	88.49	33.6	7.0	2447812.0	2456328.59	21	368	2:3
	ws302g158	39.35	0.22	9.85	30.71	257.86	145.23	31.08	7.3	2459848.5	2456564.83	24	1508	2:3
	ws302g61	39.36	0.15	11.6	33.33	75.62	146.69	45.07	5.7	2416814.3	2456564.84	30	1514	2:3
2013 RD98	2013 RD98	39.37	0.24	19.54	30.07	104.91	144.77	45.66	7.5	2425872.5	2458600.5	145	818	–
k9372	ws301g1077	39.38	0.11	22.35	35.0	42.23	164.18	43.27	5.1	2419001.8	2456537.84	24	1515	2:3
	ws302g214	39.38	0.29	19.01	27.95	275.14	173.62	30.96	7.9	2464097.6	2456247.62	30	1832	2:3
(491767) 2012 VU113	(491767) 2012 VU113	39.39	0.08	30.19	36.42	312.71	65.45	36.46	7.7	2453401.5	2458600.5	36	2896	–
	ws302g485	39.39	0.28	10.37	28.34	285.48	129.49	29.29	8.1	2460932.1	2456569.7	25	1479	2:3
	ws302g198	39.39	0.28	10.37	28.34	285.48	129.49	29.29	8.1	2460932.2	2456569.7	25	1479	2:3
K12TW4D	ws301g208	39.39	0.14	9.58	33.93	190.99	114.62	36.34	6.7	2444151.1	2456544.82	24	1448	2:3
	ws302g5	39.4	0.24	24.95	29.83	247.63	58.81	34.54	6.9	2444664.7	2456569.72	32	1510	2:3
	ws302g53	39.41	0.25	16.61	29.61	329.34	68.27	30.1	7.5	2459992.1	2456545.8	21	1175	2:3
o4555	ws302g101	39.41	0.24	18.8	29.85	172.77	158.75	32.54	6.0	2447941.9	2456569.77	29	1532	2:3
K14SY9K	ws302g258	39.41	0.29	9.4	28.02	314.67	59.87	28.11	7.4	2455636.4	2456932.79	13	56	cen
	ws302g149	39.42	0.28	43.51	28.41	318.84	32.82	29.03	7.9	2453027.9	2456544.84	15	787	2:3
	ws301g572	39.42	0.18	14.55	32.18	237.41	173.64	33.65	7.7	2464292.0	2456578.64	18	1436	cb
2014 QM441	2014 QM441	39.43	0.28	18.29	28.52	312.62	95.96	28.68	8.5	2458616.5	2458600.5	66	506	–
K14SY9K	ws302g117	39.47	0.29	9.4	28.03	315.9	59.9	28.07	7.4	2455802.6	2456569.69	19	419	2:3
	ws301g997	39.48	0.28	5.22	28.41	248.8	139.57	28.58	7.6	2458364.4	2456537.86	27	1152	2:3

Continued on next page

MPC	DES	a (au)	e	i (°)	q (au)	ω (°)	Ω (°)	r (au)	H_r	T_{peri} (JD)	Epoch (JD)	N_{obs}	Arc (days)	Class
	ws301g999	39.63	0.21	14.74	31.44	215.9	29.36	44.02	6.6	2428499.9	2456932.77	7	43	sdo
	ws121g1	39.72	0.05	54.78	37.71	254.92	206.51	37.71	6.7	2456981.4	2457014.83	10	54	cb
	ws15g0	39.79	0.06	44.56	37.34	256.23	146.81	37.68	7.0	2449720.4	2456992.8	12	433	cb
(505412) 2013 QO95	(505412) 2013 QO95	39.86	0.03	20.64	38.66	312.95	82.99	38.68	6.7	2458436.5	2458600.5	67	1214	–
2014 VT37	2014 VT37	39.95	0.26	33.46	29.44	175.63	197.67	30.41	9.0	2452238.5	2457000.5	15	60	–
o5412	ws302g94	39.97	0.03	20.6	38.66	316.07	83.11	38.68	6.4	2459211.9	2456534.7	57	1561	cb
2015 RS245	2015 RS245	40.18	0.09	16.34	36.76	247.29	141.18	36.8	8.2	2455246.5	2458200.5	20	836	–
	ws200g373	40.19	0.2	14.18	32.09	69.56	193.6	36.34	7.2	2443255.1	2456545.56	17	1478	sdo
	ws301g227	40.21	0.11	23.15	35.86	223.97	175.86	36.61	7.3	2464479.5	2456537.77	21	1510	cb
	ws301ag186	40.22	0.12	1.76	35.35	109.17	54.62	44.75	6.3	2497054.4	2456604.64	6	1122	cb
2016 PA101	2016 PA101	40.23	0.09	20.5	36.75	351.21	91.3	38.0	8.2	2469539.5	2458600.5	51	515	–
	ws301g1175	40.25	0.1	24.2	36.07	211.58	32.68	42.19	6.6	2427476.0	2456545.83	11	815	cb
	ws240g3	40.3	0.09	22.55	36.82	233.54	43.5	37.21	6.3	2450363.2	2456877.66	10	71	cb
	ws200g407	40.34	0.06	14.6	38.04	98.45	268.66	38.5	7.0	2465595.1	2456538.7	9	1832	cb
	ws200g743	40.35	0.07	18.2	37.47	154.7	188.99	37.48	7.2	2455913.6	2456546.74	12	1150	cb
2014 TT85	2014 TT85	40.41	0.08	17.86	37.35	264.25	98.12	37.81	8.1	2449003.5	2458600.5	34	847	–
K14T86F	ws241g3	40.42	0.08	32.05	37.26	106.21	65.08	43.0	6.4	2419912.6	2456931.58	20	1142	cb
2013 QP95	2013 QP95	40.5	0.17	25.49	33.78	19.05	71.3	36.63	7.2	2469065.5	2458600.5	150	530	–
	ws241g4	40.5	0.11	38.46	36.08	307.28	87.57	38.99	6.3	2473667.5	2456903.64	6	752	cb
K13Q95P	ws302g150	40.64	0.17	25.44	33.76	18.8	71.4	36.74	7.0	2469004.3	2456534.7	180	1561	cb
D9775	ws301g937	40.79	0.24	6.44	31.19	242.57	162.19	31.74	6.4	2460889.7	2456953.75	11	25	sdo
2014 TF86	2014 TF86	40.83	0.11	32.03	36.42	128.89	64.96	42.99	6.6	2426772.5	2458600.5	10	380	–
	ws200g658	40.84	0.28	27.98	29.62	193.54	175.65	30.94	7.0	2462027.6	2456545.56	8	1151	cen
2013 TH159	2013 TH159	40.88	0.1	33.68	36.91	233.21	62.35	40.68	8.6	2435011.5	2458600.5	17	433	–
	ws302g0	40.89	0.07	14.79	38.17	174.33	142.99	39.68	6.7	2440689.7	2456654.61	21	1426	cb
	ws242g7	40.96	0.04	32.37	39.21	255.28	50.97	39.29	7.0	2452119.9	2456559.57	6	1128	cb

Continued on next page

MPC	DES	a (au)	e	i (°)	q (au)	ω (°)	Ω (°)	r (au)	H_r	T_{peri} (JD)	Epoch (JD)	N_{obs}	Arc (days)	Class
2014 QU441	2014 QU441	41.14	0.1	19.35	36.88	297.24	113.03	37.15	7.9	2461614.5	2458600.5	30	469	–
2014 QE442	2014 QE442	41.15	0.04	26.41	39.37	251.41	77.68	40.39	7.1	2440295.5	2458600.5	36	894	–
E5452	ws200g166	41.51	0.02	19.27	40.58	172.29	186.99	40.65	3.2	2462592.3	2456543.64	21	1153	cb
	ws302g104	41.51	0.16	26.75	34.9	18.15	191.57	48.04	6.4	2411023.9	2456951.76	13	1041	8:13
	ws200g84	41.55	0.07	15.19	38.63	314.95	347.08	39.65	6.6	2445123.1	2457661.59	11	711	cb
2015 PL312	2015 PL312	41.73	0.13	26.18	36.28	4.35	71.67	37.35	8.5	2465997.5	2458600.5	21	439	–
2014 VW37	2014 VW37	41.93	0.13	48.81	36.46	254.34	122.66	36.81	7.2	2452104.5	2458600.5	16	428	–
2013 RB98	2013 RB98	42.06	0.26	21.93	31.26	351.21	146.96	42.31	6.5	2477718.5	2458600.5	48	1147	–
K14V37W	ws120g1	42.08	0.13	48.78	36.5	255.5	122.78	36.81	6.8	2452368.2	2456973.85	30	1185	cb
o3883	ws301g931	42.25	0.25	2.67	31.59	249.44	156.78	32.74	7.4	2462201.9	2456544.7	12	816	3:5
K12TW4C	ws302g62	42.27	0.2	9.63	33.94	259.27	131.83	33.96	6.2	2457394.0	2456569.7	29	1479	3:5
	ws302g217	42.28	0.21	29.34	33.3	138.48	194.24	36.98	6.7	2443993.1	2456268.65	39	1840	3:5
2014 UB225	2014 UB225	42.29	0.17	3.47	35.06	154.27	104.86	44.76	6.2	2428087.5	2456960.5	7	21	–
K14L28O	ws200g366	42.3	0.05	25.64	40.0	86.72	287.28	40.75	4.9	2469228.8	2456536.64	10	27	sdo
	ws301g444	42.31	0.26	11.55	31.41	287.89	42.66	33.04	7.4	2449867.1	2456568.61	21	1446	3:5
	ws301g1089	42.33	0.05	12.49	40.22	68.63	40.64	42.65	6.7	2483387.7	2456619.64	18	1402	cb
	ws301g978	42.48	0.12	7.51	37.23	78.32	60.42	45.33	6.2	2489420.8	2456569.66	19	1451	cb
	ws301g962	42.52	0.16	11.0	35.62	85.35	6.04	40.68	6.7	2475006.1	2456578.59	12	398	sdo
	ws301g1160	42.54	0.16	32.31	35.92	17.89	20.94	36.7	7.2	2463279.8	2456545.84	16	1502	cb
K03SV7Q	ws301g1217	42.66	0.08	28.57	39.25	193.15	176.31	39.24	6.4	2456366.1	2456537.85	27	1482	cb
K13U15Q	ws301g401	42.77	0.11	27.34	37.94	15.82	189.13	47.54	6.0	2408766.6	2456932.79	21	1087	cb
	ws301g802	42.81	0.4	46.0	25.46	107.39	177.36	32.84	7.2	2447435.2	2457640.66	6	77	cen
K14SZ0N	ws12g9	42.82	0.19	32.06	34.73	258.55	171.68	35.98	7.1	2464446.9	2456925.78	26	1176	cb
	ws11g20	42.82	0.17	22.71	35.49	245.05	107.65	35.99	7.5	2451873.6	2456888.86	18	1238	cb
	ws301g132	42.86	0.06	9.72	40.09	243.56	144.86	40.4	6.3	2463839.9	2456537.84	32	1517	cb
	ws13g9	42.9	0.16	32.86	35.9	251.82	140.81	35.99	6.8	2454684.5	2456920.84	18	1205	cb

Continued on next page

MPC	DES	a (au)	e	i (°)	q (au)	ω (°)	Ω (°)	r (au)	H_r	T_{peri} (JD)	Epoch (JD)	N_{obs}	Arc (days)	Class
K01QT7O	ws301g143	42.93	0.04	1.14	41.37	316.53	143.31	43.06	6.2	2482977.1	2456543.69	27	1511	cb
K13R98P	ws200g8	42.93	0.13	13.29	37.28	177.83	216.32	40.09	6.8	2471724.2	2456538.7	20	1509	cb
G0256	ws301ag272	42.95	0.06	4.91	40.59	47.44	103.67	45.0	6.5	2498916.4	2456543.69	6	60	cb
G0256	ws301g1250	42.96	0.06	4.91	40.32	38.99	103.55	45.0	6.4	2496111.7	2456543.69	13	1496	cb
2014 SQ350	2014 SQ350	43.0	0.11	29.89	38.25	213.92	66.29	44.32	7.0	2428346.5	2458600.5	23	803	–
K03QB1Z	ws200g365	43.01	0.06	2.66	40.39	16.57	326.05	40.46	7.0	2453100.9	2456565.63	22	1499	cb
	ws301g1007	43.03	0.2	11.62	34.61	327.58	35.22	34.66	7.6	2455226.4	2456578.71	12	1119	cb
	ws200g449	43.07	0.01	7.99	42.75	201.2	200.57	42.88	6.6	2471977.5	2456565.62	17	1506	cb
	ws200g576	43.08	0.2	17.09	34.55	270.55	321.57	45.22	6.1	2429737.6	2456546.74	7	46	cb
2014 SN350	2014 SN350	43.09	0.21	32.04	33.84	268.45	171.64	35.99	7.7	2466079.5	2458600.5	9	404	–
2013 RP98	2013 RP98	43.12	0.13	13.3	37.35	176.46	216.2	40.09	7.0	2471401.5	2458600.5	12	1119	–
	ws301g267	43.12	0.04	3.04	41.24	8.7	8.06	41.27	6.1	2459397.1	2456543.69	31	1480	cb
c5201	ws302g84	43.16	0.07	12.41	40.0	102.39	140.65	45.61	6.1	2417297.1	2456931.84	16	1141	cb
2016 SS46	2016 SS46	43.3	0.38	15.07	26.65	319.11	142.62	31.13	8.7	2465900.5	2457660.5	13	35	–
	ws200g108	43.32	0.13	20.3	37.61	253.58	182.47	42.45	6.5	2477863.1	2456543.66	21	1522	cb
	ws200g25	43.32	0.15	6.24	36.97	116.4	283.68	39.13	6.8	2469868.5	2457614.77	7	451	cb
l1954	ws200g378	43.33	0.13	28.09	37.64	252.68	352.44	44.5	5.3	2429222.6	2456543.67	18	1528	cb
	ws301g1073	43.34	0.06	4.22	40.78	91.05	98.74	45.9	6.1	2507892.3	2456578.68	12	733	cb
(471954) 2013 RM98	(471954) 2013 RM98	43.39	0.13	28.08	37.57	253.5	352.43	44.5	5.4	2429492.5	2458600.5	78	2206	–
	ws301g2580	43.43	0.04	4.13	41.78	174.5	44.3	44.74	6.1	2415487.1	2456546.8	17	1476	cb
	ws301g1162	43.43	0.04	4.13	41.78	174.5	44.3	44.74	6.2	2415487.1	2456546.8	17	1476	cb
2012 YO9	2012 YO9	43.45	0.16	15.4	36.28	4.08	118.43	41.56	7.4	2475310.5	2458600.5	23	2271	–
	ws301g1091	43.48	0.18	7.42	35.49	151.44	66.34	49.66	5.8	2417624.1	2456563.62	19	1485	cb
	ws302g144	43.53	0.26	21.29	32.06	170.21	177.6	33.56	7.6	2450433.2	2456887.86	16	1185	4:7
	ws301g700	43.53	0.12	2.67	38.43	138.77	74.86	47.61	6.1	2416082.8	2456604.66	14	1450	cb
	ws302g82	43.54	0.09	10.01	39.46	281.87	117.11	39.57	6.9	2460081.3	2456568.79	18	1151	cb

Continued on next page

MPC	DES	a (au)	e	i (°)	q (au)	ω (°)	Ω (°)	r (au)	H_r	T_{peri} (JD)	Epoch (JD)	N_{obs}	Arc (days)	Class
	ws118g10	43.55	0.07	35.81	40.42	47.15	72.24	44.25	5.5	2485833.5	2457017.64	14	1110	cb
	ws302g146	43.56	0.19	10.6	35.36	307.04	100.92	35.8	7.4	2461404.0	2456931.84	14	1083	4:7
B9956	ws301g593	43.59	0.17	4.05	36.0	153.11	105.58	43.84	6.0	2432644.1	2456537.78	23	1515	4:7
	ws200g481	43.6	0.12	11.63	38.18	234.16	297.65	48.96	6.1	2406567.1	2456548.67	9	403	cb
	ws301g57	43.62	0.28	7.35	31.56	315.52	93.72	33.69	7.2	2464046.4	2456563.62	32	1457	4:7
	ws301g162	43.65	0.15	5.42	37.02	165.33	112.86	42.67	5.9	2435220.8	2456537.79	32	1510	4:7
	ws301g1198	43.65	0.18	2.38	35.91	249.86	80.72	37.01	7.3	2449042.3	2456546.8	12	1824	cb
K01QT8E	ws301g985	43.71	0.16	3.66	36.92	10.72	7.76	37.02	7.3	2458946.1	2456593.57	12	1125	4:7
	ws200g557	43.73	0.13	7.48	37.89	312.79	292.1	44.2	6.2	2431049.1	2456546.74	10	46	cb
	ws301g1437	43.75	0.02	2.89	42.67	314.09	127.0	43.51	6.7	2478736.2	2456578.63	15	1445	cb
U7616	ws301g951	43.77	0.08	10.36	40.42	87.23	17.77	43.73	4.8	2481563.7	2456618.58	18	755	cb
	ws301g1427	43.78	0.06	1.79	41.11	76.21	95.08	46.4	6.4	2505612.0	2456578.61	11	1445	cb
	ws301g1491	43.89	0.09	4.59	40.03	176.21	35.07	47.32	6.5	2412250.8	2456578.61	10	1063	cb
	ws301g582	43.94	0.01	1.63	43.33	282.25	136.32	43.55	6.2	2471258.6	2456546.8	28	1501	cb
K01QW2Q	ws301g231	43.99	0.05	3.96	41.71	350.58	76.48	43.03	6.2	2474956.6	2456544.71	27	1521	cb
	ws301g1446	44.01	0.08	2.97	40.38	322.46	30.28	40.48	7.0	2452819.9	2456604.67	9	1105	cb
K01QW2S	ws301g1061	44.02	0.04	0.25	42.32	359.21	348.45	42.39	6.7	2451959.5	2456565.66	16	1156	cb
	ws301g563	44.04	0.04	1.52	42.49	328.07	52.09	42.57	6.5	2461899.6	2456546.8	18	1508	cb
	ws200g80	44.11	0.48	5.1	23.01	275.94	302.25	48.54	5.1	2434167.4	2456540.63	9	1125	cen
	ws301ag324	44.14	0.01	1.6	43.64	312.96	63.16	43.66	6.7	2460556.7	2456578.61	9	1477	cb
	ws301ag187	44.15	0.06	1.47	41.32	273.83	70.02	41.44	6.3	2451903.8	2456618.57	15	1437	cb
	ws200g750	44.17	0.16	18.3	36.98	94.16	181.22	39.44	6.6	2444098.3	2456540.58	6	78	cb
	ws302g3	44.25	0.12	11.27	38.95	280.09	114.58	39.04	6.9	2459463.4	2456568.79	13	1504	cb
	ws301g639	44.36	0.1	11.25	40.13	82.59	130.2	48.1	5.2	2411832.5	2456576.73	23	1444	cb
K15RO5T	ws301g69	44.39	0.08	0.96	40.65	343.36	330.39	41.77	6.5	2443920.8	2456577.62	22	1478	cb
	ws301bg320	44.44	0.02	1.64	43.47	242.97	136.75	43.49	6.2	2460049.7	2456546.8	13	1095	cb

Continued on next page

MPC	DES	a (au)	e	i (°)	q (au)	ω (°)	Ω (°)	r (au)	H_r	T_{peri} (JD)	Epoch (JD)	N_{obs}	Arc (days)	Class
	ws301g300	44.63	0.02	1.16	43.59	319.26	49.15	43.59	6.5	2456579.4	2456563.61	13	1154	cb
	ws301g296	44.7	0.1	2.35	40.08	269.39	105.55	40.14	6.4	2459231.9	2456546.8	29	1508	cb
	ws200g456	44.75	0.17	13.22	37.24	163.02	209.94	38.14	6.8	2463777.3	2456564.65	7	13	sdo
	ws240g7	44.79	0.14	34.32	38.55	326.14	3.23	39.34	6.9	2464218.5	2456538.55	12	1100	cb
2014 TE86	2014 TE86	44.83	0.19	28.73	36.29	164.36	161.75	40.17	7.0	2442405.5	2458600.5	8	399	–
	ws200g732	44.84	0.13	4.85	39.15	304.87	353.5	41.47	6.5	2441968.4	2456537.76	12	1832	cb
	ws302g97	44.91	0.27	13.6	32.91	305.69	132.58	35.18	7.7	2465143.8	2456953.8	17	1141	sdo
2015 PF312	2015 PF312	45.03	0.09	18.0	41.15	260.78	160.68	41.42	6.1	2463211.5	2458200.5	140	3365	–
c5458	ws301g1190	45.11	0.18	5.15	36.82	288.36	347.35	43.4	6.6	2435740.8	2456577.62	6	40	sdo
K01QT7O	ws301ag286	45.12	0.18	1.13	36.9	305.24	143.14	42.99	6.1	2476488.0	2456543.69	9	74	cb
K01QT7P	ws301g153	45.21	0.12	1.43	39.76	164.12	111.81	44.64	6.4	2432785.6	2456578.61	12	1415	cb
2014 UF224	2014 UF224	45.24	0.13	27.16	39.5	332.34	174.32	46.79	7.5	2487371.5	2458600.5	99	859	–
K15PV2F	ws302g13	45.26	0.09	17.99	41.15	260.23	160.64	41.51	5.9	2463047.2	2456247.58	189	1887	cb
	ws301g1411	45.3	0.06	4.87	42.61	31.76	71.75	45.09	6.0	2481974.0	2456537.86	32	1476	cb
	ws301g946	45.31	0.17	16.9	37.53	336.0	21.23	37.74	7.1	2453129.1	2456564.73	11	410	cb
	ws200g198	45.34	0.16	15.18	38.2	78.0	184.37	44.36	6.5	2433887.4	2456546.77	17	1527	cb
	ws301g1346	45.35	0.08	1.19	41.7	249.74	109.14	41.74	7.0	2454200.0	2456563.61	14	1483	cb
	ws302g224	45.37	0.19	15.89	36.65	241.32	163.66	36.88	7.0	2459845.4	2456569.79	21	1175	cb
	ws301g1171	45.55	0.46	10.76	24.55	5.16	93.27	35.78	7.7	2468669.3	2456545.83	15	1468	cen
	ws301g935	45.56	0.18	19.11	37.5	330.54	50.24	37.58	6.3	2458575.7	2456545.84	34	1468	cb
	ws302g98	45.56	0.18	19.11	37.5	330.56	50.24	37.58	6.3	2458578.4	2456545.84	36	1824	cb
	ws301g127	45.6	0.14	6.46	39.03	269.76	67.99	39.31	6.8	2452048.2	2456546.73	23	1497	cb
(491768) 2012 VV113	(491768) 2012 VV113	45.84	0.11	15.68	40.75	294.87	115.97	40.93	7.4	2460386.5	2458200.5	73	1867	–
K14Qi2F	ws241g0	45.9	0.21	30.51	36.4	246.42	52.92	36.78	7.3	2452796.2	2456885.73	19	777	cb
(472262) 2014 QN441	(472262) 2014 QN441	45.98	0.28	20.69	33.12	242.64	144.55	33.14	6.6	2456152.5	2458600.5	83	2491	–
	ws14g1	46.07	0.16	29.91	38.75	339.55	131.19	42.18	6.6	2472843.7	2456916.86	19	1241	cb

Continued on next page

MPC	DES	a (au)	e	i (°)	q (au)	ω (°)	Ω (°)	r (au)	H_r	T_{peri} (JD)	Epoch (JD)	N_{obs}	Arc (days)	Class
	ws302g6	46.13	0.18	14.34	37.8	354.15	97.39	41.9	6.5	2472624.8	2456569.7	26	1511	cb
2014 QF442	2014 QF442	46.24	0.21	30.51	36.35	245.71	52.79	36.78	7.5	2452647.5	2458600.5	14	778	–
	ws200g615	46.31	0.34	14.39	30.4	86.48	202.61	31.86	7.8	2451275.5	2456543.63	14	1503	sdo
	ws200g492	46.43	0.27	17.32	33.83	359.04	293.76	35.95	7.3	2448485.5	2456545.56	8	32	cen
	ws302g89	46.46	0.2	12.59	36.98	246.94	71.98	40.07	6.6	2444045.7	2456569.67	18	1127	cb
K13TF9M	ws302g213	46.47	0.17	9.54	38.67	294.34	107.96	38.92	6.5	2460466.3	2456568.75	26	1504	cb
	ws301dg25	46.61	0.15	23.72	39.81	95.86	37.03	49.51	6.0	2491666.7	2456933.8	11	1066	cb
	ws301g945	46.62	0.2	3.46	37.55	2.92	106.15	44.64	5.9	2478433.7	2456958.73	9	20	sdo
	ws200g540	46.63	0.16	21.62	39.06	61.34	179.91	46.23	6.5	2431460.6	2456548.68	13	1117	cb
	ws301g998	46.66	0.1	4.63	42.23	302.63	111.08	43.28	6.0	2468493.3	2456569.66	26	1451	cb
(483002) 2014 QS441	(483002) 2014 QS441	46.84	0.08	37.91	43.11	268.35	185.94	44.84	5.4	2474291.5	2458600.5	94	6582	–
	ws240g10	46.88	0.19	26.48	38.02	274.95	30.89	38.02	6.7	2457353.7	2456912.56	16	1127	cb
	ws301g160	46.97	0.2	13.36	37.75	355.93	43.34	38.88	7.2	2465216.8	2457639.86	9	729	cb
m3002	ws302g163	47.01	0.08	37.88	43.09	267.62	185.93	44.89	5.3	2474035.9	2456594.65	209	1502	cb
2014 XY40	2014 XY40	47.09	0.15	29.06	39.98	38.55	132.75	53.65	5.1	2507586.5	2458200.5	27	1101	–
	ws301bg337	47.26	0.2	26.38	37.96	19.65	21.53	39.41	6.6	2465256.1	2456565.67	20	1487	cb
	ws301g798	47.49	0.2	6.68	37.89	20.37	96.33	48.6	6.2	2485224.3	2456974.63	10	1046	cb
D7295	ws302g42	47.55	0.29	12.69	33.65	208.66	175.72	33.65	6.8	2456774.2	2456545.87	31	1144	1:2
(495189) 2012 VR113	(495189) 2012 VR113	47.55	0.17	19.29	39.38	219.34	120.9	41.57	6.6	2444224.5	2458600.5	72	1499	–
	ws302g212	47.65	0.25	25.69	35.94	331.08	59.87	35.94	7.5	2456231.7	2456247.63	21	1126	1:2
E5452	ws200g379	47.65	0.67	33.26	15.68	289.71	172.68	44.46	4.0	2471925.5	2456575.59	10	1472	cen
	ws301ag101	47.66	0.23	23.32	36.59	221.65	186.41	38.74	6.9	2467132.0	2457642.73	7	20	det
	ws301g472	47.66	0.23	23.32	36.59	221.65	186.41	38.74	6.9	2467132.0	2457642.73	7	20	det
n5189	ws302g110	47.69	0.17	19.28	39.49	220.45	121.03	41.57	6.3	2444500.4	2456242.66	65	1884	1:2
	ws301bg306	47.88	0.32	4.8	32.58	339.45	14.47	32.77	7.8	2454495.1	2456568.59	10	1142	det
	ws200g519	48.01	0.07	4.24	44.82	90.34	225.8	45.25	6.2	2447060.9	2456546.76	11	1826	cb

Continued on next page

MPC	DES	a (au)	e	i (°)	q (au)	ω (°)	Ω (°)	r (au)	H_r	T_{peri} (JD)	Epoch (JD)	N_{obs}	Arc (days)	Class
	ws302g50	48.26	0.26	29.84	35.69	325.69	50.81	35.72	6.8	2455617.5	2456569.77	25	1488	det
2014 QL441	2014 QL441	48.47	0.26	26.33	36.11	292.36	75.71	36.51	6.5	2453218.5	2458600.5	57	459	–
2014 SZ348	2014 SZ348	48.5	0.25	47.67	36.24	224.26	158.44	36.97	8.0	2451827.5	2458600.5	136	880	–
2014 TU85	2014 TU85	48.65	0.31	16.36	33.64	306.13	120.76	35.18	8.4	2463526.5	2456940.5	9	17	–
	ws11g16	48.85	0.25	25.67	36.85	279.11	108.72	36.91	6.7	2458382.9	2456930.75	22	1179	det
	ws302g14	49.02	0.34	14.32	32.18	41.17	107.0	49.46	6.3	2481241.0	2456250.62	12	1805	sdo
	ws200g614	49.22	0.25	7.17	37.07	102.11	215.93	37.97	6.4	2450647.8	2456543.66	16	1826	det
K14Qi1L	ws12g6	49.32	0.28	26.27	35.59	283.1	75.85	36.49	6.1	2451530.4	2456887.77	34	55	det
2015 UK84	2015 UK84	49.46	0.24	23.58	37.64	187.71	156.27	39.26	6.8	2448691.5	2458600.5	21	740	–
	ws200g569	49.53	0.3	5.62	34.8	134.79	291.04	41.7	6.5	2471906.2	2456545.79	10	398	det
	ws200g425	49.58	0.31	8.08	34.4	296.08	336.16	43.63	6.6	2438584.7	2456564.69	8	53	cen
	ws302g164	49.64	0.26	20.04	36.88	30.74	75.27	43.14	6.1	2473439.1	2456888.89	10	1481	det
K15RO5T	ws301ag276	49.69	0.37	0.97	31.46	306.48	330.71	41.88	6.3	2440374.4	2456577.62	9	41	sdo
	ws119g0	49.96	0.19	37.56	40.63	245.36	105.57	40.92	7.2	2453147.8	2457327.73	7	29	cb
	ws200g686	50.02	0.34	18.89	32.78	246.32	183.65	42.18	6.5	2472847.3	2456576.6	7	1120	det
K13R98R	ws242g0	50.21	0.28	37.76	35.88	233.47	62.27	37.49	6.8	2449389.0	2456548.76	29	1497	det
	ws301g1357	50.36	0.28	19.59	36.43	203.65	167.37	36.44	7.1	2457064.2	2456569.66	14	1129	6:13
2013 RR98	2013 RR98	50.51	0.29	37.77	35.87	233.7	62.13	37.49	7.1	2449425.5	2458600.5	17	1193	–
	ws200g372	50.83	0.22	14.28	39.51	128.52	261.02	43.85	6.2	2471941.3	2456545.69	11	1502	5:11
	ws301bg310	50.84	0.26	2.68	37.69	16.83	32.96	39.8	7.0	2465698.3	2456563.61	7	55	det
	ws200g511	51.14	0.41	12.67	30.08	75.81	199.18	35.37	7.6	2446979.5	2456575.59	6	1091	cen
	ws301g1002	51.33	0.34	20.88	33.97	67.05	191.8	49.65	5.3	2432658.7	2456958.66	15	768	det
	ws200g2017	51.37	0.46	14.4	27.77	67.55	202.57	31.87	7.8	2449276.6	2456543.63	9	31	cen
	ws119g1	51.57	0.36	34.43	32.94	192.68	88.39	43.14	6.2	2440275.2	2457034.55	15	1049	4:9
	ws302g139	51.94	0.29	27.38	36.95	248.21	176.52	39.14	6.5	2465214.0	2456568.79	26	1525	det
	ws200g190	52.0	0.22	12.17	40.47	114.02	186.15	43.64	6.5	2443335.6	2456546.77	8	1476	cb

Continued on next page

MPC	DES	a (au)	e	i (°)	q (au)	ω (°)	Ω (°)	r (au)	H_r	T_{peri} (JD)	Epoch (JD)	N_{obs}	Arc (days)	Class
	ws200g364	52.2	0.29	12.88	37.26	118.92	334.7	50.69	6.1	2482524.9	2456565.61	14	39	sdo
	ws301g749	52.28	0.26	11.41	38.91	226.98	154.01	39.07	7.1	2459143.7	2456563.62	24	1447	det
	ws200g561	52.45	0.28	30.77	37.74	174.77	172.22	37.83	6.3	2458292.6	2456543.66	12	1829	det
	ws240g0	52.61	0.27	28.19	38.2	321.06	38.24	42.8	6.3	2471049.8	2457277.51	16	765	det
	ws240g6	52.86	0.38	29.92	32.59	9.74	41.44	50.49	5.7	2480519.4	2456565.5	12	1454	3:7
	ws302g31	53.05	0.37	9.99	33.2	276.33	109.98	33.2	7.3	2456300.3	2456544.87	18	1152	3:7
n5297	ws301g93	53.09	0.32	4.81	36.24	174.2	165.17	36.93	6.5	2452124.7	2456546.81	20	1180	3:7
(495297) 2013 TJ159	(495297) 2013 TJ159	53.13	0.32	4.81	36.2	173.73	165.17	36.94	6.5	2452037.5	2458600.5	29	5931	–
2014 QG442	2014 QG442	53.62	0.37	30.5	33.97	241.43	95.78	39.02	6.8	2445773.5	2458600.5	14	1219	–
K14Qi2G	ws13g4	53.76	0.37	30.46	34.07	241.85	95.9	39.02	6.4	2445853.7	2456888.92	15	500	det
	ws200g168	54.17	0.4	18.05	32.59	81.24	189.0	39.09	4.0	2444682.1	2456548.66	9	1499	det
K14N66B	ws200g81	54.4	0.12	4.68	47.6	56.06	296.56	47.61	5.4	2458618.5	2457657.63	7	8	cb
2013 VD24	2013 VD24	54.51	0.24	18.94	41.26	196.85	105.69	51.31	7.7	2431074.5	2456640.5	8	90	–
K13R98O	ws200g443	54.66	0.32	18.84	36.88	94.97	292.85	40.89	5.7	2467785.6	2456540.57	15	37	det
(495190) 2012 VS113	(495190) 2012 VS113	54.79	0.31	26.79	38.01	219.63	171.6	38.05	7.1	2455421.5	2458600.5	61	2923	–
2014 YL50	2014 YL50	55.02	0.32	29.15	37.57	236.53	127.26	38.38	7.0	2452082.5	2458600.5	10	363	–
n5190	ws302g182	55.07	0.31	26.79	38.04	220.14	171.6	38.05	6.8	2455533.9	2456243.66	131	1867	det
	ws200g806	55.09	0.66	7.38	18.81	297.07	290.82	46.02	5.1	2440413.5	2456576.59	10	1120	cen
2015 PD312	2015 PD312	55.15	0.37	23.06	34.64	225.98	154.8	34.77	7.9	2455327.5	2458600.5	41	856	–
K14N66B	ws200g18	55.32	0.21	4.68	43.82	111.16	296.53	47.71	5.4	2474152.9	2457614.78	8	51	cb
	ws302g210	55.36	0.45	13.03	30.33	333.32	65.6	30.59	7.8	2458454.8	2456545.85	13	470	2:5
	ws302g124	55.37	0.45	15.07	30.56	187.61	170.1	33.36	7.3	2450085.5	2456619.71	12	395	det
K14Y50L	ws12g3	55.45	0.32	29.15	37.42	234.35	127.38	38.37	6.7	2451690.8	2457007.68	21	1127	2:5
	ws12g4	55.46	0.36	32.12	35.59	338.51	89.06	37.84	7.2	2464531.2	2456961.78	9	1409	2:5
K14UM5N	ws251g2	55.51	0.25	53.19	41.4	317.06	68.83	46.92	5.1	2474120.1	2456952.51	9	22	det
2013 RQ98	2013 RQ98	56.47	0.44	37.69	31.54	245.69	11.18	33.32	7.5	2451207.5	2458600.5	11	1134	–

Continued on next page

MPC	DES	a (au)	e	i (°)	q (au)	ω (°)	Ω (°)	r (au)	H_r	T_{peri} (JD)	Epoch (JD)	N_{obs}	Arc (days)	Class
K15RO5W	ws301g958	56.52	0.53	13.3	26.47	19.74	0.39	26.78	8.6	2458222.1	2456578.59	9	395	cen
k9750	ws200g598	57.01	0.48	7.59	29.78	83.67	188.99	41.08	5.6	2442574.3	2456543.67	6	34	sdo
	ws119g2	57.13	0.47	44.67	30.06	258.72	103.79	30.09	8.4	2456217.5	2456891.85	18	1162	sdo
	ws118g6	57.77	0.35	29.96	37.51	344.34	76.06	41.44	6.5	2468103.4	2457251.91	17	1117	det
2014 RS63	2014 RS63	58.09	0.35	28.99	37.52	307.03	38.85	38.37	6.8	2461722.5	2456920.5	7	55	–
	ws200g515	58.25	0.41	23.79	34.47	305.44	358.41	39.43	6.2	2446006.4	2456546.77	15	71	det
K14UM5N	ws252g0	59.21	0.35	53.15	38.69	323.41	68.69	46.93	5.2	2474199.6	2456952.51	17	1070	det
2016 QP85	2016 QP85	59.37	0.33	15.62	39.81	278.14	121.27	39.84	7.3	2458174.5	2458200.5	58	509	–
	ws200g175	59.4	0.29	11.95	41.93	206.34	186.32	44.22	6.1	2466469.6	2456565.62	7	1102	det
	ws200g466	59.6	0.4	8.39	36.0	36.87	255.56	40.03	7.1	2446606.5	2456548.68	10	403	det
2014 UN225	2014 UN225	59.92	0.36	53.11	38.53	323.41	68.52	46.93	5.4	2474062.5	2458600.5	13	709	–
	ws241g7	60.21	0.39	28.98	36.79	314.58	38.93	38.36	6.7	2463089.1	2456904.69	7	54	det
	ws302g160	60.99	0.4	14.19	36.78	334.77	76.79	38.68	7.4	2463347.9	2456568.79	12	1506	det
	ws200g272	61.2	0.42	25.26	35.71	112.27	176.16	38.11	7.0	2449292.1	2456546.7	12	1110	det
	ws301g720	61.53	0.38	5.47	38.34	181.2	156.35	39.59	7.1	2450746.3	2456568.59	18	1455	det
	ws11g4	61.55	0.42	28.59	35.52	215.04	153.69	35.7	7.4	2454976.0	2456888.85	22	1220	det
K14Od4Q	ws301g375	61.96	0.44	29.49	34.72	157.84	186.62	35.44	6.7	2452862.4	2456544.7	32	1503	det
D4210	ws200g516	62.01	0.39	6.48	37.62	22.17	316.33	37.82	7.0	2454341.5	2456540.62	15	1525	det
	ws11g5	62.41	0.32	31.23	42.74	267.8	145.45	44.85	5.9	2466298.7	2456982.7	24	1112	det
K10T00J	ws17g1	62.86	0.36	38.9	39.92	273.91	91.3	40.75	5.3	2451887.0	2456887.91	24	1239	det
2013 RO98	2013 RO98	63.04	0.47	18.74	33.72	105.38	292.53	40.84	6.0	2468415.5	2458600.5	13	35	–
	ws13g7	65.14	0.44	28.56	36.49	229.99	129.55	39.66	6.6	2448565.1	2456927.82	21	1169	det
	ws200g451	65.67	0.62	8.17	24.95	51.74	199.72	43.14	6.4	2442099.2	2456565.62	8	1092	cen
m0017	ws302g128	66.34	0.45	7.29	36.63	269.32	75.29	38.94	6.0	2449547.3	2456568.64	24	1121	det
	ws14g4	67.22	0.36	32.48	43.1	287.45	149.53	44.59	6.3	2464239.9	2456904.9	16	1247	det
	ws301bg348	67.73	0.44	4.45	38.01	247.36	114.15	38.03	7.2	2455913.0	2456564.73	21	1459	det

Continued on next page

MPC	DES	a (au)	e	i (°)	q (au)	ω (°)	Ω (°)	r (au)	H_r	T_{peri} (JD)	Epoch (JD)	N_{obs}	Arc (days)	Class
2014 UA225	2014 UA225	67.73	0.46	3.57	36.67	17.88	344.55	36.8	6.8	2456007.5	2458600.5	41	1214	–
D6199	ws302g183	67.83	0.44	43.99	38.09	151.22	35.98	96.45	-1.4	2545665.6	2456547.89	30	1528	det
2014 QR441	2014 QR441	68.17	0.37	42.23	42.61	282.78	77.78	42.98	6.8	2460324.5	2458600.5	47	485	–
K14UM5A	ws301g955	69.07	0.48	3.6	35.68	357.89	344.78	36.78	6.6	2452457.3	2456951.71	9	24	sdo
	ws302g86	69.1	0.5	18.99	34.49	45.03	46.67	44.42	5.8	2470771.4	2456568.64	18	1803	det
	ws12g5	69.12	0.51	28.28	33.91	294.54	130.86	36.09	6.9	2462922.0	2457003.7	11	1367	2:7
	ws301g934	69.28	0.47	16.69	36.85	331.66	42.21	36.85	7.0	2456596.9	2456569.66	24	1801	2:7
	ws302g148	69.5	0.55	26.78	31.05	218.8	175.11	31.39	6.8	2458580.4	2456568.63	24	1525	2:7
	ws301g988	69.55	0.54	11.24	32.17	41.7	8.69	34.98	7.5	2463140.3	2456887.82	8	88	sdo
	ws301g546	69.7	0.48	12.61	36.43	352.32	14.87	36.48	7.4	2457492.4	2456578.63	15	1792	det
	ws302g132	72.21	0.68	17.89	23.21	345.61	63.09	23.86	9.0	2458453.2	2456568.75	14	447	cen
2016 SW50	2016 SW50	72.84	0.51	32.55	35.85	333.78	61.04	36.01	8.7	2459260.5	2458600.5	26	423	–
	ws302g111	73.16	0.48	28.5	38.32	158.01	182.8	43.16	6.2	2445981.2	2456568.79	25	1533	det
2014 SO350	2014 SO350	75.11	0.54	24.05	34.59	243.96	140.99	34.64	7.9	2456314.5	2458200.5	19	1152	–
E5480	ws200g50	75.66	0.39	26.48	46.2	171.44	180.45	46.24	4.0	2457714.6	2456540.62	30	1541	det
K14SZ0O	ws12g12	75.8	0.54	24.04	34.6	244.15	141.0	34.62	7.4	2456349.5	2456930.76	24	1439	1:4
(451657) 2012 WD36	(451657) 2012 WD36	75.83	0.51	23.69	37.44	293.93	177.33	49.31	6.8	2473200.5	2458600.5	63	3012	–
	ws13g11	75.85	0.51	30.74	36.89	226.46	109.01	44.33	5.8	2444389.5	2456915.83	18	1454	1:4
	ws11g23	79.57	0.55	23.39	36.22	276.98	69.2	37.25	6.7	2452752.2	2456888.83	15	810	det
2013 SE99	2013 SE99	79.92	0.54	18.3	36.53	223.74	100.39	46.49	7.8	2442242.5	2458600.5	18	448	–
	ws11g14	80.72	0.71	37.13	23.68	215.1	167.68	23.68	8.0	2457157.7	2457318.74	7	1051	cen
	ws301g1060	82.47	0.58	19.75	34.52	10.67	27.92	37.17	7.0	2462817.2	2456578.73	7	1120	sdo
	ws200g683	83.04	0.53	14.12	39.37	145.11	189.42	39.73	6.5	2453879.9	2456576.6	8	1475	det
	ws12g0	85.75	0.6	22.9	33.92	277.13	108.86	33.92	7.6	2456724.4	2456931.88	13	1163	det
2015 PK312	2015 PK312	89.3	0.65	23.42	31.31	226.2	159.95	31.38	9.8	2456366.5	2457280.5	12	62	–
	ws301g1071	89.48	0.62	12.85	34.28	162.36	176.76	36.27	6.8	2451361.7	2456544.72	26	1476	sdo

Continued on next page

MPC	DES	a (au)	e	i (°)	q (au)	ω (°)	Ω (°)	r (au)	H_r	T_{peri} (JD)	Epoch (JD)	N_{obs}	Arc (days)	Class
	ws200g122	90.02	0.63	17.15	33.16	86.9	192.48	37.46	6.3	2449070.4	2456538.68	16	1509	sdo
	ws302g165	90.6	0.68	9.47	29.39	237.37	141.27	29.45	7.6	2456206.3	2456951.77	7	770	cen
	ws240g5	91.71	0.62	29.55	35.17	357.65	14.31	47.66	5.8	2471419.6	2456565.5	16	1474	det
E5474	ws302g17	92.24	0.64	16.27	33.06	277.08	170.35	38.94	6.1	2465055.8	2456268.65	32	1828	sdo
	ws118g8	92.8	0.69	28.99	28.5	336.87	132.53	54.04	4.7	2476244.6	2456982.7	9	1101	cen
	ws200g248	95.6	0.74	13.59	24.89	79.43	185.21	42.66	6.1	2443815.1	2456544.67	8	1493	cen
h7360	ws302g192	98.96	0.74	41.11	26.19	285.9	191.44	39.62	5.8	2467890.8	2456930.78	54	102	cen
K14SZ0R	ws241g5	100.96	0.63	28.77	36.99	220.11	35.12	45.86	6.1	2444454.4	2456886.71	17	782	det
2014 SR350	2014 SR350	102.4	0.64	28.78	37.08	220.67	35.02	45.91	6.5	2444540.5	2458600.5	15	743	–
	ws302g44	103.38	0.72	18.02	28.53	292.41	177.07	40.08	5.2	2467377.5	2456594.67	6	1062	cen
	ws17g0	104.64	0.52	43.15	50.2	296.98	130.38	52.53	5.3	2465809.3	2456925.82	26	1444	det
2014 UZ224	2014 UZ224	108.18	0.65	26.79	38.02	30.0	130.8	92.54	3.5	2503562.5	2458600.5	18	814	–
K14UM4Z	ws13g2	108.56	0.65	26.78	38.33	29.42	131.0	92.54	3.0	2503592.7	2456888.92	21	1221	det
(437360) 2013 TV158	(437360) 2013 TV158	109.86	0.67	31.15	36.47	231.93	181.08	37.08	6.3	2459753.5	2458600.5	346	5223	–
h7360	ws302g60	111.23	0.67	31.14	36.47	232.11	181.08	37.23	6.1	2459779.8	2456575.64	317	1551	det
	ws200g624	111.73	0.76	10.27	26.23	142.64	285.7	44.91	6.0	2470029.4	2456564.67	11	1062	cen
	ws302g209	116.76	0.69	18.58	36.69	270.91	120.02	36.93	7.2	2454806.5	2456619.75	7	34	det
	ws200g461	120.83	0.67	31.67	40.0	160.02	175.66	40.52	6.7	2453656.4	2456543.67	17	1829	det
2014 UY224	2014 UY224	125.03	0.84	26.46	20.37	308.44	145.33	25.0	8.9	2461199.5	2458600.5	14	422	–
	ws240g11	133.5	0.75	28.5	33.73	208.87	75.94	34.84	7.2	2453480.0	2456898.55	11	1147	sdo
	ws200g520	158.49	0.77	17.4	36.66	27.4	293.44	37.17	6.3	2454070.2	2456540.57	14	1832	etno
	ws200g30	161.46	0.72	4.82	45.92	123.36	219.36	46.08	6.3	2455855.5	2457657.63	8	39	etno
o8338	ws302g147	164.77	0.8	23.41	33.17	354.78	33.63	33.4	6.3	2457992.2	2456545.85	16	443	etno
2016 QV89	2016 QV89	167.95	0.76	21.39	39.95	281.19	173.22	50.95	5.9	2469961.5	2458600.5	123	1882	–
2016 QU89	2016 QU89	168.58	0.79	16.99	35.25	303.29	102.8	35.92	7.9	2459240.5	2458600.5	39	1559	–
	ws302g10	171.62	0.77	21.39	39.96	281.09	173.22	50.95	5.7	2469915.1	2456247.59	121	1882	etno

Continued on next page

MPC	DES	a (au)	e	i (°)	q (au)	ω (°)	Ω (°)	r (au)	H_r	T_{peri} (JD)	Epoch (JD)	N_{obs}	Arc (days)	Class
k9750	ws200g444	174.69	0.83	6.17	29.25	227.86	192.49	40.15	6.0	2466379.0	2456537.74	34	1544	cen
	ws11g19	205.1	0.87	26.12	25.98	298.53	148.5	34.82	7.2	2464481.8	2456888.86	25	1481	cen
	ws302g63	232.92	0.85	13.22	35.11	296.29	118.98	36.81	7.1	2460726.5	2456568.8	32	1525	etno
	ws301g157	314.39	0.88	6.5	38.13	265.48	94.73	38.26	6.8	2455322.0	2456544.71	31	1479	etno
2013 RF98	2013 RF98	357.63	0.9	29.59	36.07	311.61	67.58	36.3	8.7	2455100.5	2458600.5	51	1092	–
K15Bp9P	ws121g0	449.42	0.92	54.11	35.25	348.06	135.21	55.08	4.2	2473015.0	2456988.83	27	1175	etno
	ws302g153	462.24	0.9	12.4	46.01	262.92	104.8	46.34	5.9	2454268.8	2456547.89	19	1822	etno

BIBLIOGRAPHY

BIBLIOGRAPHY

Abbott, T., Abdalla, F. B., Allam, S., et al. 2016a, Phys. Rev. D, 94, 022001

Abbott, T., Abdalla, F. B., Aleksić, J., et al. 2016b, MNRAS, 460, 1270

Abbott, T. M. C., Catarutti, R., Mondaca, E., et al. 2006, in Proc. SPIE, Vol. 6267, Society of Photo-Optical Instrumentation Engineers (SPIE) Conference Series, 62673M

Bannister, M. T., Kavelaars, J. J., Petit, J.-M., et al. 2016, AJ, 152, 70

Bannister, M. T., Gladman, B. J., Kavelaars, J. J., et al. 2018, The Astrophysical Journal Supplement Series, 236, 18

Batygin, K., Adams, F. C., Brown, M. E., & Becker, J. C. 2019, Physics Reports, doi:https://doi.org/10.1016/j.physrep.2019.01.009

Batygin, K., & Brown, M. E. 2016, AJ, 151, 22

Becker, J. C., Khain, T., Hamilton, S. J., et al. 2018, AJ, 156, 81

Bernardinelli, P. H., Bernstein, G. M., Sako, M., et al. 2019, in prep

Bernstein, G., & Khushalani, B. 2000, AJ, 120, 3323

Bernstein, G. M., Trilling, D. E., Allen, R. L., et al. 2004, AJ, 128, 1364

Bernstein, J. P., Kessler, R., Kuhlmann, S., et al. 2012, ApJ, 753, 152

Brasser, R., & Morbidelli, A. 2013, Icarus, 225, 40

Brasser, R., & Schwamb, M. E. 2015, MNRAS, 446, 3788

Brown, M. E. 2001, AJ, 121, 2804

—. 2017, AJ, 154, 65

Brown, M. E., & Batygin, K. 2019, AJ, 157, 62

Brown, M. E., & Butler, B. J. 2017, AJ, 154, 19

Brucker, M. J., Grundy, W. M., Stansberry, J. A., et al. 2009, Icarus, 201, 284

Buratti, B. J., Hofgartner, J. D., Hicks, M. D., et al. 2017, Icarus, 287, 207

Chambers, J. E. 1999, MNRAS, 304, 793

Chen, Y.-Y., Ma, Y., & Zheng, J. 2016, MNRAS, 458, 4277

Chiang, E. I., & Lithwick, Y. 2005, ApJ, 628, 520

Dalle Ore, C. M., Dalle Ore, L. V., Roush, T. L., et al. 2013, Icarus, 222, 307

Dark Energy Survey Collaboration, Abbott, T., Abdalla, F. B., et al. 2016, MNRAS, 460, 1270

Davies, J. K., McFarland, J., Bailey, M. E., Marsden, B. G., & Ip, W. H. 2008, The Early Development of Ideas Concerning the Transneptunian Region, ed. M. A. Barucci, H. Boehnhardt, D. P. Cruikshank, A. Morbidelli, & R. Dotson, 11

de la Fuente Marcos, C., de la Fuente Marcos, R., & Aarseth, S. J. 2017, Ap&SS, 362, 198

Diehl, H. T., Neilsen, E., Gruendl, R., et al. 2016, in Proc. SPIE, Vol. 9910, Society of Photo-Optical Instrumentation Engineers (SPIE) Conference Series, 99101D

Edgeworth, K. E. 1943, Journal of the British Astronomical Association, 53, 181

Elliot, J. L., Kern, S. D., Clancy, K. B., et al. 2005, AJ, 129, 1117

Flaugher, B. 2005, International Journal of Modern Physics A, 20, 3121

Flaugher, B., Diehl, H. T., Honscheid, K., et al. 2015, AJ, 150, 150

Fornasier, S., Lellouch, E., Müller, T., et al. 2013, A&A, 555, A15

Fraser, W. C., & Brown, M. E. 2012, ApJ, 749, 33

Fraser, W. C., Brown, M. E., Morbidelli, A., Parker, A., & Batygin, K. 2014, ApJ, 782, 100

Gerdes, D. W., Jennings, R. J., Bernstein, G. M., et al. 2016, AJ, 151, 39

Gerdes, D. W., Sako, M., Hamilton, S., et al. 2017, ApJ, 839, L15

Gladman, B., Bannister, M. T., Kavelaars, J., et al. 2018, in AAS/Division for Planetary Sciences Meeting Abstracts, 302.01

Gladman, B., Kavelaars, J. J., Nicholson, P. D., Loredo, T. J., & Burns, J. A. 1998, AJ, 116, 2042

Gladman, B., Marsden, B. G., & Vanlaerhoven, C. 2008, in The Solar System Beyond Neptune, ed. M. A. Barucci, H. Boehnhardt, D. P. Cruikshank, A. Morbidelli, & R. Dotson, 43–57

Gladman, B., Lawler, S. M., Petit, J.-M., et al. 2012, AJ, 144, 23

Goldstein, D. A., D'Andrea, C. B., Fischer, J. A., et al. 2015, AJ, 150, 82

Gomes, R., Levison, H. F., Tsiganis, K., & Morbidelli, A. 2005, Nature, 435, 466

H. Neilsen, J., Bernstein, G., Gruendl, R., & Kent, S. 2016, doi:10.2172/1250877

Hahn, J. M., & Malhotra, R. 2005, AJ, 130, 2392

Hamilton, S. J., Napier, K. J., Gerdes, D. W., et al. 2019, in prep

Heinze, A. N., Metchev, S., & Trollo, J. 2015, AJ, 150, 125

Jewitt, D., & Luu, J. 1992, Astron. J., 104, 398

Jewitt, D., & Luu, J. 1993, Nature, 362, 730

Jewitt, D. C., & Luu, J. X. 1995, AJ, 109, 1867

Johnston, W. R. 2018, NASA Planetary Data System, 307

Jones, R. L., Gladman, B., Petit, J.-M., et al. 2006, Icarus, 185, 508

Kaib, N. A., & Sheppard, S. S. 2016, AJ, 152, 133

Kaiser, N., Kaiser, N., Aussel, H., et al. 2002, Soc. Photo-Optical Instrum. Eng. Conf. Ser., 4836, 154

Kavelaars, J., Jones, L., Gladman, B., Parker, J. W., & Petit, J.-M. 2008, The Orbital and Spatial Distribution of the Kuiper Belt, ed. M. A. Barucci, H. Boehnhardt, D. P. Cruikshank, A. Morbidelli, & R. Dotson, 59–69

Kavelaars, J. J., Jones, R. L., Gladman, B. J., et al. 2009, AJ, 137, 4917

Kessler, R., Marriner, J., Childress, M., et al. 2015, AJ, 150, 172

Khain, T., Gerdes, D. W., Becker, J. C., et al. 2019, in prep

Khain, T., Becker, J. C., Adams, F. C., et al. 2018, AJ, 156, 273

Kortenkamp, S. J., Malhotra, R., & Michtchenko, T. 2004, Icarus, 167, 347

Kuiper, G. P. 1951, Proceedings of the National Academy of Science, 37, 717

Lacerda, P., Fornasier, S., Lellouch, E., et al. 2014, ApJ, 793, L2

Lawler, S. M., Kavelaars, J. J., Alexandersen, M., et al. 2018a, Frontiers in Astronomy and Space Sciences, 5, 14

Lawler, S. M., Shankman, C., Kaib, N., et al. 2017, AJ, 153, 33

Lawler, S. M., Pike, R. E., Kaib, N., et al. 2018b, ArXiv e-prints, arXiv:1808.02618

Lebofsky, L. A., & Spencer, J. R. 1989, in Asteroids II, ed. R. P. Binzel, T. Gehrels, & M. S. Matthews, 128–147

Lebofsky, L. A., Sykes, M. V., Tedesco, E. F., et al. 1986, Icarus, 68, 239

Levison, H. F., Morbidelli, A., Tsiganis, K., Nesvorný, D., & Gomes, R. 2011, AJ, 142, 152

Levison, H. F., Morbidelli, A., Van Laerhoven, C., Gomes, R., & Tsiganis, K. 2008, Icarus, 196, 258

Li, J.-Y., McFadden, L. A., Parker, J. W., et al. 2006, Icarus, 182, 143

Lin, H. W., Gerdes, D. W., Hamilton, S. J., et al. 2019, Icarus, 321, 426

Lykawka, P. S., & Mukai, T. 2005, Planetary and Space Science, 53, 1319

Madigan, A.-M., & McCourt, M. 2016, MNRAS, 457, L89

Millis, R. L., Buie, M. W., Wasserman, L. H., et al. 2002, AJ, 123, 2083

Mommert, M., Harris, A. W., Kiss, C., et al. 2012, A&A, 541, A93

Morbidelli, A., Levison, H. F., Tsiganis, K., & Gomes, R. 2005, Nature, 435, 462

Morbidelli, A., Tsiganis, K., Crida, A., Levison, H. F., & Gomes, R. 2007, Astron. J., 134, 1790

Morganson, E., Gruendl, R. A., Menanteau, F., et al. 2018, Publications of the Astronomical Society of the Pacific, 130, 074501

Moullet, A., Lellouch, E., Moreno, R., & Gurwell, M. 2011, Icarus, 213, 382

Napier, K. J., Gerdes, D. W., Hamilton, S. J., et al. 2019, in prep

Nesvorný, D. 2015, AJ, 150, 73

Nesvorný, D., & Morbidelli, A. 2012, AJ, 144, 117

Nesvorný, D., & Vokrouhlický, D. 2009, AJ, 137, 5003

—. 2016, ApJ, 825, 94

Nesvorný, D., Vokrouhlický, D., & Roig, F. 2016, ApJ, 827, L35

Noll, K. S., Grundy, W. M., Stephens, D. C., Levison, H. F., & Kern, S. D. 2008, Icarus, 194, 758

Pál, A., Kiss, C., Müller, T. G., et al. 2012, A&A, 541, L6

Parker, A. H. 2015, Icarus, 247, 112

Petit, J.-M., Kavelaars, J. J., Gladman, B. J., et al. 2011, AJ, 142, 131

Santos-Sanz, P., Lellouch, E., Fornasier, S., et al. 2012, A&A, 541, A92

Schwamb, M. E., Brown, M. E., & Rabinowitz, D. L. 2009, ApJ, 694, L45

Schwamb, M. E., Brown, M. E., Rabinowitz, D. L., & Ragozzine, D. 2010, Astrophys. J., 720, 1691

Schwamb, M. E., Fraser, W. C., Bannister, M. T., et al. 2018, arXiv e-prints, arXiv:1809.08501

Shankman, C., Kavelaars, J. J., Bannister, M. T., et al. 2017, AJ, 154, 50

Sheppard, S. S., & Trujillo, C. 2016, AJ, 152, 221

Sheppard, S. S., & Trujillo, C. A. 2006, Science, 313, 511

Sheppard, S. S., Trujillo, C. A., Oldroyd, W. J., Tholen, D. J., & Williams, G. V. 2018, Minor Planet Electronic Circulars, 2018-Y14

Sheppard, S. S., Trujillo, C. A., Tholen, D. J., & Kaib, N. 2019, AJ, 157, 139

Sicardy, B., Ortiz, J. L., Assafin, M., et al. 2011, Nature, 478, 493

Smith, J. A., Tucker, D. L., Kent, S., et al. 2002, The Astronomical Journal, 123, 2121

Stansberry, J., Grundy, W., Brown, M., et al. 2008, in The Solar System Beyond Neptune (University of Arizona Press), 161–179

Tancredi, G., & Favre, S. 2008, Icarus, 195, 851

Tegler, S. C., & Romanishin, W. 2000, Nature, 407, 979

Trujillo, C. A., & Sheppard, S. S. 2014, Nature, 507, 471

Tsiganis, K., Gomes, R., Morbidelli, A., & Levison, H. F. 2005, Nature, 435, 459

Volk, K., & Malhotra, R. 2017, AJ, 154, 62

Volk, K., Murray-Clay, R., Gladman, B., et al. 2016, AJ, 152, 23

Wong, I., Brown, M. E., & Emery, J. P. 2014, AJ, 148, 112